Volume 71C
Number 1
Jan.–Mar. 1967

Engineering and Instrumentation

U.S. DEPARTMENT OF COMMERCE

SECTION C

JOURNAL OF RESEARCH

NATIONAL BUREAU OF STANDARDS

Journal of Research
of the
National Bureau of Standards

C. Engineering and Instrumentation

Jan.–Mar. • 1967

VOLUME • 71C

NUMBER • 1

Editor: Martin Greenspan

Associate Editors: G. F. Montgomery, R. V. Smith, A. F. Schmidt

Publication dates:
Feb. 15, May 15, Aug. 15, Nov. 15, 1967

JOURNAL OF RESEARCH

The National Bureau of Standards Journal of Research reports research and development in the fields of activity shown at right. Also included from time to time are survey articles on topics closely related to the Bureau's scientific and technical program.

The Journal is published in three separate sections as follows:

A. Physics and Chemistry

Contains papers of interest primarily to scientists working in these fields. Issued six times a year. Annual subscription: domestic, $5.00; foreign, $6.00. Single copy, $1.00.

B. Mathematics and Mathematical Physics

Presents studies and compilations designed mainly for the mathematician and the theoretical physicist. Issued quarterly. Annual subscription: domestic, $2.25; foreign, $2.75. Single copy, 75¢.

C. Engineering and Instrumentation

Reports research and development results of interest chiefly to the engineer and the applied scientist. Issued quarterly. Annual subscription: domestic, $2.75; foreign, $3.00. Single copy, 75¢.

The National Bureau of Standards is a principal focal point in the Federal Government for assuring maximum application of the physical and engineering sciences to the advancement of technology in industry and commerce. Its responsibilities include development and maintenance of the national standards of measurement, and the provisions of means for making measurements consistent with those standards; determination of physical constants and properties of materials; development of methods for testing materials, mechanisms, and structures, and making such tests as may be necessary, particularly for government agencies; cooperation in the establishment of standard practices for incorporation in codes and specifications; advisory service to government agencies on scientific and technical problems; invention and development of devices to serve special needs of the Government; assistance to industry, business, and consumers in the development and acceptance of commercial standards and simplified trade practice recommendations; administration of programs in cooperation with United States business groups and standards organizations for the development of international standards of practice; and maintenance of a clearinghouse for the collection and dissemination of scientific, technical, and engineering information. The scope of the Bureau's activities is suggested in the following listing of its three Institutes and their organizational units.

Institute for Basic Standards. Applied Mathematics. Electricity. Metrology. Mechanics. Heat. Atomic Physics. Physical Chemistry. Laboratory Astrophysics.* Radiation Physics. Radio Standards Laboratory:* Radio Standards Physics; Radio Standards Engineering. Office of Standard Reference Data.

Institute for Materials Research. Analytical Chemistry. Polymers. Metallurgy. Inorganic Materials. Reactor Radiations. Cryogenics.* Materials Evaluation Laboratory. Office of Standard Reference Materials.

Institute for Applied Technology. Building Research. Information Technology. Performance Test Development. Electronic Instrumentation. Textile and Apparel Technology Center. Technical Analysis. Office of Weights and Measures. Office of Engineering Standards. Office of Invention and Innovation. Office of Technical Resources. Clearinghouse for Federal Scientific and Technical Information.**

*Located at Boulder, Colo. 80302.
**Located at 5285 Port Royal Road, Springfield, Va. 22151.

U.S. DEPARTMENT OF COMMERCE
Alexander B. Trowbridge, Acting Secretary
NATIONAL BUREAU OF STANDARDS
A. V. Astin, Director

Order all publications from the Superintendent of Documents
U.S. Government Printing Office, Washington, D.C. 20402.

Use of funds for printing this publication approved by the Director of the Bureau of the Budget (June 22, 1966).

Dedication of the New NBS Laboratories

On November 15, 1966, Secretary of Commerce John T. Connor dedicated the new ultra-modern facilities of the National Bureau of Standards at Gaithersburg, Md. This $120 million laboratory complex serves as the nerve center of the Nation's measurement and standardization activities. With three Institutes devoted to Basic Standards, Materials Research, and Applied Technology, the Bureau's new home has been designed to meet the needs of today and the challenges of the future in the physical sciences.

Dedication ceremonies were held in a courtyard between the Bureau's new library and one of the laboratory buildings. In the center of the courtyard is an apple tree descended from the tree under which Sir Isaac Newton was sitting when, according to the story, an apple fell on his head, leading him to conceive the law of universal gravitation.

Surrounding this tree was an audience of 2500, including distinguished guests from government, industry, and the world scientific community. The Reverend Edward G. Latch, Chaplain of the House of Representatives, gave the invocation and the benediction. Introduced by Dr. A. V. Astin, Director of the National Bureau of Standards, Secretary Connor said:

"It is no accident of history that the establishment of NBS in 1901 coincided with the beginning of America's transformation into the industrial giant of the twentieth century. . . . Today the demands made upon the Bureau and the nature of its program reflect the complexity of our atomic and space-age world."

The Secretary began his remarks with a message from President Johnson. The President noted that throughout its 65 years' existence the Bureau had advanced the frontiers of measurement in pace with the demands of science and industry; he extended his congratulations and best wishes for continuing achievement.

Secretary Connor stated that at age 65 the Bureau had significant accomplishments behind it and a future promising even greater contributions to the Nation. He noted that the new facilities are a symbol of the Bureau's future, but that the germ of future achievement lies in the members of the Bureau's staff.

In connection with the dedication, the Secretary

Eleven stories high, the Administration Building at the National Bureau of Standards' new site near Gaithersburg, Md., towers above the other buildings in the laboratory complex. The building houses the Director and his staff as well as other NBS activities not requiring laboratory space.

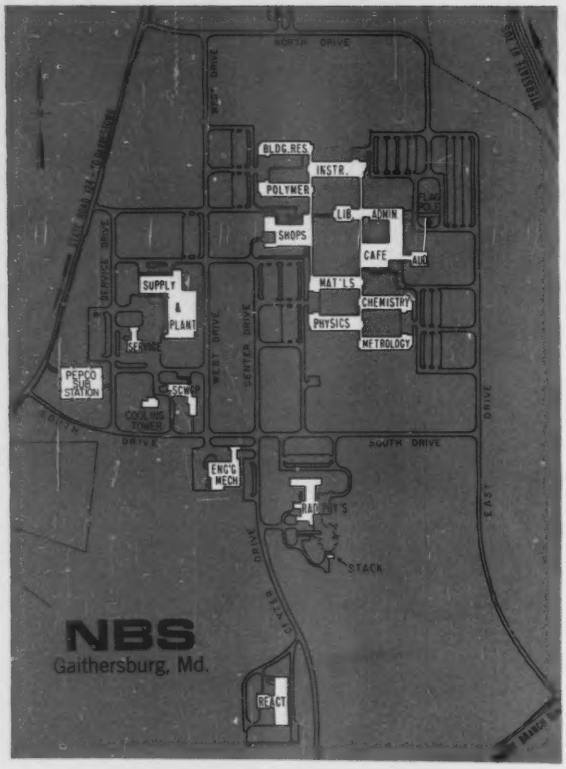

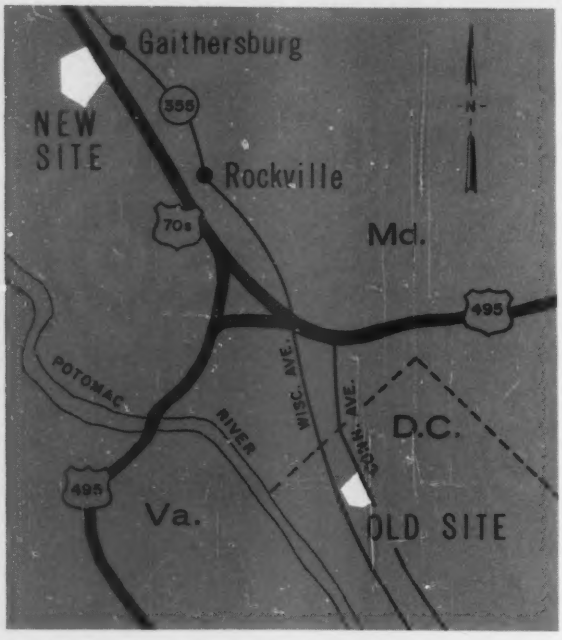

The new NBS site is 20 miles northwest of the old Washington site, at the Darnestown exit of Interstate Highway 70S. It borders and is west of 70S and Gaithersburg, Md. The plan view shows the layout of existing buildings.

sponsored a Symposium on Technology and World Trade which was held at the Bureau during the two days following the dedication. It featured as speakers experts from industry, government, and education of many countries, attracting an attendance of nearly 500.

Following the dedication ceremonies, the invited guests were given a tour of the installation. On Saturday, November 19, the general public was invited to visit the new facilities and to view over 100 laboratories and demonstrations. In an eight-hour period over 20,000 people roamed the site. Some of the things they saw were a 100-ft linear accelerator which produces one of the world's most intense electron beams; a recently completed high-flux research reactor; a 12-million pound capacity hydraulic testing machine; the NBS Museum containing historical instruments, equipment, standards, and materials pertaining to the Bureau's activities during its 65-year history; a vault containing the national measurement standards—or parts symbolizing those standards; a demonstration of glass blowing techniques used to make highly unusual, and precise apparatus; and many of the Bureau's laboratories in the fields of metrology, electricity, mechanics, heat, atomic physics, radiation physics, analytical chemistry, physical chemistry, polymers, metallurgy, and building research.

By the close of 1966, transfer of the Bureau's Washington (D.C.) laboratories to the Gaithersburg site will be largely completed and most of the 2700 staff members will be relocated in 15 major buildings at the site. Of about 300 persons remaining at the Washington site, most will be relocated in new special-purpose laboratories now under construction at Gaithersburg. In addition, the Bureau will continue to maintain a staff of about 600 in Boulder, Colo., for work in radio standards and cryogenics, and a staff of about 300 at the Clearinghouse for Federal Scientific and Technical Information at Springfield, Va., as well as small groups of employees at widely scattered field stations.

Although the Bureau is located 20 miles northwest of its old site, the mailing address remains: National Bureau of Standards, Washington, D.C. 20234. The new telephone number is (Area Code 301) 921–1000. To reach the Bureau by car, use the Darnestown exit on Interstate Highway 70S.

JOURNAL OF RESEARCH of the National Bureau of Standards—C. Engineering and Instrumentation
Vol. 71C, No. 1, January–March 1967

Symmetrical Bending of Thin Circular Elastic Plates on Equally Spaced Point Supports

A. F. Kirstein and R. M. Woolley

Institute for Basic Standards, National Bureau of Standards, Washington, D.C. 20234

(August 23, 1966)

A special application of Bassali's solution for transverse flexure of thin elastic plates supported at several points is presented for the case of symmetrical bending. Equations for moments, shearing forces, and stresses are developed which may be useful for design purposes. The experimental results although limited in quantity are in good agreement with the theoretical predictions.

Key Words: Circular plates, concentric loading, design, elasticity, experiment, maximum stresses, symmetrical bending, symmetrically distributed load, theory.

1. Introduction

The determination of bending moments, twisting moments, and shearing forces in a thin circular elastic plate subjected to symmetrical bending is a problem which is often encountered in the design and analysis of structural elements or systems. This study deals with the solution of this problem for a thin circular elastic plate supported at points equally spaced along a concentric support circle and subjected to a transverse load which is symmetrically distributed over a concentric circular area. These structures may be typified as end closures, bulkheads, and diaphragms. Usually the analysis of such a structure is simplified by the introduction of engineering approximations which pertain to the particular structural system under examination. However, this paper presents a special application of a more general solution developed by Bassali [1][1] which more closely represents the conditions realized in practical structures and obviates the necessity for some of the approximations.

This specialized treatment of Bassali's theory provides the equations necessary to calculate moments, shearing forces, and associated stresses anywhere within the plate. It also shows that the expressions for maximum bending stresses at the center are independent of the angular orientation and the number of supports. Further reduction of these expressions result in the Grashof [2] equations.

A comparison between a limited amount of experimental results and the theoretical predictions of tangential strains along the concentric support circle show good agreement. This good agreement for strains along with that for deflections [3] tend to substantiate the theory.

2. List of Symbols

r, θ polar coordinates
c radius of the plate
a radius of the concentric support circle
b radius of the loaded area (region 1) of the plate
h thickness of the plate

[1] Figures in brackets indicate the literature references at the end of this paper.

$\rho = r/c$ $\quad b' = b\sqrt{n/n'}$

$t = a/c$ $\quad n' = n+2$

$q = b/c$ $\quad q' = b'/c$

m number of support points ($m \geq 3$)

$\alpha = 2\pi/m$, polar angle subtended by support points

$\theta_s = s\alpha$, polar angle subtended by the sth support point ($s = 1, 2, 3, \ldots m$)

$\varphi_s = \theta - \theta_s$

E modulus of elasticity

ν Poisson's ratio

$\kappa = (3+\nu)/(\nu-1)$

p_0 intensity of load

p_1 transverse load intensity over $0 \leq r \leq b$ (region 1)

p_2 transverse load intensity over $b \leq r \leq c$ (region 2)

P_0 total load on the plate defined by eq (1.02)

M moment

Q shearing force

σ stress

ϵ strain.

Subscripts:

1, 2 refer to regions 1 and 2, respectively

r, t refer to radial and tangential, respectively

rt refers to twisting.

3. Background

Bassali obtained the solution for the problem of flexure of a thin circular elastic plate supported at several arbitrarily located interior points and transversely loaded over a circular area eccentrically located with respect to the center of the plate. Bassali considers the intensity of the transverse load over the circular area indicated as region 1 in figure 1 to be

$$p_1 = p_0 r^{n-2}, \quad (n \geq 2) \tag{1.01}$$

and the intensity over region 2 to be $p_2 = 0$. This, of course, shows that the load is distributed symmetrically with respect to the center of region 1, and the value of n defines the load distribution ($n = 2$ represents uniform load distribution). The total load on the plate is given by

$$P_0 = 2\pi p_0 \frac{b^n}{n}. \tag{1.02}$$

The boundary of the plate is considered to be free as the plate is supported at interior points, but no special treatment is required when some or all of the supports lie on the boundary.

In a previous paper [3] a special application of this more general solution was used to obtain a method of determining the deflection of a plate subjected to symmetrical bending with the load uniformly distributed over region 1. A comparison of theoretical and experimental results indicated that the theory adequately predicted the deflection of the plates over the range of geometries tested. Further observations indicated that the theory accounted for a constraining effect on the deflection which for the most part was due to the annular portion of the plate overhanging the support circle. It was also noted that this constraining effect decreased as the number of supports were increased, but did not vanish when the number of supports became sufficiently large to produce a support condition equivalent to that of a simple continuous line support.

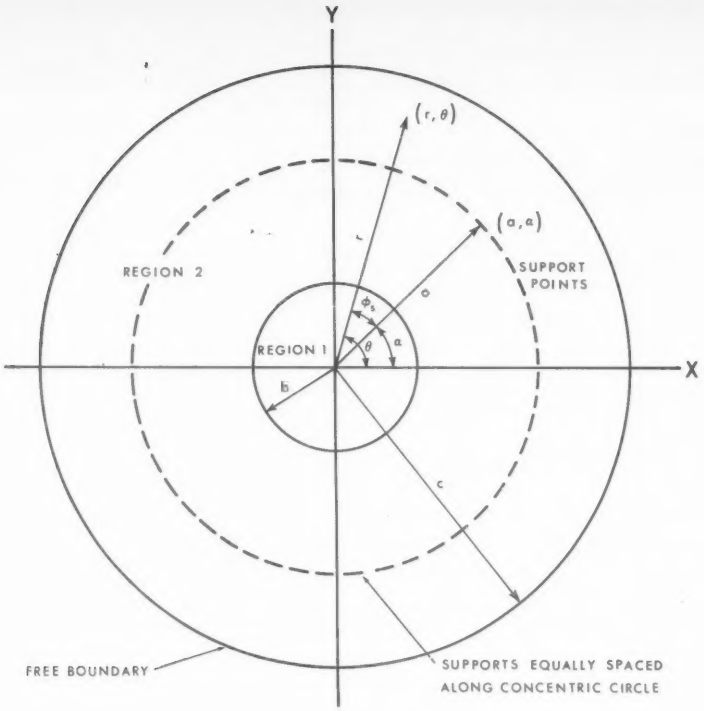

FIGURE 1. *Concentric arrangement of the circular plate.*

With regard to the preceding discussion it was deemed desirable to extend the previous work [3] to encompass moments, shearing forces, and stresses, for the purpose of presenting equations which may be adapted to the design and analysis of structures of this type.

4. Moments and Shearing Forces for Symmetrical Bending

It can be shown that Bassali's solution, reduced to the case of symmetrical bending, yields the following expressions for the radial and tangential bending moments in region 1

$$M'_{r_1}=-\frac{P_0(1+\nu)}{8\pi m\kappa}\left[\Psi'_1\right]+\frac{P_0(1-\nu)}{16\pi m\kappa\rho^2}\left[\Omega'_1\right] \tag{1.03}$$

and

$$M'_{t_1}=-\frac{P_0(1+\nu)}{8\pi m\kappa}\left[\Psi'_1\right]-\frac{P_0(1-\nu)}{16\pi m\kappa\rho^2}\left[\Omega'_1\right], \tag{1.04}$$

respectively, where

$$\Psi'_1=\left[\sum_{s=1}^{m}\left\{\ln(1-2\rho t\cos\varphi_s+\rho^2t^2)-\kappa\ln(\rho^2-2\rho t\cos\varphi_s+t^2)-\frac{(1-t^2)(1-\rho^2t^2)}{(1-2\rho t\cos\varphi_s+\rho^2t^2)}\right\}\right.$$

$$\left.+\frac{2mt^2}{(1+\nu)}+m-\frac{2m\kappa q'^2}{\kappa+1}+2m\kappa\ln q+\frac{2m\kappa}{n}\left(\frac{\rho^n}{q^n}-1\right)\right] \tag{1.05}$$

and

$$\Omega_1'=\left[\sum_{s=1}^{m}\left\{(\kappa^2-1)\ln(1-2\rho t\cos\varphi_s+\rho^2t^2)+\frac{(1-\rho^2t^2)^2-2t^2(1-\rho^2)^2}{(1-2\rho t\cos\varphi_s+\rho^2t^2)}\right.\right.$$

$$\left.\left.-\frac{(1-\rho^2)(1-t^2)(1-\rho^2t^2)^2}{(1-2\rho t\cos\varphi_s+\rho^2t^2)^2}+\frac{\kappa(\rho^2-t^2)^2}{(\rho^2-2\rho t\cos\varphi_s+t^2)}\right\}+m(\kappa-1)(\rho^2-t^2)-\frac{4m\kappa\rho^{n'}}{n'q^n}\right]. \quad (1.06)$$

For region 2,

$$M_{r_2}'=-\frac{P_0(1+\nu)}{8\pi m\kappa}\left[\Psi_2'\right]+\frac{P_0(1-\nu)}{16\pi m\kappa\rho^2}\left[\Omega_2'\right] \quad (1.07)$$

and

$$M_{t_2}'=-\frac{P_0(1+\nu)}{8\pi m\kappa}\left[\Psi_2'\right]-\frac{P_0(1-\nu)}{16\pi m\kappa\rho^2}\left[\Omega_2'\right], \quad (1.08)$$

respectively, where

$$\Psi_2'=\left[\sum_{s=1}^{m}\left\{\ln(1-2\rho t\cos\varphi_s+\rho^2t^2)-\kappa\ln(\rho^2-2\rho t\cos\varphi_s+t^2)-\frac{(1-t^2)(1-\rho^2t^2)}{(1-2\rho t\cos\varphi_s+\rho^2t^2)}\right\}\right.$$

$$\left.+\frac{2mt^2}{(1+\nu)}+m-\frac{2m\kappa q'^2}{\kappa+1}+2m\kappa\ln\rho\right] \quad (1.09)$$

and

$$\Omega_2'=\left[\sum_{s=1}^{m}\left\{(\kappa^2-1)\ln(1-2\rho t\cos\varphi_s+\rho^2t^2)+\frac{(1-\rho^2t^2)^2-2t^2(1-\rho^2)^2}{(1-2\rho t\cos\varphi_s+\rho^2t^2)}-\frac{(1-\rho^2)(1-t^2)(1-\rho^2t^2)^2}{(1-2\rho t\cos\varphi_s+\rho^2t^2)^2}\right.\right.$$

$$\left.\left.+\frac{\kappa(\rho^2-t^2)^2}{(\rho^2-2\rho t\cos\varphi_s+t^2)}\right\}+m(\kappa-1)(\rho^2-t^2)-2m\kappa\rho^2+2m\kappa q'^2\right]. \quad (1.10)$$

It is noted here that the equation for the twisting moment is the same for regions 1 and 2 and may be expressed as

$$M_{rt}=\frac{P_0(1-\nu)}{8\pi m\kappa\rho^2}\left[\sum_{s=1}^{m}\left\{\frac{\rho t\sin\varphi_s(\rho^2-t^2)}{(1-2\rho t\cos\varphi_s+\rho^2t^2)}-\frac{\rho t\sin\varphi_s(1-\rho^2)(1-t^2)(1-\rho^2t^2)}{(1-2\rho t\cos\varphi_s+\rho^2t^2)^2}\right.\right.$$

$$\left.\left.-\frac{\kappa\rho t\sin\varphi_s(\rho^2-t^2)}{(\rho^2-2\rho t\cos\varphi_s+t^2)}-(\kappa^2-1)\arctan\frac{\rho t\sin\varphi_s}{1-\rho t\cos\varphi_s}\right\}\right] \quad (1.11)^2$$

and that the equation for the tangential shearing force is also the same for regions 1 and 2. The tangential shearing force is given by

$$Q_t=\frac{P_0}{4\pi rm\kappa}\left[\sum_{s=1}^{m}\left\{\frac{2\kappa\rho t\sin\varphi_s}{(\rho^2-2\rho t\cos\varphi_s+t^2)}-\frac{2\rho t\sin\varphi_s}{(1-2\rho t\cos\varphi_s+\rho^2t^2)}-\frac{2\rho t\sin\varphi_s(1-t^2)(1-\rho^2t^2)}{(1-2\rho t\cos\varphi_s+\rho^2t^2)^2}\right\}\right]. \quad (1.12)$$

---

[2] Bassali's eq (2.44) for M_{rt_1} was incorrect in that a factor, his P_s, was omitted from the summation. No doubt this was a typographical error as his equation for M_{rt_2} was correct, and for the general solution of eccentric loading M_{rt_1} must equal M_{rt_2} at the boundary between regions 1 and 2.

The radial shearing forces in regions 1 and 2 as reduced from the general solution are

$$Q'_{r_1}=\frac{P_0}{4\pi rm\kappa}\left[\sum_{s=1}^{m}\left\{\frac{\kappa(\rho^2-t^2)}{(\rho^2-2\rho t\cos\varphi_s+\rho^2t^2)^2}+\frac{(1-2\rho^2+\rho^2t^2)t^2}{(1-2\rho t\cos\varphi_s+\rho^2t^2)}\right.\right.$$
$$\left.\left.+\frac{(1-t^2)(1-\rho^2t^2)^2}{(1-2\rho t\cos\varphi_s+\rho^2t^2)^2}\right\}+m(\kappa-1)-\frac{2m\kappa\rho^2}{q^n}\right] \tag{1.13}$$

and

$$Q'_{r_2}=\frac{P_0}{4\pi rm\kappa}\left[\sum_{s=1}^{m}\left\{\frac{\kappa(\rho^2-t^2)}{(\rho^2-2\rho t\cos\varphi_s+t^2)}+\frac{(1-2\rho^2+\rho^2t^2)t^2}{(1-2\rho t\cos\varphi_s+\rho^2t^2)}+\frac{(1-t^2)(1-\rho^2t^2)^2}{(1-2\rho t\cos\varphi_s+\rho^2t^2)^2}\right\}-m(\kappa+1)\right], \tag{1.14}$$

respectively.

5. The Uniformly Distributed Concentric Load

The case of the uniformly distributed concentric load with its limiting cases of the concentrated central load and the load uniformly distributed over the entire plate is of more general interest than the case of the symmetrically distributed load given in the preceding section. Therefore this investigation will deal primarily with the case of the uniformly distributed load. It should be noted that no special treatment is required to examine the limiting cases mentioned above, as they are implicit in the solution. The concentrated central load is represented by permitting q to shrink to zero, and the load uniformly distributed over the entire plate is realized by setting $q=1$. It remains then only to select the appropriate equations for the region under analysis.

The equations for moments and shearing forces given in the preceding section were derived for the symmetrically distributed concentric load as defined by eq (1.01). In order to obtain similar equations for the uniformly distributed concentric load it is a simple matter of supplying the appropriate values for n, n', and q', viz, $n=2$, $n'=4$, and $q'=q/\sqrt{2}$. Thus, eqs (1.03) and (1.04) become

$$M_{r_1}=-\frac{P_0(1+\nu)}{8\pi m\kappa}[\Psi_1]+\frac{P_0(1-\nu)}{16\pi m\kappa\rho^2}[\Omega_1] \tag{1.15}$$

and

$$M_{t_1}=-\frac{P_0(1+\nu)}{8\pi m\kappa}[\Psi_1]-\frac{P_0(1-\nu)}{16\pi m\kappa\rho^2}[\Omega_1], \tag{1.16}$$

respectively, where eqs (1.05) and (1.06) become

$$\Psi_1=\left[\sum_{s=1}^{m}\left\{\ln(1-2\rho t\cos\varphi_s+\rho^2t^2)-\kappa\ln(\rho^2-2\rho t\cos\varphi_s+t^2)-\frac{(1-t^2)(1-\rho^2t^2)}{(1-2\rho t\cos\varphi_s+\rho^2t^2)}\right\}\right.$$
$$\left.-\frac{2mt^2\left(1+\dfrac{\kappa q^2}{2-t^2}\right)}{\kappa+1}+m(1+t^2)+2m\kappa\ln q+\frac{m\kappa\rho^2}{q^2}-m\kappa\right] \tag{1.17}$$

and

$$\Omega_1=\left[\sum_{s=1}^{m}\left\{(\kappa^2-1)\ln(1-2\rho t\cos\varphi_s+\rho^2t^2)+\frac{(1-\rho^2t^2)^2-2t^2(1-\rho^2)^2}{(1-2\rho t\cos\varphi_s+\rho^2t^2)}-\frac{(1-\rho^2)(1-t^2)(1-\rho^2t^2)^2}{(1-2\rho t\cos\varphi_s+\rho^2t^2)^2}\right.\right.$$
$$\left.\left.+\frac{\kappa(\rho^2-t^2)^2}{(\rho^2-2\rho t\cos\varphi_s+t^2)}\right\}+m(\kappa-1)(\rho^2-t^2)-\frac{m\kappa\rho^4}{q^2}\right], \tag{1.18}$$

respectively. Following this same procedure, the radial and tangential bending moments in region 2, obtained from eqs (1.07) and (1.08) are

$$M_{r_2}=-\frac{P_0(1+\nu)}{8\pi m\kappa}[\Psi_2]+\frac{P_0(1-\nu)}{16\pi m\kappa\rho^2}[\Omega_2] \tag{1.19}$$

and

$$M_{t_2}=-\frac{P_0(1+\nu)}{8\pi m\kappa}[\Psi_2]-\frac{P_0(1-\nu)}{16\pi m\kappa\rho^2}[\Omega_2], \tag{1.20}$$

respectively, where eqs (1.09) and (1.10) become

$$\Psi_2=\Bigg[\sum_{s=1}^{m}\left\{\ln(1-2\rho t\cos\varphi_s+\rho^2t^2)-\kappa\ln(\rho^2-2\rho t\cos\varphi_s+t^2)-\frac{(1-t^2)(1-\rho^2t^2)}{(1-2\rho t\cos\varphi_s+\rho^2t^2)}\right\}$$

$$-\frac{2mt^2\left(1+\frac{\kappa q^2}{2t^2}\right)}{\kappa+1}+m(1+t^2)+2m\kappa\ln\rho\Bigg] \tag{1.21}$$

and

$$\Omega_2=\Bigg[\sum_{s=1}^{m}\left\{(\kappa^2-1)\ln(1-2\rho t\cos\varphi_s+\rho^2t^2)+\frac{(1-\rho^2t^2)^2-2t^2(1-\rho^2)^2}{(1-2\rho t\cos\varphi_s+\rho^2t^2)}-\frac{(1-\rho^2)(1-t^2)(1-\rho^2t^2)^2}{(1-2\rho t\cos\varphi_s+\rho^2t^2)^2}\right.$$

$$\left.+\frac{\kappa(\rho^2-t^2)^2}{(\rho^2-2\rho t\cos\varphi_s+t^2)}\right\}+m(\kappa-1)(\rho^2-t^2)-2m\kappa\rho^2+m\kappa q^2\Bigg], \tag{1.22}$$

respectively.

Since the expressions for the twisting moment, M_{rt}, the tangential shearing force, Q_t, and the radial shearing force in region 2, Q'_{r_2} are independent of the load distribution, eqs (1.11), (1.12), and (1.14) are also appropriate for the case of the uniformly distributed load. However, Q'_{r_1} of eq (1.13) being dependent on n, becomes

$$Q'_{r_1}=\frac{P_0}{4\pi rm\kappa}\Bigg[\sum_{s=1}^{m}\left\{\frac{\kappa(\rho^2-t^2)}{(\rho^2-2\rho t\cos\varphi_s+t^2)}+\frac{(1-2\rho^2+\rho^2t^2)t^2}{(1-2\rho t\cos\varphi_s+\rho^2t^2)}\right.$$

$$\left.+\frac{(1-t^2)(1-\rho^2t^2)^2}{(1-2\rho t\cos\varphi_s+\rho^2t^2)^2}\right\}+m(\kappa-1)-\frac{2m\kappa\rho^2}{q^2}\Bigg] \tag{1.23}$$

for uniform loading.

6. Stress at the Center of the Plate

An examination of eq (1.11) shows that $M_{rt}=0$ as a limit when $\rho\to 0$, and is independent of the angular orientation. Therefore Mohr's circle becomes a point, $M_{t_1}=M_{r_1}$, and $\sigma_{r_1}=\sigma_{t_1}$. It is noted that M_{r_1} and M_{t_1} given in eqs (1.15) and (1.16), respectively, differ only in the sign of the second term of each equation, and that these terms, having ρ^2 in the denominator cannot be solved directly when $\rho=0$. However, they can be evaluated by setting $M_{r_1}=M_{t_1}$. Thus, eqs (1.15) and (1.16) yield

$$\Bigg[\sum_{s=1}^{m}\left\{(\kappa^2-1)\ln(1-2\rho t\cos\varphi_s+\rho^2t^2)+\frac{(1-\rho^2t^2)^2-2t^2(1-\rho^2)}{(1-2\rho t\cos\varphi_s+\rho^2t^2)}-\frac{(1-\rho^2)(1-t^2)(1-\rho^2t^2)^2}{(1-2\rho t\cos\varphi_s+\rho^2t^2)^2}\right.$$

$$\left.+\frac{\kappa(\rho^2-t^2)^2}{(\rho^2-2\rho t\cos\varphi_s+t^2)}\right\}+m(\kappa-1)(\rho^2-t^2)-\frac{m\kappa\rho^4}{q^2}\Bigg]=0$$

from which it is obvious that the second terms of eqs (1.15) and (1.16) are equal to zero when $\rho = 0$. The moments at the center of the plate ($\rho = 0$) may now be written as

$$M_{r_1} = M_{t_1} = -\frac{P_0(1+\nu)}{8\pi m\kappa}\left[-2m\kappa \ln t + \frac{2m\kappa t^2\left(1-\frac{q^2}{2t^2}\right)}{\kappa+1} + 2m\kappa \ln q - m\kappa\right]_{\rho=0} \tag{1.24}$$

and the stresses on the surface are given by

$$\sigma_{r_1} = \sigma_{t_1} = \pm\frac{3P_0(1+\nu)}{4\pi h^2}\left[\frac{2t^2\left(1-\frac{q^2}{2t^2}\right)}{\kappa+1} + 2\ln\frac{q}{t} - 1\right]_{\rho=0}. \tag{1.25}$$

As a matter of convenience for graphical representation eq (1.25) may be written as

$$\sigma_{r_1} = \sigma_{t_1} = -\frac{3P_0}{4\pi h^2}[\xi - \lambda] \tag{1.26}$$

where

$$\xi = (1+\nu)\ln q^2 + \frac{(1-\nu)}{2}q^2 \tag{1.27}$$

and

$$\lambda = (1+\nu)(1+\ln t^2) + (1-\nu)t^2. \tag{1.28}$$

Figure 2 is the graphical representation of eqs (1.27) and (1.28) for $\nu = 0.3$. It is apparent from the λ curve that the stresses at the center of the plate are also affected by the portion of the plate that overhangs the supports. The ξ curve shows how q affects the stresses at the center. It should be noted that when $q \to 0$, σ_r and $\sigma_t \to \infty$. It is obvious that this theory cannot be used to compute stress at or very near a concentrated load or reaction point.

An examination of eq (1.25) shows that the stresses at the center of the plate are independent of m and θ, and it can be shown that this equation reduces to

$$\sigma = \frac{3P_0}{8\pi h^2}(3+\nu) \tag{1.29}$$

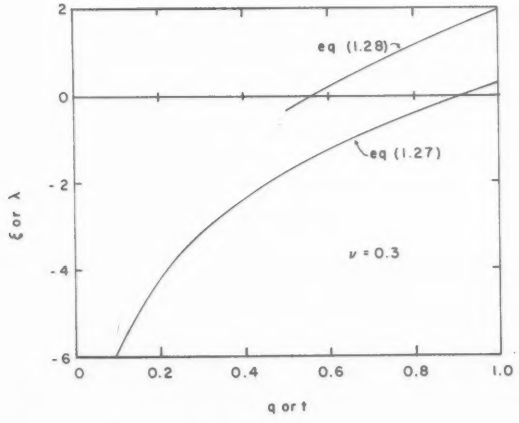

FIGURE 2. *Factors which affect the stress at the center of the plate.*

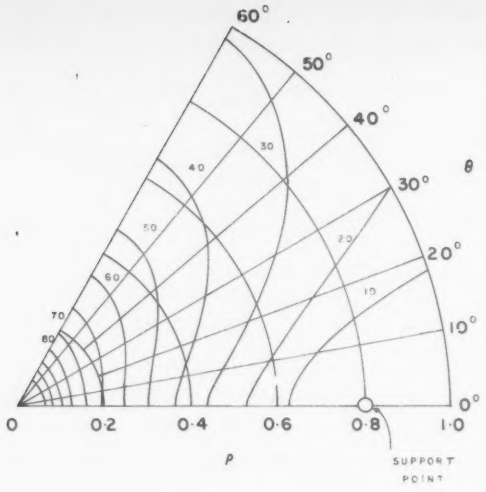

FIGURE 3. *Distribution of maximum principal stresses in the plate.*

for the case of a simply supported, uniformly loaded plate ($t=q=1$). Furthermore, for the case of a simply supported circular plate having a central load ($q=b/c$ and $t=1$) eq (1.25) reduces to

$$\sigma=\frac{3P_0(1+\nu)}{2\pi h^2}\left[\frac{1}{(1+\nu)}+\ln\frac{c}{b}-\frac{b^2\,(1-\nu)}{4c^2\,(1+\nu)}\right]. \tag{1.30}$$

Thus, it is shown that for these limiting cases eq (1.25) reduces to the Grashof equations.

It should be noted that the usable strength of a plate is usually greater than that implied by eqs (1.25), (1.26), (1.29), and (1.30) [4]. These are elastic equations, and experience shows that local yielding of materials at a highly stressed point does not necessarily indicate structural failure or excessive deflection. Therefore, predictions of structural failure based on these equations would require the use of an appropriate theory of failure.

Moments and Stresses Elsewhere in the Plate. To illustrate the stress distribution over a segment of a plate, figure 3 presents lines of equal maximum principal stress sensitivity (σ/P_0) over one half the period of symmetrical distribution. This figure was prepared from the results obtained from eqs (1.11), (1.19), and (1.20) for the following conditions: $m=3$, $t=0.8$, $q=0$, $\nu=0.3$, and $h=0.125$. It can be noted from the figure that the support is located on the ray $\theta=0°$, and that the larger values of the maximum principal stress sensitivity extend the farthest out from the center along the ray $\theta=\pi/m$. These rays have further distinction in that an examination of the twisting moment, eq (1.11), shows that $M_{rt}=0$ for any values of ρ and t along these angular orientations. It follows then that the bending moments, M_r and M_t, along these rays produce principal stresses.

7. Comparison of Theoretical and Experimental Results

The test results presented herein were obtained from retesting specimen A of a previous investigation [3]. Since the specimens, materials, and test methods were fully described in the previous paper, it suffices here to indicate that the dead load method of testing was used, and the tangential strains were measured along the support circle ($t=0.976$ and $m=3$) by means of foil type electrical resistance strain gages having a gage length of 1/8 in. These gages were mounted on the top and bottom surface of the specimen at the angular locations indicated in figure 4.

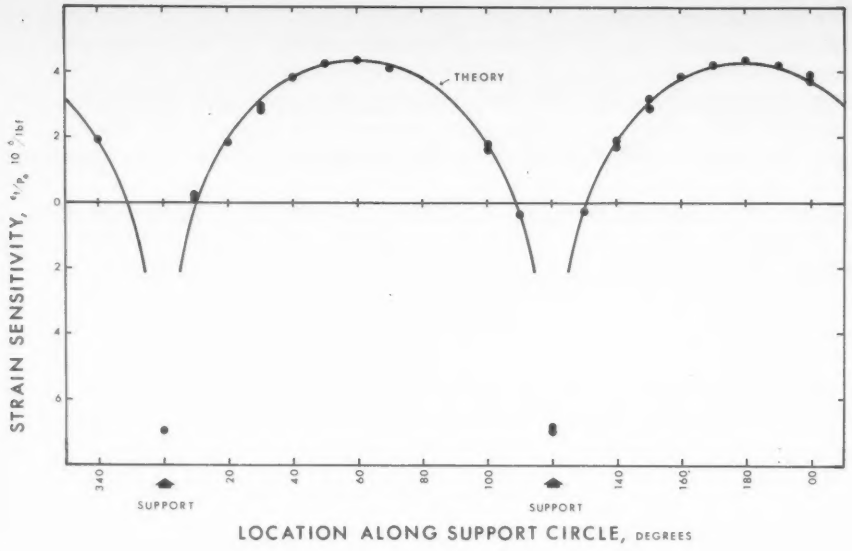

FIGURE 4. *Theoretical and experimental strain sensitivities along the support circle.*

The tangential strains were computed for the expression

$$\epsilon_{t_2}=\frac{1}{E}(\sigma_{t_2}-\nu\sigma_{r_2})=\pm\frac{6}{Eh^2}(M_{t_2}-\nu M_{r_2}). \tag{1.31}$$

Inserting the appropriate values for radial and tangential bending moment from eqs (1.19) and (1.20) yields

$$\epsilon_{t_2}=\pm\frac{3P_0(1-\nu^2)}{4\pi mEh^2\kappa}\left(\Psi_2+\frac{\Omega_2}{2\rho^2}\right) \tag{1.32}$$

where Ψ_2 and Ω_2 are given by eqs (1.21) and (1.22), respectively.

The agreement between the experimental data, which represents two separate sets of test results, and the theoretical results shown in figure 4 is very good. This, along with the good agreement reported for deflection [3], lends credence to the use of the theory to predict the flexural behavior of the plates.

8. Summary

The special application of Bassali's more general solution presented herein provides the equations necessary to calculate the elastic moments, shearing forces, and stresses anywhere in a thin circular elastic plate supported at points equally spaced along a concentric support circle and subjected to symmetrical bending. However, the maximum stresses at the center of the plate are probably of more general interest in the design and analysis of the thin circular plate subjected to a uniformly distributed concentric load. It is interesting to note that the equations take on a very simple form for these stresses and appear to be well adapted for design purposes. It is of

further interest that these stresses, eq (1.25), are independent of angular orientation and the number of supports. As in the case of deflection [3], the effect of the annular portion of the plate overhanging the support circle is evident as illustrated by the λ curve in figure 2.

Caution should be exercised in the use of these elastic equations for design purposes as local yielding may not be a valid design criterion for the particular material and structure under consideration. The selection of an appropriate theory of failure is of the utmost importance in this case.

The good agreement between the theoretical and experimental strains presented herein along with that for deflection [3] serve to substantiate the ability of the theory to predict the flexual behavior of the plates.

The authors are indebted to W. H. Pell of the National Science Foundation for his advice during the initial phases of this investigation, and to D. R. Tate for his valuable suggestions. Special mention is due L. J. Davis for his active participation in the Laboratory.

9. References

[1] Bassali, W. A., The Transverse Flexure of Thin Elastic Plates Supported at Several Points, Proceedings Cambridge Philosophical Society, Vol. **53**, 728–743, 1957.

[2] Morley, A., Strength of Materials (Longmans, Green and Company, 8th ed., 1935).

[3] Kirstein, A. F., W. H. Pell, R. M. Woolley, and L. J. Davis, Deflection of centrally loaded thin circular elastic plates on equally spaced point supports, J. Res. NBS **70C** (Engr. and Instr.) No. 4, 227 (1966).

[4] Seely, F. B., Advanced Mechanics of Materials (John Wiley & Sons, Inc., New York, N.Y., First Edition, 1950).

(Paper 71C1–438)

JOURNAL OF RESEARCH of the National Bureau of Standards—C. Engineering and Instrumentation
Vol. 71C, No. 1, January–March 1967

Ultrasonic Measurement of Cylinder Expansion at Pressures to 40 Kilobars

Peter L. M. Heydemann and James C. Houck

Institute for Basic Standards, National Bureau of Standards, Washington, D.C. 20234

(September 12, 1966)

For the accurate determination of internal pressures in solid-filled piston and cylinder devices the effective area and its change with pressure are very significant factors. The computation of the change of area with pressure from elastic theory leads however to considerable uncertainties.

The present paper describes how ultrasonic measurements made in solid-filled piston and cylinder devices to 45 kilobars are combined with measurements of the lengths of the samples as function of pressure and with ultrasonic measurements under hydrostatic pressure to yield values for cylinder expansion. The results are compared with values obtained from modified elastic theory.

Key Words: Compressibility, cylinder distortion, high pressure, nickel, tellurium, ultrasonics.

1. Introduction

Several solid filled piston and cylinder devices with rotatable pistons have been used in this laboratory to determine transition pressures at pressures up to 45 kbar. The internal pressure was computed as the ratio of ram force on the piston to effective area of the cylinder. Appropriate corrections were made for friction between moving and stationary parts and for distortion of the cylinder. An estimate of the change of the effective area of the cylinder with internal pressure was calculated using equations developed from elastic theory for long thick-walled cylinders subjected to internal pressure. These relations were modified using the solution to the tangential strain problem for an infinite cylinder with a semi-infinite zone of internal pressure [1].[1]

The estimated uncertainty in this calculation of the area is two parts per thousand at 25 kbar and four parts per thousand at 40 kbar provided that the elastic theory on which the calculation is based accurately describes the problem. This uncertainty is sufficiently large to warrant some effort in a direct determination of the change of area of the cylinder with internal pressure. This paper describes such a direct determination by means of ultrasonic measurements on a sample contained in the cylinder.

The ultrasonic measurements are used to determine the compressibility of the sample as a function of pressure. From this the length, which the sample would have in a rigid cylinder at any given pressure, is computed. This hypothetical length will be compared with a sample length obtained from a direct measurement at the same pressure. The ratio of these two lengths is a measure of the expansion of the cylinder.

2. Definition of Expansion Factor

We assume a mean value for the expansion of the cylinder over the pressurized length (fig. 1) and we define as the expansion factor:

$$\alpha(p)=\frac{\text{mean expanded area of the cylinder } A_{ex}}{\text{nonexpanded area of the cylinder } A_0}.$$

$\alpha(p)$ is a function of pressure. The relative change of the area of the cylinder with pressure is

$$\frac{\Delta A}{A_0}=\frac{A_{ex}-A_0}{A_0}=\alpha(p)-1. \tag{1}$$

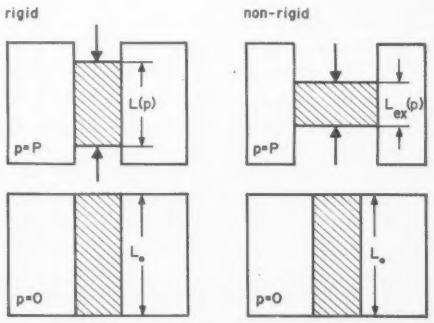

FIGURE 1. *Deformation of sample under pressure with and without deformation of cylinder.*

[1] Figures in brackets indicate the literature references at the end of this paper.

We further assume that the pressure is uniform throughout the sample, that the end faces of the sample are plane, and that the cylinder remains straight.

The expansion of the cylinder does not change the volume $V(p)$ which the sample assumes at pressure p, so that

$$V(p)=A_0L_0(1-Kp)=A_{ex}L_{ex}(p) \tag{2}$$

where $L_{ex}(p)$ is the length of the sample in the expanded cylinder at pressure p, L_0 is the sample length at zero pressure, and K is the compressibility of the sample (see fig. 1). Whence follows

$$\alpha(p)=\frac{A_{ex}}{A_0}=\frac{L_0(1-K(p)\cdot p)}{L_{ex}(p)}=\frac{L(p)}{L_{ex}(p)} \tag{3}$$

According to eq (3) the distortion of the cylinder and the change of area could then be obtained from a measurement of the actual length of the sample and a computation of the uniaxial compression of the sample in a rigid-walled cylinder based on the compressibility $K(p)$ of the sample material.

3. Determination of Sample Length $L(p)$ for Uniaxial Compression

At low pressures, where the compressibility of the sample placed in a rigid cylinder is constant, its length $L(p)$ is

$$L(p)=L_0(1-Kp). \tag{4}$$

Generally K is a function of pressure and, if this function is known, $L(p)$ may be computed from

$$L(p)=L_0\left(1-\int_0^p K(p)dp\right). \tag{5}$$

Although data of compressibility versus pressure have been reported for a number of materials, the agreement between different sources for the same material is often very disappointing. It is desirable to use materials with small compressibilities to reduce the uncertainty in the determination of $L(p)$.

The choice of materials is also narrowed down by the fact that the present purpose requires a material with low yield strength to ensure a more nearly hydrostatic stress pattern.

Typical uncertainties in $L(p)$ caused by an uncertainty of 10 percent in the compressibility of the material are 0.1 percent for nickel at 20 kbar and 3 percent for the more compressible tellurium at 40 kbar.

In 1957 R. K. Cook published a paper [2] dealing with the variation of the elastic constants and static strains with hydrostatic pressure and their calculation from ultrasonic measurements. The final equation reported in that paper relates the sample length at the hydrostatic pressure p with the fundamental resonance frequencies of the same sample measured as a function of pressure for longitudinal and shear waves propagating along the axis of the cylindrical sample:

$$\frac{L_0}{L(p)}=1+\frac{1+\Delta}{3h_0}\int_0^p\frac{dp}{f_l^2-\frac{4}{3}f_s^2} \tag{6}$$

where L_0 is the length of sample at zero pressure

$L(p)$ is the length of sample at pressure p

$h_0=4L_0^2\rho_0$

f_l, f_s are the resonance frequencies for longitudinal and shear waves, and

$$\Delta=\frac{K_{is}}{K_{ad}}-1 \tag{7}$$

where K_{ad} is the adiabatic bulk compressibility

K_{is} is the isothermal bulk compressibility

$h_0(f_l^2-\frac{4}{3}f_s^2)$ is essentially the adiabatic bulk modulus $B_{ad}=K_{ad}^{-1}$.

In the derivation ot eq (6) two approximations were made

$$\frac{\left(1-\frac{1}{3}pK(p)\right)^2}{(1-pK(p))}\approx 1 \tag{8}$$

and

$$\frac{1}{1-\frac{1+\Delta}{3}\int_0^p K(p)dp}\approx 1+\frac{1+\Delta}{3}\int_0^p K(p)dp \tag{9}$$

In the case of very compressible materials like tellurium the first approximation leads to a value of $L(p)$ that is too large by a few tenths of 1 percent at 40 kbar. An error of similar magnitude but opposite sign is introduced if Δ in eq (6) is neglected. The second approximation can be avoided by rewriting eq (6). With less compressible materials like, for example, nickel, both corrections amount to less than 0.1 percent in $L(p)$. This indicates again that materials with low compressibility are to be preferred for such measurements.

Equation (6) permits the computation of the length of a sample subjected to hydrostatic pressure from the resonance frequencies obtained over the entire pressure range. The same equation less the factor 3 in the denominator in front of the integral holds for a sample contained in a rigid cylinder and compressed longitudinally.

If the measurement is made in a nonrigid cylinder where the length of the sample is reduced by α^{-1} due to cylinder expansion, eq (6) has to be corrected by multiplying $h_0=4.L_0^2\rho_0$ with $\alpha(p)^{-2}$. Since $\alpha(p)$ is a function of pressure it has to be written under the integral. Equation (6) for a nonrigid cylinder then becomes

$$\frac{L_0}{L(p)}=1+\frac{1+\Delta}{h_0}\int_0^p\frac{\alpha^2(p)dp}{f_1^2-\frac{4}{3}f_s^2}. \tag{10}$$

$\alpha^2(p)$ does not differ appreciably from unity. To facilitate the solution of eq (10) we assume that $\alpha(p)$ is a linear function of p

$$\alpha(p)=1+\beta p;\ \beta=\frac{\delta\alpha}{\delta p},$$

and we use an estimated value for β in the actual numerical evaluation of this and related equations.

$L(p)$ obtained from eq (10) can be combined with an $L_{ex}(p)$ obtained from dial gage measurements of the sample length as described in section 6 to yield the expansion factor:

$$\alpha_1(p)=\frac{L_0}{L_{ex}(p)}\frac{1}{1+\frac{1+\Delta}{h}\int_0^p\frac{\alpha^2dp}{f_1^2-\frac{4}{3}f_s^2}}. \tag{11}$$

Instead of using ultrasonic measurements in a solid-filled piston cylinder device to determine $L(p)$, a sample length $L^B(p)$ could be determined under hydrostatic conditions with higher precision and then be converted to the hypothetical length $L(p)$ with the help of the relation

$$\frac{L_p^B-L_0^B}{L_0^B}=\frac{L(p)-L_0}{3L_0}, \tag{12}$$

and the equation for $\alpha(p)$ is then

$$\alpha_2(p)=\frac{L_0}{L_{ex}(p)}\left[\frac{3}{1+\frac{1+\Delta}{3h}\int_0^p\frac{dp}{f_1^{B^2}-\frac{4}{3}f_s^{B^2}}}-2\right]. \tag{13}$$

The superscript B in these equations denotes values obtained under hydrostatic conditions.

Equations (12) and (13) are not very sensitive to errors made in the determination of the frequencies or the compressibility derived from them as long as materials with low compressibility are used. The main source of error is the determination of $L_{ex}(p)$. In a particular experiment to be described below an error of 25 μm in the determination of $L_{ex}(p)$ would cause an error in the change of area, ΔA, of more than 30 percent.

4. Determination of Actual Sample Length $L_{ex}(p)$ from Ultrasonic Measurements

In equations (11) and (13) the sample lengths computed for the rigid-walled cylinder were combined with an actual sample length obtained from dial gage readings. If, from ultrasonic measurements under hydrostatic conditions, both the shear and the longitudinal wave velocity (v) are known, these, together with the resonance frequencies or the times of flight (τ) through the sample in the solid-filled cylinder, can be used to determine the actual length of the sample:

$$L_{ex}(p)=\frac{v}{2f}=v\tau. \tag{14}$$

Two values for $L_{ex}(p)$ are obtained; one from shear waves and the other from longitudinal waves. The precision required in f is rather high. An uncertainty of less than 0.1 percent is necessary and 0.01 percent is desirable at the highest pressures.

The two values thus obtained for $L_{ex}(p)$ can be combined with the two values for $L(p)$ used in eqs (11) and (13) in four different ways to yield:

$$\alpha_3(p)=\frac{L_0f_1}{L_0^Bf_1^B}\frac{1+\frac{1+\Delta}{3h_0}\int_0^p\frac{dp}{f_1^{B^2}-\frac{4}{3}f_s^{B^2}}}{1+\frac{1+\Delta}{h_0}\int_0^p\frac{\alpha_2dp}{f_1^2-\frac{4}{3}f_s^2}} \tag{15}$$

$$\alpha_4(p)=\frac{L_0f_s}{L_0^Bf_s^B}\frac{1+\frac{1+\Delta}{3h_0}\int_0^p\frac{dp}{f_1^{B^2}-\frac{4}{3}f_s^{B^2}}}{1+\frac{1+\Delta}{h_0}\int_0^p\frac{\alpha_2dp}{f_1^2-\frac{4}{3}f_s^2}} \tag{16}$$

$$\alpha_5(p)=\frac{L_0f_1}{L_0^Bf_1^B}\left[1-\frac{2}{3}\frac{1+\Delta}{h_0}\int_0^p\frac{dp}{f_1^{B^2}-\frac{4}{3}f_s^{B^2}}\right] \tag{17}$$

$$\alpha_6(p)=\frac{L_0f_s}{L_0^Bf_s^B}\left[1-\frac{2}{3}\frac{1+\Delta}{h_0}\int_0^p\frac{dp}{f_1^{B^2}-\frac{4}{3}f_s^{B^2}}\right] \tag{18}$$

The expressions in brackets are very close to unity and, especially with materials of low compressibility, do not contribute very much to the total uncertainty. L_0 and L_0^B, the initial sample lengths, can be measured with sufficient precision. The main source of error is in measuring the resonance frequencies. While the frequencies in hydrostatic environments can often be reproduced to better than 0.01 percent at 20 kbar no such claim can be made for our solid-filled cylinder assemblies where a scatter of the data of up to 1 percent was encountered. In planned future work a

very definite improvement is expected from improved ultrasonic techniques and choice of more suitable materials.

5. Description of Pressure Equipment and Pressure Determination

A diagrammatic sketch of the equipment is shown in figure 2. The cylinders used were made from cemented tungsten carbide with 6 percent cobalt. Radial support was provided by hardened steel support rings with an interference fit. Axial support was provided by end-loading applied to the carbide cylinder through a bridge plate resting on extensions of a thick cylinder wall of a ram with a 15 cm diam piston. This ram operated on the high pressure piston through a hole in the bridge plate. Rotation of the high pressure piston and 15 cm diam piston is accomplished by a handle passing between the cylinder wall extensions. Both the end loading force and the 15 cm diam piston force are supplied by the large press in which this equipment is inserted. Transition pressure measurements were made in this equipment using a high pressure cylinder 5 cm long with a bore of 1.26 cm. Quartz transducers were mounted as shown in figure 2. In the 5 cm long cylinder a carbide filler rod was used to give the desired sample length for an entrance of the movable piston of about 0.1 cm at zero ram force. This additional member in the path of the ultrasonic signal was undesirable. It was later eliminated by the use of a 1 cm long cylinder as shown in figure 3.

Piston displacement was measured with a dial gage indicator mounted on the cylinder rim and bearing against an extension of the rotation handle. The displacement read is the sum of the movement of the sample end of the high pressure piston, the compression of the high pressure piston, and the compression of the carbide pieces which back up the piston. The movement of the sample end of the high pressure piston is due to compression of the sample, expansion of the cylinder, and, if used, the carbide filler rod.

In the 5 cm long cylinder a sample was compacted from tellurium powder with a particle size of 50 μm or less. The length after compaction to 40 kbar was 0.6858 cm. Conical steel rings were used to prevent extrusion. The transition pressure with rotation (approximately two degree oscillation) was determined to be 40 kbar. In the 1 cm long cylinder a nickel sample, machined to fit, was used for measurements to 20 kbar. For the ultrasonic measurements the equipment was operated without rotation.

The determination of internal pressure requires correction for friction and the determination of sample length requires correction of sample length for compression of various members. Figure 4 shows a typical curve of uncorrected dial gage reading against uncorrected increasing and decreasing pressure. The dashed line to A is the calculated change in dial gage reading with pressure due to the compressibility

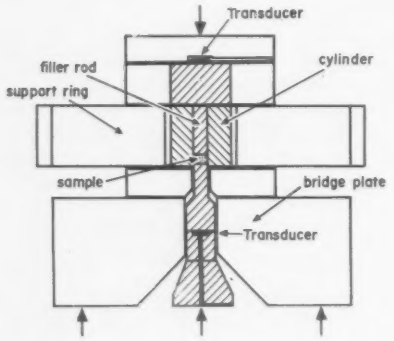

FIGURE 2. *Long cylinder.*
Tungsten carbide parts hatched. Sample marked by dotted area.

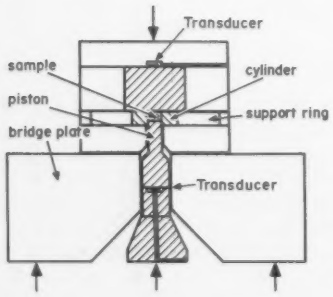

FIGURE 3. *Short cylinder.*
Tungsten carbide parts hatched. Sample marked by dotted area.

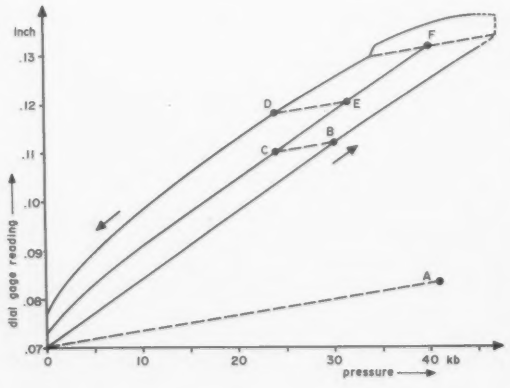

FIGURE 4. *Change of length of tellurium sample as indicated by dial gage reading and correction to internal pressure.*

of the carbide high pressure piston and its supporting pieces. A modified mean curve for the pressure on the tellurium is drawn to point F, the start of a transition. The corrected pressure is obtained by following a line with a slope equal to that of line "A" from an observed point B or D to the intersection with the modified mean curve (points C or E) respectively. These corrected pressures are used with the observed frequencies for the ultrasonic computations.

6. Determination of the Measured Sample Length, $L_{ex}(p)$

The measured sample length, L_{ex}, is obtained by applying a correction to the dial gage reading for the compression of the various carbide members. For pressures to 20 kbar a constant value of Young's modulus for the carbide of 5.93×10^3 kbar was used. For pressures from 20 to 40 kbar a decreasing Young's modulus was used.

The effects of uncertainties in L_{ex} on α are computed for a 5 percent uncertainty in Young's modulus and for a 10 percent uncertainty in the estimate of effective length of the compressible carbides including the tapered piston and the backup pieces of various cross-sections. These effects on $\alpha(p)$ are larger in the tellurium measurements than in the nickel measurements primarily because of the greater length of compressible carbide in the tellurium measurement and secondarily because of the shorter sample length of the tellurium. These uncertainties in $\alpha(p)$ due to L_{ex} are shown in figures 7 and 8 and will be discussed later.

7. Derivation of Expansion Factor $\alpha(p)$ from Elastic Theory

The expansion of the bore of a long thick-walled cylinder due to internal pressure p is

$$\frac{\Delta d}{d} = \frac{p}{E} \frac{(1-\mu) + (1+\mu) W^2}{W^2 - 1} \tag{19}$$

where E is Young's modulus, μ is Poisson's ratio, and W is the ratio of the outer diameter to inner diameter of the cylinder.

The cylinder used with the tellurium had a wall ratio, W, of 4 and a length of 5 cm with only 0.686 cm or about one radius of that length exposed to internal pressure.

A proportionality factor, F, to be applied to eq (19) for this pressure distribution is computed using values of tangential strain at the inner surface of a cylinder for a semi-infinite zone of internal pressure from the "Thick Walled Cylinder Handbook" [1]. For a long cylinder with internal pressure over a length equal to one radius starting at one end, the proportional expansion is computed by assuming a mirror image of the cylinder at the pressurized end of the cylinder. In Figure 5 curves (a and b) are drawn for semi-infinite

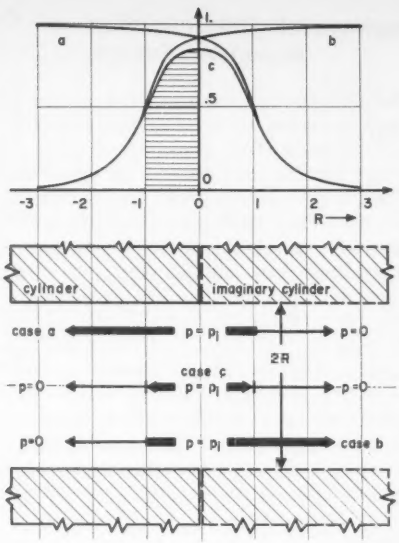

FIGURE 5. *Derivation of cylinder expansion from the distortion caused by reflected semi-infinite zones of internal pressure.*

pressure zones starting at the original and reflected pressure discontinuities. Curve c is the product of "a" and "b" and is an approximation for the factor for a pressurized zone of length $2R$ in a long cylinder.

A mean value of 0.75 is taken to apply to the expansion calculated from eq (19). $\alpha(p)$ is computed using the above factor and a Young's modulus of 5.79×10^3 kbar for pressures 0 to 20 kbar and a decreasing Young's modulus for pressures of 20 and 40 kbar. The computed $\alpha(p)$ for the cylinder used with the tellurium sample is shown in figure 7. The effects of a 5 percent uncertainty in E and a 33 percent uncertainty in F are shown.

The 1 cm long carbide cylinder used with the nickel sample has a wall ratio $W = 3$. Equation (19) is used neglecting the increase in effective W due to the steel rings and the variation of the expansion of this short section from that of a long cylinder. For a value for E of 5.97×10^3 kbar and a μ of 0.25:

$$\frac{\Delta d}{d} = 0.00503 \text{ at } 20 \text{ kbar}$$

$$\frac{\Delta A}{A} = \alpha - 1 = 0.0101 \text{ at } 20 \text{ kbar}.$$

An estimated uncertainty of 5 percent in E results in a 5 percent uncertainty in $\alpha - 1$ and this is shown in the value of α in figure 8. No value is included for the uncertainty introduced by applying the theory for elastic distortion of long cylinders to a short section and neglecting the friction effects at the end faces.

237-679 O-67—2

8. Experimental Determination of Cylinder Expansion Factors

For the ultrasonic measurements in the solid-filled piston and cylinder assemblies the signal had to be generated outside the pressurized zone, radiated through the sample and picked up again outside the pressurized zone. Since plane and parallel interfaces along the ultrasonic path are necessary for all precise measurements, the signal could only be radiated along the longitudinal axis of the apparatus. Figures 2 and 3 show how the 10 MHz quartz transducers were arranged. One transducer was used for shear, the other for longitudinal waves. Part of the signal originating from a transducer is reflected at the tungsten carbide-sample interface, the rest travels through the sample and undergoes another reflection at the sample-tungsten carbide interface. The returning echoes plus usually several artifacts were picked up by the same transducer. The signal was then amplified and displayed on the screen of an oscilloscope without demodulation.

The delay time caused by the sample was measured in two ways: At high attenuations a short pulse was used and the time between the reflection from the front (tungsten carbide-sample) interface and the rear (sample-tungsten carbide) interface was measured by displaying the rf-pulse on the screen of an oscilloscope and using the variable sweep delay to let the pulses successively coincide with a mark on the screen. The transit times could thus be determined with a sensitivity of ± 20 ns. At low values of attenuation in the samples the phase comparison method developed by McSkimin [3] was used. The pulse length was adjusted to provide sufficient overlap of succeeding pulses and the rf-frequency was adjusted for destructive interference. At constant pressure the critical frequencies could usually be reset to ± 1 kHz at 10 to 12 MHz.

The electronic equipment consisted of an rf-cw-generator, a gated amplifier and, on the receiver side, a wide-band rf-amplifier and a wide band oscilloscope. The transducers were connected to the circuit through a tuned transformer bridge.

The same electronic equipment was also used for ultrasonic measurements with a nickel sample under hydrostatic pressure. In this case only the phase comparison method was used. The sample was cemented between two fused quartz buffer rods with a shear and a longitudinal mode transducer attached to either end.

Figure 6 shows a typical plot of transit time versus uncorrected pressure obtained in a solid-filled cylinder. The large amount of hysteresis is due to the friction between the piston and the cylinder. In section 5 we have already described how the uncorrected pressure is related to the internal pressure. This relation is now used to re-plot the ultrasonic data versus internal pressure. The result is, in the case of shear waves in tellurium, a single curve for increasing and decreasing pressure. In some cases the results were less satisfactory. Transit time data are read from the final curves at intervals of 1 kbar to be used for the computation of the cylinder expansion.

The results of two such computations are shown in figures 7 and 8. Figure 7 is for the long cylinder shown in figure 2 filled with sintered tellurium powder compacted at 40 kbar. The expansion factor computed from elastic theory is shown as a solid line. The uncertainty is schematically indicated by the vertically hatched area. Data for the expansion factor computed from ultrasonic measurements and measurements of sample length are entered as black dots. The total of the estimated uncertainties of the measured length is schematically indicated by the horizontally hatched area. The estimated uncertainty introduced by the ultrasonically measured $L(p)$ is considerably smaller. Also entered in figure 7 are the adiabatic compres-

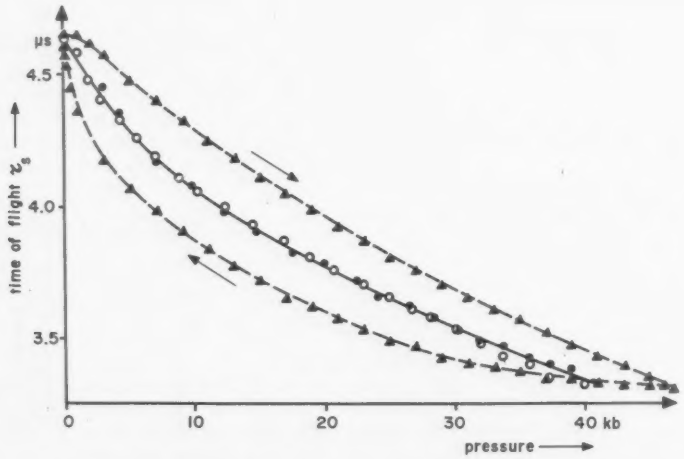

FIGURE 6. *Time of flight for shear waves in tellurium as function of increasing, decreasing and corrected internal pressure.*

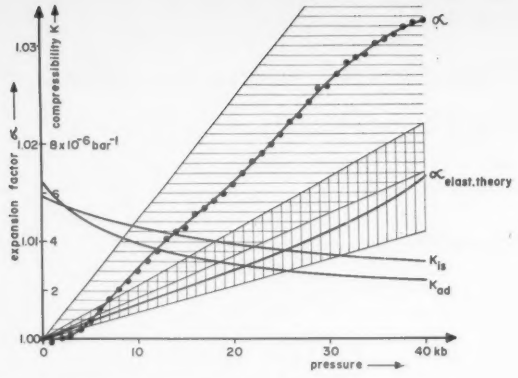

FIGURE 7. *Cylinder expansion with tellurium sample in long cylinder.*
Areas of uncertainty hatched.

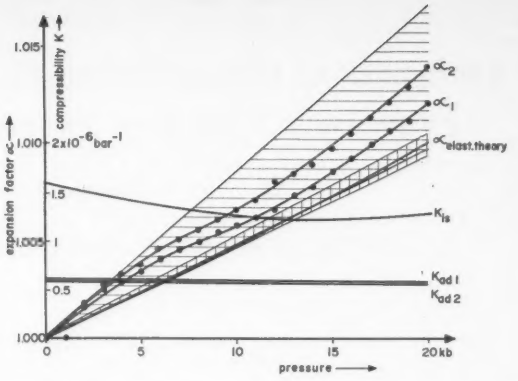

FIGURE 8. *Cylinder expansion with nickel sample in short cylinder.*
Areas of uncertainty hatched.

sibility K_{ad} obtained from the ultrasonic measurement and the isothermal compressibility K_{is} obtained from the dial gage reading. The latter includes the effect of cylinder expansion and is therefore not a correct value.

The overall uncertainty in this determination is extremely large. The greater part of the uncertainty is due to the determination of $L_{ex}(p)$ from the dial gage measurements. This fact emphasizes the need for an improved way to measure the actual length of the sample under pressure.

Figure 8 presents the results obtained with a short cylinder filled with nickel. The uncertainties are indicated in the same way as in figure 7. The overall uncertainties are relatively much smaller. This is partly due to the improved design of the cylinder and partly to the smaller compressibility of the sample. The precision of the ultrasonic measurements was improved over that with tellurium. Consequently the disagreement between the measured and the computed values for α is much smaller. Again the compressibilities are entered.

9. Conclusion

The experimentally determined expansions for both the long and the short cylinder are larger than the expansions computed from elastic theory. The same relation was reported by Bridgman [4] for his experimental determinations of cylinder distortion under various conditions. Therefore, a more rigorous computation of elastic distortion of short cylinders, including end effects and other modifications, seems to be desirable. While this mathematical solution does not seem to be very near at hand, the main effort will have to be in the direction of improved ultrasonic measurements with carefully selected materials in various piston-cylinder devices. The application of ultrasonic measurements to the determination of cylinder distortion as proposed in this paper will then lead to more meaningful and more precise data.

10. References

[1] P. P. Kadkowski, J. I. Bluhm, O. L. Bowie, Watertown Arsenal Laboratory, "Thick-Walled Cylinder Handbook," figures 6A and 6B.
[2] R. K. Cook, J. Acoust. Soc. Am. **29**, 445 (1957).
[3] H. J. McSkimin, J. Appl. Phys. **24**, 988 (1953).
[4] P. W. Bridgman, Proc. Am. Acad. Arts Sci. **74**, 1 (1940).

(Paper 71C1–439)

JOURNAL OF RESEARCH of the National Bureau of Standards—C. Engineering and Instrumentation
Vol. 71C, No. 1, January–March 1967

A Comparison of Absorbed Dose Determinations in Graphite by Cavity Ionization Measurements and by Calorimetry*

Ben Petree and Paul Lamperti

Institute for Basic Standards, National Bureau of Standards, Washington, D.C. 20234

(September 27, 1966)

The absorbed dose in graphite from a cobalt-60 gamma-ray source was measured with a spherical air-filled cavity ionization chamber and with two spherical calorimeters. The instruments were constructed from high-purity graphite. The current per unit mass of air and the absorbed power per unit mass of graphite were determined with uncertainties of 0.40 and 0.17 percent respectively. When the two results are combined the value of $W_{air} \cdot \bar{s}_m$ is found to be 33.72 electron volts in graphite per ion pair in air, with an uncertainty of ± 0.14 electron volts.

Key Words: Absorbed dose, calorimeter, cavity ionization chamber, cobalt-60 gamma rays, comparison, graphite, $W \cdot \bar{s}_m$.

1. Introduction

Ionization techniques are often employed for the determination of radiation exposure and absorbed dose. Especially for photons in the megavolt region, the instrument of choice is a cavity ionization chamber. For absolute determinations of exposure with such a device the effective stopping power ratio, $\bar{s}_m$, contributes the largest single uncertainty—about 0.5 to 2 percent [1].[1] For absorbed dose determinations with a cavity chamber the principal contributors to the uncertainty are the stopping power ratio and the value of W, the average energy required to produce an ion pair in the gas. For air, the uncertainty in W is about 0.4 percent [1]. Higher accuracy for such determinations therefore necessitates a reexamination of the values of W and $\bar{s}_m$. The present investigation in which measurements are made, both with the ionization technique and with the calorimetric technique of the same beam of cobalt-60 gamma rays, provides data on $W \cdot \bar{s}_m$.

When the necessary conditions of homogeneity in the material and uniformity of primary radiation are satisfied the relation [2] between ionization and energy deposited is given by the Bragg-Gray equation:

$$\frac{P}{M} = W \cdot \bar{s}_m \cdot \frac{I}{m} \tag{1}$$

where $\frac{I}{m}$ is the ionization current produced by the radiation per unit mass of cavity gas and $\frac{P}{M}$ is the power deposited by the radiation per unit mass of the absorbing material. If $\frac{I}{m}$ and $\frac{P}{M}$ are given in amperes per gram of gas and watts per gram of absorbing material respectively, then W is to be given in electron volts per ion pair. In the experiments to be described in this paper the values of $\frac{P}{M}$ and $\frac{I}{m}$ were measured with small graphite calorimeters and an air-filled graphite wall cavity ionization chamber respectively, using cobalt-60 gamma radiation. The quotient of the measured values of $\frac{P}{M}$ and $\frac{I}{m}$ constitutes an experimental determination of the effective value of the product $W \cdot \bar{s}_m$ in terms of mass and electrical units. Such pairs of measurements have been made most recently by Bewley [3] and previously by Bernier et al. [4], and by Reid and Johns [5]. The present experiment repeats work that was done earlier in this laboratory [6] but with improved procedures that result in increased accuracy.

2. Apparatus

2.1. Radiation Source

The source of radiation for these measurements was a cylindrical assembly of twelve encapsulated cobalt-60 pencils, each a half-inch in diameter and 6 in long, containing about 1000 Ci (curies) in all. The pencils are mounted upright on a steel base plate and are spaced equally around a 4⅛ in diam circle of centers. This assembly is mounted near the bottom of a square concrete cistern 6 ft on a side in the laboratory floor. The source is covered by water to a depth of 10 ft. The ion chamber and calorimeter were mounted in a watertight can and, during measurements, were placed at the geometric center of the

*This work was supported by the Division of Biology and Medicine of the United States Atomic Energy Commission.

[1] Figures in brackets indicate the literature references at the end of this paper.

source. The exposure rate at that point was about 55 roentgens per second.

The exposure rate is fairly uniform near the center of the source. For example, the average exposure rate within a spherical volume 1.5 cm in diameter, which is the approximate inside dimension of the instruments, is only about 0.01 percent greater than at the center.

The spectrum of photons inside the can was examined and found to have approximately the composition given in table 1 [7].

TABLE 1. *Spectrum of cobalt-60 source*

Component	Fraction of intensity	Energy
Primary photons	0.80	1.17 MeV and 1.33 MeV
Singly scattered photons	.18	0.21 MeV to 1.33 MeV
Multiply scattered photons	.02	0.105 MeV (effective energy)

This description of the source is clearly not unique. For example, Ritz and Attix, studying a nearly identical source, found that the responses they obtained with a set of energy-dependent chambers could be adequately explained by assuming a scattered intensity of 1.7 percent at 169 keV and a primary radiation of 98.3 percent [8].

2.2. Calorimeter

The two adiabatic calorimeters used in these measurements each comprise two main parts; a spherical calorimetric body, or core, and a spherical enclosing shell. They are similar to one previously described [6, 9]. Figure 1 shows the essential dimensions and details of one of the present instruments. A thermocouple, T_1, is inserted in a shallow hole in the core and securely fastened. It is used to measure changes in core temperature with respect to reference junctions held at a constant temperature. Thermocouples T_2 and T_3, which are attached to the core and shell respectively, are connected in opposition and permit the measurement of temperature differences that may develop between the core and the shell during measurements.

Two cores differing in thickness were used in order to be able to determine whether or not the attenuation of the gamma rays within the core was properly evaluated. One core was made of solid hemispheres that were joined together by a film, H_1, of electrically conductive resin. The resistor thus formed measured about 100 Ω. It was used as a source of heat for calibrating changes in potential of T_1 in terms of energy input to the core. The second core was made of two hollow hemispheres having the same outer diameter as the first, but only about two-thirds the mass. These were joined in the same way as the first. The cores were carefully weighed at each step of assembly and the composition by weight of each component is given in table 2.

TABLE 2. *Composition by weight of calorimeter cores*

Component	Solid core		Hollow core	
	Mass	Fraction	Mass	Fraction
	Gram		*Gram*	
Graphite	0.9058_0	0.9945	0.5946_1	0.9929
Conducting resin	$.0004_8$	.0005	$.0000_1$	.0000
Copper spots	$.0002_9$	.0002	$.0001_7$	.0003
Epoxy	$.0009_1$	.0010	$.0007_8$	.0013
Copper wire	$.0002_9$	.0003	$.0001_8$	.0003
Thermocouples	$.0031_2$	.0034	$.0031_1$	.0052
Total	0.9108_0	0.9999	0.5988_6	1.0000

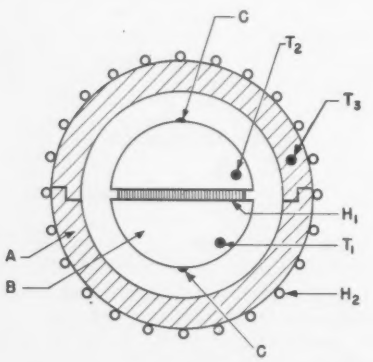

FIGURE 1. *Spherical graphite calorimeter with solid core.*
A Shell: Outer diam, 2.05 cm; inner diam, 1.28 cm; graphite.
B Core: Diam, 1.00 cm; graphite.
T_1, T_2, T_3, Thermocouples: Constantan versus chromel P; 0.003 in diam wires imbedded in holes with epoxy resin.
H_1 Core heater made of electrically conducting resin.
C Copper spots. A No. 43 copper wire was attached to each spot with epoxy resin.
H_2 Shell heater. Karma resistance wire. Diam, 0.003 in. Attached to shell with epoxy resin. Space between wires is about 0.2 cm.

The calorimeter shells were also made in halves that fit tightly together. The thickness was sufficient to stop electrons generated outside the shell by cobalt-60 photons. Four hollow polystyrene spheres of about 1.5 mm diam were cemented to the inside surface of the shell to hold the core in the central position. An insulated wire heater, H_2, was wound over the outer surface of the shells and attached with epoxy resin. An adjustable current generated heat in the winding so as to permit control of the shell temperature. Control was automatic during the measurements, and kept the shell temperature equal to that of the core.

The graphite of which the calorimeters and ion chamber were made was a reactor grade material, a sample of which left a residue of 0.014 percent when ashed in a muffle furnace. Calcium, vanadium, and titanium were the principal constituents detected by spectrographic analysis of the residue. This level of impurity has no significant effect upon the observed gamma-ray heating rates. The density of a sample of the graphite was 1.76 g per cm^3.

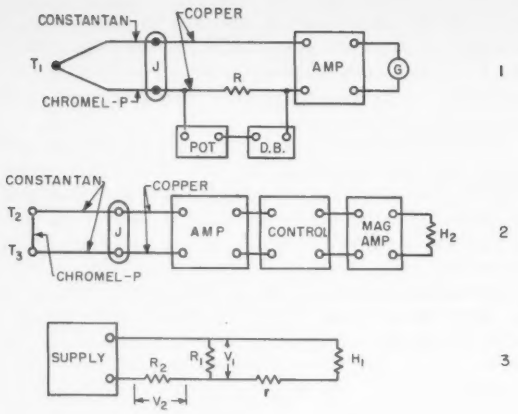

FIGURE 2. *Electrical circuits used with calorimeters.*
(1) Core temperature measurement. T_1, core thermocouple; J, constant temperature reference cell; R, 10 Ω manganin standard; POT, 0–1.6 V potentiometer; D.B., 5 dial decade resistor, 0 to 111,110 Ω; AMP, contact modulated d-c amplifier; G, microammeter with zero at center of scale.
(2) Shell temperature control. T_2, core thermocouple; T_3, shell thermocouple; J, constant temperature reference cell; AMP, contact modulated d-c amplifier; CONTROL, 3-mode current adjusting controller; MAG AMP, magnetic amplifier; H_2, shell heater winding.
(3) Electrical calibration. SUPPLY, constant current generator; R_1, R_2, wirewound resistors; r, copper lead wires; H_1, core heater.

Three electrical circuits were required for operating the calorimeters. They are shown in figure 2 and functioned as follows:

(1) *Core temperature measurement.* The EMF of the thermocouple, T_1, attached to the core was measured by balancing it with an EMF developed by a simple Lindeck circuit consisting of a manganin 10 Ω standard resistor, R, a five dial decade resistor and a potentiometer set at 0.3 V. Adjustments in the decade resistance were made to provide a range of potentials of from about 45 to 175 μV across R. The null detection system consisted of a contact modulated d-c amplifier and a galvanometer. The connections of the thermocouple wires to the copper lead wires at J were kept at a steady reference temperature of 26.8 °C by immersing them in oil in the central tube of a glass cell containing solidifying diphenyl ether [10].

(2) *Shell temperature control.* The EMF of the opposed thermocouple pair, T_2 and T_3, was amplified by a second contact modulated amplifier in order to obtain indications of temperature differences between the shell and the core. During normal calorimeter operation the EMF was kept equal to zero by the action of a three-mode controller and a magnetic amplifier that regulated the current flowing through the heater winding, H_2, of the shell. The calorimeters were operated a few degrees C above the temperature of the surroundings, so that the electrical heat supplied to the shell could be balanced by radiative and convective heat loss.

(3) *Electrical calibration.* This circuit provided power to the core heater, H_1, and so permitted calibration of the core temperature indications in terms of added energy. Since it was observed that the core resistance increased slightly as the temperature rose during a measurement, a power stabilizing arrangement was employed consisting of a constant current source, and a calibrated stabilizing resistance, R_1, shunting the heater. A calibrated resistor, R_2, was also included as shown. A calibrated potentiometer was used to measure the voltages, V_1 and V_2, that developed across R_1 and R_2. To give the desired stabilizing effect the resistance of R_1 was adjusted to be equal to that of the core heater, H_1; for convenience in measurement, the resistance of R_2 was adjusted to be one-half that of R_1, so that V_1 was nearly equal to V_2.

2.3. Graphite Cavity Ionization Chamber

The important dimensions and details of the cavity ionization chamber are shown in figure 3. The wall thickness is equal to that of the calorimeter shells. The inner and outer surfaces of the chamber are spherical except at the end where the instrument is supported. The cylindrical collecting rod has a spherical enlargement at the end to reduce the electric field strength in that vicinity and thus make the field strength more uniform throughout the cavity.

To obtain the volume of the cavity in the graphite shell it was weighed both when empty and when filled with distilled water. The volume of the cavity was then determined as the quotient of the observed mass of added water by the density of water at the corresponding temperature. Water was excluded

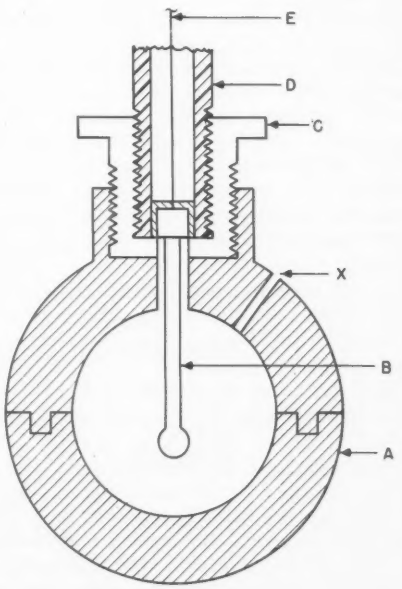

FIGURE 3. *Spherical graphite wall cavity ionization chamber.*
A Graphite wall assembly. Outer diam, 2.07 cm; inner diam, 1.27 cm.
B Graphite collecting electrode. Diam, 0.1 cm; diam of ball, 0.2 cm; length, 1.1 cm.
C Polystyrene high voltage insulator.
D Aluminum supporting stem with insulating plug to hold collecting electrode. Evacuated.
E Current lead to electrometer.
X Air vent.

from the air vent with a plug during the weighings. Corrections were made for atmospheric buoyancy acting on the added water. We believe there was no significant absorption of water into the graphite because the weight of the shell immediately after being emptied of water and wiped dry was not significantly different from the weight after the shell was kept overnight in vacuum.

Five determinations of the cavity volume were made, including one in which the cavity was filled with mercury rather than water. The results are given in table 3.

TABLE 3. *Volume of ionization chamber cavity*

Cavity filling	Computed volume
	cm^3
Water	1.0839
Mercury	1.0773
Water	1.0770
Water	1.0771
Water	1.0800
Average	$1.07_{91} \pm 0.001_3$ [a]

[a] Standard error of the average.

The volume of the collecting electrode was calculated from its measured dimensions to be 0.0128 cm^3. This was subtracted from the average determined above to give the volume of air within the assembled chamber.

The ionization current from the chamber was determined by measuring the corresponding voltage drop that it produced in flowing through a calibrated, wire-wound resistor. A calibrated potentiometer was used for the voltage measurement, with a vibrating reed electrometer for null detection. The collecting voltage was supplied by dry batteries. An aneroid barometer was used to determine the air pressure. A mercury thermometer was used to measure the temperature of the surrounding water. The humidity of the air was shown to have no significant effect on the chamber current [11].

3. Measuring Procedures

3.1. Calorimeter

In both gamma-ray and electrical calibration runs the length of time required for the temperature of the calorimeter core to rise between two arbitrarily selected temperatures was determined. The temperatures corresponded to 160 and 60 μV respectively, as indicated by the core thermocouple. Since the thermoelectric power of the measuring thermocouple was about 60 μV per degree C, the temperature interval amounted to about 1⅔ °C. The time required for the gamma rays to produce this change in temperature was about 40 min.

The final determination of gamma-ray heating power by this method does not require that the end points of the temperature interval be known, but only that they remain fixed during the set of runs. It was convenient, however, to divide the 100 μV interval into fourths so that during electrical calibration runs five power observations could be made at nearly equal intervals of time.

A calibration run was made as follows: The temperature of the calorimeter was raised until a temperature indication of 175 μV was attained, and at that time the automatic shell temperature control was turned on. Several observations, usually seven, of microvoltage were made at intervals of 5 min to determine an initial zero-power drift rate. The electrical calibrating power was then turned on. When a temperature indication of 160 μV was attained (the controller having eliminated the transient shell-core temperature differential), an electronic timer was started, and measurements of V_1 and V_2 were made. V_1 and V_2 were also measured at 135, 110, 85, and 60 μV. The timer was stopped at the 60 μV indication. Calibrating power was turned off at 45 μV. Observations of microvoltage were then made at 5-min intervals as before, to determine a final zero-power drift rate. In reducing the data obtained in each run, the gross drift rate determined by the time interval between the 160 and 60 μV indications was diminished by the average of the initial and final zero-power drift rates so as to obtain a corrected net rate.

For gamma-ray heating runs a similar schedule was followed. The calorimeter, placed near the corner of the pool where the radiation intensity was negligible, was brought to 175 μV and the shell temperature was put under automatic control. Measurements of microvoltage were made for 30 min to determine the initial zero-power drift rate. The calorimeter was then inserted into the source. The timer was started when the temperature indication attained 160 μV, and was stopped when it attained 60 μV. At 45 μV the calorimeter was removed from the radiation source to the corner of the pool and another set of measurements was made of microvoltage to determine the final zero-power drift rate. This measurement procedure was carried out with the calorimeter at different positions along the vertical axis of the source. Repeated measurements were then made at the position of maximum rate of temperature rise.

In this method of calorimetry a systematic error can result if the thermocouple pair used for automatic shell temperature control do not measure the average temperature of the core and shell surfaces to which they are attached. To evaluate this error the calibrations and gamma-ray measurements were done both with the calorimeters evacuated and open to normal atmospheric air. In addition, measurements of the time constants for the relaxation of core-shell temperature differentials with no shell heat were made under conditions of vacuum and atmospheric pressure.

3.2. Cavity Chamber

Preliminary measurements were made of chamber current versus chamber position along the vertical axis of the source to determine the position of maxi-

mum response. At that position the current was measured over a range of collecting potentials up to 540 V to provide the data required for extrapolation to infinite field strength. To eliminate extra-cameral currents each current measurement was made with both positive and negative collecting potentials.

At the time of the measurement the atmospheric pressure was read from an aneroid barometer in the laboratory, and the temperature of the water was read from a mercury thermometer. The thermometer was brought to the surface for reading inside a 1-gal bottle of water. The effect of scattering and attenuation in the chamber neck, insulator and stem was determined by measuring the chamber current with and without an equivalent dummy installed on the opposite side of the chamber.

4. Results

4.1. Calorimetric

The calibrations of the two instruments and the gamma-ray measurements obtained with them are given in table 4. The gamma-ray measurements, which were made during a period extending from January to July 1965, have all been corrected to a common date, March 31, 1965, using 5.24 yr as the half-life of the radiation. The standard error shown with each mean value was computed from the deviations of that set of readings from its mean. It can be seen that the response of these instruments was, in each instance, less when it was operated at atmospheric pressure than in vacuum.

TABLE 4. *Calorimeter measurements*

(i) Calibrations, in microvolts per minute and milliwatt

Solid core		Hollow core	
Vacuum	Air	Vacuum	Air
5.377	5.358	8.204	8.096
5.380	5.357	8.180	8.120
5.370	5.363	8.189	8.164
	5.346	8.202	8.138
	5.344	8.221	8.158
	5.355		
	5.344		
	5.350		
	5.354		
Mean 5.376 ± 0.003 [a]	5.352 ± 0.003 [a]	Mean 8.199 ± 0.007 [a]	8.135 ± 0.013 [a]

(ii) Gamma-ray measurements, in microvolts per minute

Solid core		Hollow core	
Vacuum	Air	Vacuum	Air
2.509	2.507	2.548	2.497
2.503	2.504	2.531	2.525
2.520	2.491	2.544	2.549
2.518	2.493	2.547	2.534
2.522	2.509	2.548	
	2.492		
Mean 2.515 ± 0.004 [a]	2.499 ± 0.003 [a]	Mean 2.544 ± 0.003 [a]	2.526 ± 0.011 [a]

[a] Standard error of the mean.

The results of the temperature relaxation measurements are given in the four curves of figure 4, and

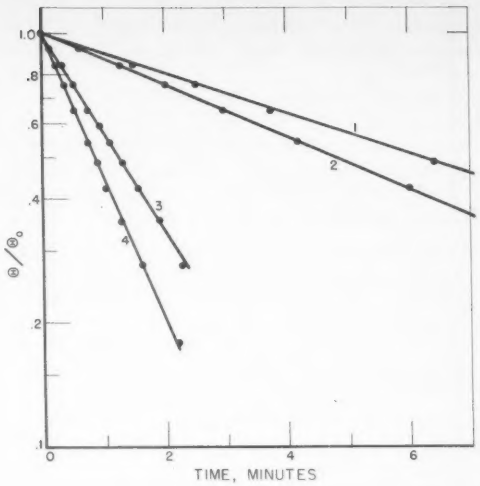

FIGURE 4. *Relaxation of temperature differences between core and shell of calorimeter with no electrical shell heat.*

θ/θ_0 is the fraction of the initial temperature difference. Initial temperature difference was produced by a pulse of heat in the core. Scale of ordinates is logarithmic. 1, solid core in vacuum; 2, hollow core in vacuum; 3, solid core in air; 4, hollow core in air.

show clearly the importance of air as a heat conduction path between core and shell. The relaxation rates (reciprocal of time constant) determined from these data are 0.168 and 0.237 per minute respectively, for the solid and hollow core instruments in vacuum; 0.910 and 1.30 per minute respectively, for the solid and hollow core instruments in air. Since for each calorimeter this relaxation rate is $\lambda = k\left(\frac{1}{C_1}+\frac{1}{C_2}\right)$ min^{-1} where k = core-shell heat transfer coefficient, joules per minute and °C, C_1 = heat capacity of core, joules per °C and C_2 = heat capacity of shell, joules per °C, the relaxation rates obtained above are proportional to the corresponding core-shell heat transfer coefficients.

As was noted from the mean values in table 4, both the electrical and gamma-ray heating rates were affected by the addition of air with its consequent alteration of the core-shell heat transfer coefficient. The correct heating rate that is desired in both determinations is that which would be obtained with no heat transfer to the core. That rate may be arrived at by extrapolating linearly to zero, on a heat transfer scale, the two heating rates measured in air and in vacuum. The extrapolations are shown in figures 5a and 5b and give the values shown in table 5 for the calorimetric results.

TABLE 5. *Extrapolated calorimeter measurements*

Calorimeter core	Gamma-ray heating rate	Calibration
	$\mu V\ min^{-1}$	$\mu V\ min^{-1} mW^{-1}$
Solid	2.519	5.381
Hollow	2.548	8.213

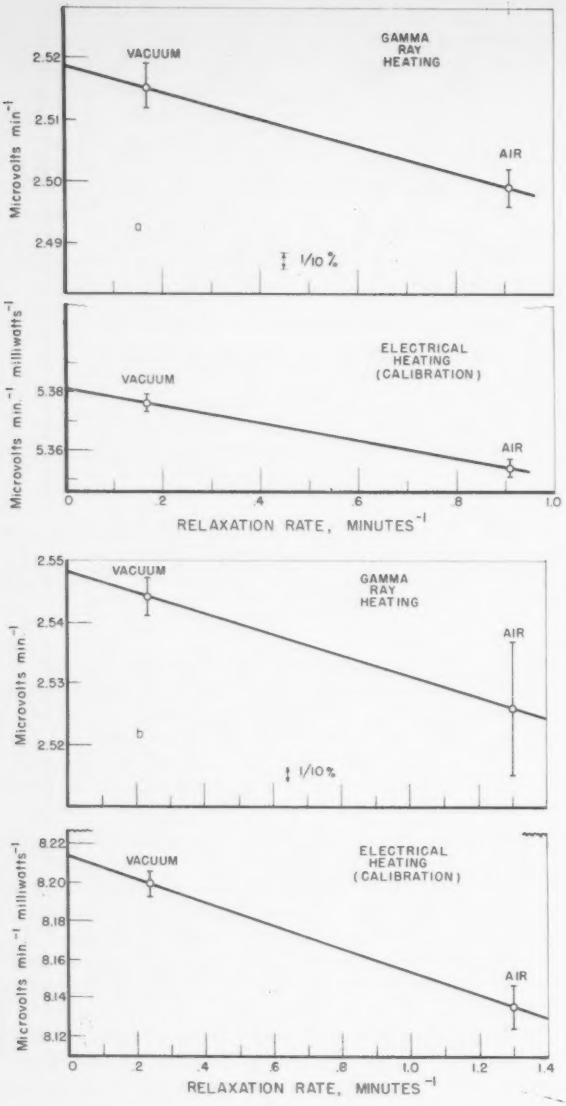

FIGURE 5. *Variation of calorimeter response with core-shell heat transfer coefficient.*

a, solid core; b, hollow core. The abscissae are proportional to the core-shell heat transfer coefficients.

From the values of the calorimetric results, shown in table 5, and the masses given in table 2, the gamma-ray heating powers per gram of the cores are obtained as follows:

(1) Solid Core: $\frac{P}{M}=2.519\times\frac{10^{-3}}{5.381}$

$$\times\frac{1}{0.9108}=0.5140\times10^{-3}Wg^{-1}$$

(2) Hollow Core: $\frac{P}{M}=2.548\times\frac{10^{-3}}{8.213}$

$$\times\frac{1}{0.5989}=0.5180\times10^{-3}Wg^{-1}.$$

4.2. Ionization Measurements

Measurements of ionization current were made at the position of maximum observed response in the source on December 31, 1964, before the calorimetric measurements and on July 16, 20, 21, and 23, 1965, after their completion. The chamber currents observed at a series of collecting potentials were extrapolated to infinite field strength according to the method of Mie [12, 13] to determine the true ionization current in the absence of recombination. From extrapolations similar to those illustrated in figure 6 it was found that the collection efficiency at 540 V was about 0.993. The measurements with and without the dummy stem showed that absorption in the stem reduced the observed current by 0.13 percent. Therefore, the observed currents were increased by the factor $\frac{1.0013}{0.993}$. The density of the air in the cavity chamber was computed using the expression

$$\rho_{air}=0.001293\frac{P}{760}\frac{273.2}{T}\ g/cm^3$$

where

P = observed barometric pressure, mm Hg
T = observed collecting volume air temperature °K.

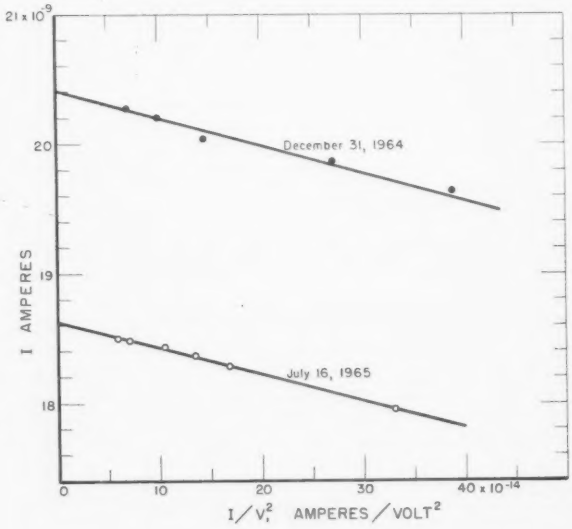

FIGURE 6. *Extrapolation of observed chamber current to infinite field strength.*

I, observed chamber current, amperes; V, collecting potential, volts.

In the air density calculation, 0.4 mm Hg was added to the observed pressure to allow for the difference in altitude between the barometer and the chamber, and 0.2 °C was added to the observed water temperature to allow for the gamma-ray heating of the chamber as measured in a separate experiment.

The mass of air was computed as the product of the volume of the cavity, 1.0663 cm^3, and the density of the air at the time of measurement. The ionization current per unit mass of air was then determined. The observed currents and the results of the computations are shown in table 6. The standard error of the average was computed from the deviations of the individual determinations from the average.

TABLE 6. *Ionization measurements*

Date of measurement	Ionization current				Air density	Mass of air	Current per unit mass of air
	Observed[a]	Corrected[b]	Extrapolated[c]	Referred to 3/31/65			
	$\times 10^{-5}A$	$\times 10^{-5}A$	$\times 10^{-5}A$	$\times 10^{-5}A$	$\times 10^{-3}g/cm^3$	$\times 10^{-3}g$	$\times 10^{-5}A/g$
12/31/64	2.031_5	2.034_1	2.049_2	1.986_0	1.202_8	1.282_5	1.548_6
	2.032_4	2.035_0	2.050_1	1.987_0	1.202_8	1.282_7	1.549_0
7/16/65	1.850_1	1.852_5	1.864_5	1.940_2	1.172_3	1.250_0	1.552_2
	1.851_1	1.853_5	1.865_6	1.941_3	1.173_8	1.251_{6_5}	1.551_1
7/20/65	1.862_3	1.864_8	1.876_9	1.955_5	1.180_6	1.258_9	1.553_4
	1.858_5	1.860_9	1.873_0	1.951_5	1.179_6	1.257_8	1.551_5
7/21/65	1.862_8	1.865_2	1.877_3	1.956_2	1.181_6	1.259_9	1.552_7
	1.855_6	1.857_4	1.869_5	1.948_0	1.178_2	1.256_5	1.550_6
	1.856_6	1.859_0	1.871_1	1.949_6	1.178_6	1.256_1	1.552_1
7/23/65	1.843_4	1.845_8	1.857_8	1.937_7	1.170_5	1.248_1	1.552_5
	1.838_9	1.841_3	1.853_3	1.932_9	1.168_5	1.246_0	1.551_3
Average							$1.551_4 \pm 0.000_5$[d]

[a] At 540 V collecting potential.
[b] Corrected for stem absorption.
[c] Extrapolated to infinite collecting potential.
[d] Standard error of the average.

5. Analysis of Results

5.1. Correction of Calorimetric Measurements for Impurities and Core Attenuation

In the relation

$$W \cdot \bar{s}_m = \frac{\frac{P}{M}}{\frac{I}{m}},$$

$\frac{I}{m}$ refers to the cavity chamber's response in amperes per gram of air in the cavity while $\frac{P}{M}$ refers to the calorimeter's response in watts per gram of carbon in the core. For this equation to hold accurately, corrections to the calorimetric results are required to allow for the radiation absorption of atoms other than carbon in the cores and for the effect of gamma-ray attenuation in the cores. No correction is needed for attentuation in the calorimeter shells as they were equal in thickness to the chamber wall, and the additional attenuation in the shell heater windings was negligible.

The effect of impurities is small and results in only a slight increase in gamma-ray heating relative to pure carbon. We calculate the excess, using the data of tables 1 and 2 and the mass energy transfer coefficients of Berger [14] to be 0.028 percent and 0.041 percent for the solid and hollow cores respectively.

In evaluating the core attenuation we have made use of data obtained by Loftus and Weaver [15] in this laboratory that show the variation with wall thickness of the response of a cavity ionization chamber. Three spherical chambers made of the same graphite as that used for the calorimeters were exposed in turn at the same distance from a cobalt-60 source similar in spectrum to the NBS water-shielded source. The resulting ionization current per gram of air within the cavity was determined for each chamber. The data of table 7 are the result of a series of such comparisons, all at source-chamber distances greater than 1 m.

TABLE 7. *Attenuation in graphite*

Chamber	Diameter of cavity	Thickness of wall	Current per gram of air relative to chamber 2
	cm	*mm*	
1	1.588	2.41	1.0065
2	1.270	4.00	1.0000
3	0.953	5.585	0.9900

These data indicate a fractional decrease in chamber response of 0.0051 per mm of wall thickness. Although the average wall thickness for each spherical chamber is larger than the radial thickness shown in table 7, the differences of these averages were found not to be significantly larger than the radial difference. The linear attenuation is therefore correctly given as 0.0051 per mm.

The length within the cores to be used for calculating the attenuation was obtained from a theorem of geometry due to Tomkeieff [16] that the average length $\bar{L}$ of the intercept in a spherical body is

$$\bar{L} = 4\frac{V}{S} \text{ where}$$

V = volume of sphere and

S = surface area of sphere.

If the body contains voids and V is taken to be the volume of the sphere less the volume of the voids, then the expression gives the average length of intercept not in a void. We find average gamma-ray paths in graphite from this theorem of 0.667 cm and 0.438 cm for the solid and hollow cores, respectively.

With no appreciable error of approximation the quotient of the average intensity of the radiation

within the cores by the intensity outside can be taken to be

$$1-0.0051\times\frac{6.67}{2}=0.9830 \text{ for the solid core and}$$

$$1-0.0051\times\frac{4.38}{2}=0.9888 \text{ for the hollow core.}$$

The absorbed gamma-ray power in watts per gram of pure carbon in the absence of core attenuation is therefore found to be by the two calorimeter determinations:

$$\text{Solid core: } 0.5140\times\frac{1}{1.00028}\times\frac{1}{0.9830}\times 10^{-3}$$
$$=0.5227\times 10^{-3} \text{ watts per gram.}$$

$$\text{Hollow core: } 0.5180\times\frac{1}{1.00041}\times\frac{1}{0.9888}\times 10^{-3}$$
$$=0.5237\times 10^{-3} \text{ watts per gram.}$$

Average: 0.5232×10^{-3} watts per gram.

5.2. Value of $\frac{P}{M}\div\frac{I}{m}$

The average values of $\frac{P}{M}$ and $\frac{I}{m}$ determined in this work give for their quotient

$$Q=\frac{\frac{P}{M}}{\frac{I}{m}}=\frac{0.5232\times 10^{-3}}{1.551_4\times 10^{-5}}=33.72 \text{ eV}$$

in carbon per ion pair in air.

5.3. Accuracy of Result

In estimating the uncertainty in the quotient $\frac{\frac{P}{M}}{\frac{I}{m}}$, we have considered the effect of uncertainties in the determinations of mass, ion chamber current, electrical calibration power, the attenuation correction that was applied to the calorimetry, the field strength extrapolation of the ion chamber current and in the extrapolated values of the electrical calibration and gamma-ray rates.

The measurements of voltage in this experiment are subject to a systematic error of ± 0.02 percent and a random reading error (standard error) of 0.01 percent which have been combined to give an overall uncertainty of 0.05 percent (three times 0.01 percent plus 0.02 percent).

The error in the ionization current measurements caused by an inability to null precisely is estimated to be no more than 0.04 percent.

The resistance value used in the ionization current measurements was considered to be accurate to within 0.01 percent. The values of R_1 and R_2 (fig. 2), used in the power calibration each have an uncertainty of not more than 0.05 percent.

An overall uncertainty of 0.13 percent has been assumed for temperature measurements, based on an estimated systematic error of 0.07 percent and a standard error of 0.02 percent, due to reading the instrument. No significant error is introduced by the method of measurement outlined above.

Pressure measurements are believed to be accurate to one part in 10,000 and are subject to reading errors of no more than 0.02 percent. These have been combined to give an overall uncertainty of 0.07 percent.

The uncertainty in the collection efficiency is estimated to be 0.06 percent, based on three times a standard error of 0.02 percent.

It has been estimated that the core attenuation correction introduces a systematic error of not more than 0.05 percent.

The mass of the calorimeter cores was believed to be known to two parts in 10,000.

The uncertainty in the collecting volume of the cavity chamber has been estimated to be no more than three times the standard error of the mean value of the cavity chamber volume, from table 3, since the error contributed by the collecting electrode volume measurement is negligible. Thus, an overall uncertainty of 0.36 percent has been assigned to the collecting volume.

Measurements before and after each of the two series of ionization measurements indicated that the chamber was off axis by only a small fraction of a millimeter. We estimate that this introduced no significant error in the ionization measurements.

The errors produced by the extrapolation process were computed to be no more than 0.10 percent and 0.04 percent for the gamma-ray heating and electrical calibration rates, respectively.

Tables 8 and 9 show the resulting uncertainties in $\frac{P}{M}$ and $\frac{I}{m}$, respectively, due to the different variables. The combined uncertainty in each ratio is the square root of the sum of squares of the individual uncertainties listed. The uncertainty in the value of $\frac{P}{M}\div\frac{I}{m}$ has been computed to be $(0.17+0.40)^{1/2}=0.43$ percent.

TABLE 8. *Uncertainty in* $\frac{P}{M}$

Variable—total uncertainty		Resulting uncertainty in $\frac{P}{M}$
		Percent
Mass of core:	0.02 percent	0.02
Power: Voltage measurement, V_2, fig. 2:	0.05 percent	.10
Resistance measurement, R_1, fig. 2:	0.05 percent	.05
Resistance measurement, R_2, fig. 2:	0.05 percent	.05
Core attenuation factor:	0.05 percent	.05
Electrical calibration rate extrapolation:	0.04 percent	.04
Gamma-ray rate extrapolation:	0.10 percent	.10
Square root of sum of squares		0.17

TABLE 9. *Uncertainty in* $\frac{I}{m}$

Variable—total uncertainty		Resulting uncertainty in $\frac{I}{m}$
		Percent
Mass of air: Volume:	0.36 percent	0.36
Pressure:	0.07 percent	.07
Temperature:	0.13 percent	.13
Current: Resistance:	0.01 percent	.01
Voltage measurement:	0.05 percent	.05
Null determination:	0.04 percent	.04
Collection efficiency:	0.06 percent	.06
Square root of sum of squares		0.40

5.4. Comparison With Other Measurements

The previous measurements of this quotient that were mentioned in the introduction are shown in comparison to the present result in table 10. These values should be directly comparable except for the slight differences in effective stopping power, $\bar{s}_m$, that may arise from the spectral dissimilarities of the different cobalt sources used. The values of $\bar{s}_m$ listed in table 10 are those given by the authors as applicable to their sources. The value for the NBS source was computed from the expression:

$$\int \mu(E)i(E)dE \div \int \frac{1}{\bar{s}_m(E)} \mu(E)i(E)dE$$

where $i(E)$ is the distribution in energy of photon intensity given in table 1, $\mu(E)$ is the mass energy transfer coefficient of carbon given by Berger [14] and $\bar{s}_m(E)$ is interpolated from the mean mass stopping power ratios for graphite relative to air given in table IA7 of NBS Handbook 85 [1]. While the methods used for obtaining $\bar{s}_m$ are not entirely consistent with one another, the resulting discrepancies are evidently small and probably negligible in comparison to the experimental uncertainties.

The value of Q included in table 10 from the earlier NBS measurements [6] differs from the other entries in that the value of ionization per unit mass of air was derived from an exposure rate measurement of the source with a calibrated chamber. The original data have been recomputed to remove a correction previously made for humidity and to change the attenuation correction so as to conform to that of the present experiment using the data of Loftus and Weaver. The uncertainty shown is largely that assigned to the NBS exposure standard in 1958.

The present measurements give the value of Q and hence the value of the product $W \cdot \bar{s}_m$ with an uncertainty of about 0.43 percent. Since the uncertainty in each of the factors is about one-half percent, the effect of the present determination is to reduce the product's uncertainty by about a factor of two. Our estimates of error for the presently reported experiment are two-thirds and one-third those of Bewley and of Reid and Johns respectively.

Table 10 includes the quotient of Q by $\bar{s}_m$ for each of the experiments. These should be equal, provided the values of $\bar{s}_m$ have been selected in a consistent way. The quotients show a reasonable degree of consistency, except for the early measurement of Bernier et al. If the data reduction computations of measurements 3 and 4 were to be altered to eliminate the humidity correction that was included, the quotients of Q by $\bar{s}_m$ would be increased, although probably by no more than 0.1 percent.

The consistency of the values of $Q \div \bar{s}_m$ does not, however, imply a corresponding degree of accuracy of W, since each quotient carries with it the uncertainty in $\bar{s}_m$. The uncertainty in $\bar{s}_m$ does not appear to be easily reduced by direct experiment or computation.

A more accurate experimental determination of W, on the other hand, does appear to be possible, and would, if available, also provide a more accurate value for $\bar{s}_m$.

TABLE 10. *Comparison of results*

Measurement number	Authors	$Q = \frac{P}{M} \div \frac{I}{m}$ [a]	$\bar{s}_m$ [b]	$W = Q \div \bar{s}_m$ [c]
1	Bernier et al. [4]	33.07 ± 0.21	1.005	32.91 ± 0.21
2	Hart et al. [6]	33.41 ± 0.7	1.004	33.28 ± 0.7
3	Reid and Johns [5]	34.15 ± 0.31	1.005	33.98 ± 0.31
4	Bewley [3]	34.11 ± 0.21	1.004	33.97 ± 0.21
5	Present	33.72 ± 0.14	1.004	33.59 ± 0.14

[a] Electron volts in carbon per ion pair in air.
[b] Effective mass stopping power of carbon relative to air.
[c] Electron volts in air per ion pair in air. Uncertainty does not include uncertainty in $\bar{s}_m$.

The authors are indebted to Harold O. Wyckoff for his continued interest in and many valuable discussions concerning this measurement.

6. References

[1] NBS Handbook 85, Physical Aspects of Irradiation (1964).
[2] L. H. Gray, Proc. Roy. Soc. (London), **A156,** 578 (1936).
[3] D. K. Bewley, Brit. J. Radiol. **36,** 865–878 (1963).
[4] J. P. Bernier, L. D. Skarsgard, D. V. Cormack, and H. E. Johns, Radiation Res. **5,** 613–633 (1956).
[5] W. B. Reid and H. E. Johns, Radiation Res. **14,** 1–16 (1961).
[6] E. J. Hart, H. W. Koch, B. Petree, J. H. Schulman, S. I. Taimuty, and H. O. Wyckoff, Proceedings of the second U.N. conference on the peaceful uses of atomic energy, Vol. **21,** 189–193 (1958), Geneva.
[7] B. Petree and J. C. Humphreys, Radiology **84,** 129 (Jan. 1965).
[8] V. H. Ritz and F. H. Attix, Radiation Res. **16,** 401–415 (1962).
[9] B. Petree and G. Ward, NBS Tech. Note 163 (1962).
[10] D. D. Enagonio, E. G. Pearson, and C. P. Saylor, Temperature, its measurement and control in science and industry, Vol. **3,** Part 1, 219–230 (Reinhold Publishing Corporation, New York, 1962).
[11] T. P. Loftus, B. Petree, and J. T. Weaver, Radiology **86,** 149 (1966).
[12] G. Mie, Ann. Phys. Lpz. **13,** 857 (1904).
[13] T. E. Burlin and S. R. Husein, J. Sci. Instr. **42,** 800 (1965).
[14] R. T. Berger, Radiation Res. **15,** 1 (1961).
[15] T. P. Loftus and J. T. Weaver (private communication).
[16] S. I. Tomkeieff, Nature **155,** 24 (1945).

(Paper 71C1–440)

JOURNAL OF RESEARCH of the National Bureau of Standards—C. Engineering and Instrumentation
Vol. 71C, No. 1, January–March 1967

Germanium Resistance Thermometry in the Range 2.1 to 5.0 °K

M. H. Edlow [1] and H. H. Plumb

Institute for Basic Standards, National Bureau of Standards, Washington, D.C. 20234

(September 9, 1966)

The resistances of three encapsulated, hermetically sealed, arsenic-doped germanium resistors from a commerical source have been measured at every 0.1 °K from 2.1 to 5.0 °K in highly stabilized liquid helium baths; values of temperature were derived from vapor pressure measurements associated with the liquid bath.

Ten similar germanium resistors of common origin have been calibrated from 2.1 to 5.0 °K in a calibration comparator apparatus that is similar to a calorimeter in design. Calibrations were performed against a resistor that had been previously referenced to temperature through a helium-4 vapor pressure calibration.

Next, three of the resistors that were calibrated in the comparator apparatus were recalibrated in a liquid helium bath (at 2.2, 3.0, and 4.2 °K) and results from the two methods agree within ± 1 millidegree. The resistance-temperature data from both methods have been fitted to the polynomial equation $\log_{10} R = \sum_{n=0}^{m} A_n \cdot (\log_{10} T)^n$ and the results of a computer program, which evaluates the coefficients, are presented.

1. Introduction

We have a group of impurity-doped germanium resistors that possess desirable thermometric properties at low temperatures—negative coefficient of temperature, good sensitivity and excellent reproducibility under thermal cycling [1].[2] This paper describes the calibration (in the range 2.1 to 5.0 °K) of the above-mentioned resistor group.

Several resistors have been calibrated directly against liquid helium-4 vapor pressures thus giving reference to temperatures from the "1958 He^4 Scale of Temperatures" [2]. Since this method of calibration is costly in both time and refrigerant materials, a different procedure was utilized for extending the calibration over a greater number of resistors. An apparatus was constructed for comparison calibrations between "unknowns" and resistors that had been previously calibrated against helium-4 vapor pressures.

2. Calibration in a Liquid Helium Bath

2.1. Liquid Helium Bath

The apparatus, used for calibrating germanium resistors in a highly stabilized liquid helium bath, has been described in an earlier paper [1]. While the previous report was based upon calibrations in the vicinity of 4.2 °K only, no modification of the apparatus was necessary for expanding the calibration range to include 2.1 to 5.0 °K.

The bath consisted of about 8 liters of liquid helium which filled the spherical liquid helium storage Dewar (25 liters) to a height of 14 cm. This provided a liquid helium surface level that did not extend above the thermally insulating vacuum jacket of the vapor pressure bulb. The storage Dewar was then connected to a vapor pressure regulator [3] and the surface vapor pressure monitored by a mercury manometer. Small amounts of helium gas from a 1-liter filling can were bled into the jacketed vapor pressure thermometer. After the helium gas pressure in the thermometer equaled the controlled bath surface pressure, ⅓ of an atmosphere of helium gas was slowly metered into the bulb to condense approximately 0.5 cm^3 of liquid. Since the thermometer bulb volume was 2 cm^3, the fluid level was well below the top of the bulb and the remaining volume was sufficiently large to contain some additional condensate-condensation of gas from the vapor pressure thermometer tubing occurred when the vapor pressure of the helium bath was intentionally decreased during the course of a calibration.

The calibration from 2.1 to 5.0 °K was procedurally divided into three stages. Obvious checks were made to ascertain that there was appropriate electrical continuity of resistor leads and no undesired grounding in the resistance measuring circuit before the resistors were lowered into helium bath. Then the Dewar bath was cooled to appropriate temperatures

[1] M. H. Edlow is presently associated with the United States Patent Office.
[2] Figures in brackets indicate the literature references at the end of this paper.

by pumping through the vapor pressure regulating manostat and calibrations were performed at every 0.1 °K in the range 4.2 to 2.6 °K. Next, the Dewar bath was warmed to the helium boiling point (by bleeding helium gas into the Dewar) and a second liquid helium transfer made. The second transfer was necessary since a height of only 3.2 cm of liquid helium remained in the Dewar after the calibration at 2.6 °K was finished. The bath was then cooled directly to 2.5 °K and subsequent calibrations performed at the five lower temperature points −2.5, 2.4, 2.3, 2.2, and 2.1 °K. Thirdly, the Dewar bath was warmed to 4.2 °K, a necessary third liquid helium transfer made and the calibration performed in the range 4.2 to 5.0 °K. (Vapor pressures that exceed atmospheric pressure were obtained by closing off the manostat and allowing the Dewar vapor pressure to build up to a desired value at which time it was again manostatically controlled. The normal evaporation rate within the Dewar provided the gas for the increased pressure.)

2.2. Vapor Pressure Thermometry

The vapor pressure measuring techniques, used in these measurements, were consonant with procedures that we have previously reported [4]. Since a temperature gradient exists at the surface of the "constant temperature" liquid bath, the vapor pressure thermometer tubing must be thermally insulated from the colder surface to avoid spurious effects caused by "cold spots" [4,5]. Consequently, the thermometer tubing was surrounded by a vacuum jacket—the tubing length that otherwise would be in contact with the liquid surface—thus insuring that the vapor pressure thermometer indicated a vapor pressure that was associated with the bulk liquid. Vapor pressure measurements of both the helium surface and the thermometer bulb were routinely performed and recorded. In a previous paper [4], we have listed the observed differences in these two measurements for tenth-degree intervals from 2.1 to 4.2 °K. Table 1 lists typical comparisons derived from the calibration data that are the basis for this paper. The differences between the two vapor pressures, P_J and P_S, are not unique since the pressure and temperature gradients, at the liquid helium surface, appear to be dependent upon at least two conditions—the geometry of the contained liquid helium and the Dewar evaporation rate. Nevertheless the qualitative change in magnitude of the surface temperature gradient (ΔT) as a function of the helium bath temperature is supported by the results of many experimental "runs" in our laboratory. Additionally, as we have previously reported [4], calibrations of germanium resistors across the helium−λ point have been "smooth" when temperatures in the helium-I region were derived from pressures measured in conjunction with the jacketed vapor pressure thermometer. We have been unable to obtain a "smooth" calibration across the λ-point when temperatures are derived from surface vapor pressure measurements; as might be suspected, temperatures derived from either method are satisfactory in the temperature region of helium-II provided the effects of helium film creep do not enter as a variable.

In the range 4.2 to 5.0 °K, the vapor pressure bulb required periodic additions of helium gas since, as the vapor pressure was increased, some of the previously condensed liquid helium must be evaporated to supply the required helium gas in the vapor pressure thermometer tubing. The inverse operation was necessary as temperatures were reduced below 4.2 °K i.e., liquid helium was occasionally removed from the bulb to avoid an overfilling of the bulb.

TABLE 1. *Vapor pressure measurements in a "constant" temperature liquid helium-4 bath*

Temperature	P_J[a] − P_S[b]	ΔT[c]	Temperature	P_J[a] − P_S[b]	ΔT[c]
°K	*mm* Hg	*mdeg*	°K	*mm* Hg	*mdeg*
5.0	0.43	0.4	3.5	0.84	2.0
4.9	.38	.4	3.4	.76	1.9
4.8	.66	.7	3.3	.71	2.0
4.7	.71	.7	3.2	.66	2.0
4.6	.86	1.0	3.1	.61	2.0
4.5	.97	1.1	3.0	.58	2.1
4.4	.99	1.2	2.9	.58	2.4
4.3	1.02	1.4	2.8	.56	2.6
4.2	0.91	1.3	2.7	.48	2.5
4.1	1.07	1.6	2.6	.48	2.8
4.0	0.97	1.6	2.5	.43	2.8
3.9	.91	1.6	2.4	.38	2.9
3.8	.90	1.7	2.3	.38	3.3
3.7	.90	1.8	2.2	.33	3.4
3.6	.81	1.8	2.1	.00	0.0

[a] P_J is the helium vapor pressure of the jacketed thermometer.
[b] P_S is the helium vapor pressure of the bath surface.
[c] ΔT (the temperature equivalent of the pressure difference, $P_J - P_S$) is equal to $\frac{(P_J - P_S)}{\frac{dP}{dT}}$. $\frac{dP}{dT}$ is obtained from the "1958 He^4 Scale of Temperatures" [2].

In the range 4.8 to 5.0 °K there were a few instances when the helium gas oscillated in the jacketed vapor pressure tube. These oscillations [6] were indicated by: (1) Thermometer vapor pressures greatly exceeded surface vapor pressures of the bath after surface pressure control had been established for several hours; (2) the evaporation rate of the helium bath, as measured with a flow meter, was greatly increased (by as much as a factor of three) but returned to its normal value when the bulb was evacuated; and (3) large oscillations were observed in the mercury manometer. Reliable measurements were obtained in these instances by altering the liquid bath temperature to a value where oscillations were not encountered.

Resistance determinations, at each stabilized temperature, were measured potentiometrically; the electrical power applied to a resistor generally did not exceed 0.02 μW, but at temperatures above 4.6 °K, it was possible to apply 0.1 μW without causing appreciable joule heating in the resistors.

2.3. Discussion

The calibration at each temperature in the range 2.1 to 4.2 °K required approximately 3 hr−½ to 1 hr for cooling the bath to the desired surface vapor pressure, 2 hrs for the bath to stabilize and ½ hr for performing electrical measurements. In one range above the

boiling point, 4.7 to 5.0 °K, it required about 24 hrs to increase the bath temperature by 0.1 °K. Therefore, it was not unusual to expend three weeks in performing a calibration at every 0.1 °K from 2.1 to 5.0 °K. The fact that at least three liquid helium transfers were necessary to cover the range made this calibration expensive as well as time consuming. For these reasons, an isothermal comparator was constructed for calibrating a large number of resistors more efficiently.

3. Calibration in an Isothermal Comparator

3.1. Comparator

The comparator design and construction is shown in figure 1. The copper top A of the outside can B is 6.04 cm in diameter and has an internal extended sleeve A′ (1.90 cm O.D., 2.22 cm long, and 1.27 cm wall thickness). The outside can B is mainly brass and has the dimensions of 6.67 cm diam, 21 cm long, and 0.159 cm wall thickness; the upper 1.27 cm of the can is a piece that was machined to receive the cylindrical tongue of top A. Wood's metal is used to solder the copper top to the brass can. The bottom of the brass can C is a brass disk that has been silver soldered to the outside cylinder. During a calibration, the can B is contained in a liquid bath whose liquid level is well above the top A. The thermal anchor post T, 0.477 cm copper rod, is screwed into A. Three Teflon rods, each of 0.32 cm diam and 3.2 cm long, are equally spaced on the end of cylinder A′ and screwed into the wall thickness. A 0.64 cm perforated stainless steel tube E was silver soldered to the copper top A; its opposite end was soft soldered to the top of the 2.5 cm solid copper cylinder J. Twelve 0.36 cm diam holes N were drilled at an angle of 45 degrees to the axis of J and to a depth of 1.12 cm, which is sufficiently deep to contain the length of a germanium resistor encapsulation. The inner copper can K, 6.4 cm outside diameter, 9.5 cm long, screws onto the threaded surface of the shoulder M. K serves as a radiation shield for the portion of the cylinder that contains the resistors. Several 0.16 cm holes O were drilled through K to enhance evacuation of the volume within K. F and F′ (0.64 cm, thin wall, stainless steel tubings), were soft soldered through A and serve respectively, as a helium gas filling or evacuation line and conduit for lead wires to the resistors and heater coil. A total of 14 leads (#38 A. W. G. formvar coated, double nylon insulated, copper wire) are used as connecting wires—4 pairs as potential leads to the germanium resistors that are involved in a calibration, 1 pair for current leads to the series connected resistors and 1 pair each for the sensor and heater coil. For the heater coil, #36 A.W.G. manganin wire was noninductively wound on the bobbin H to provide a total resistance of 38,000 Ω at room temperature.

The seven pairs of connecting wires were conducted down from the Dewar cap through F′ (see fig. 2) and wound around the thermal anchor T—prior to wrapping

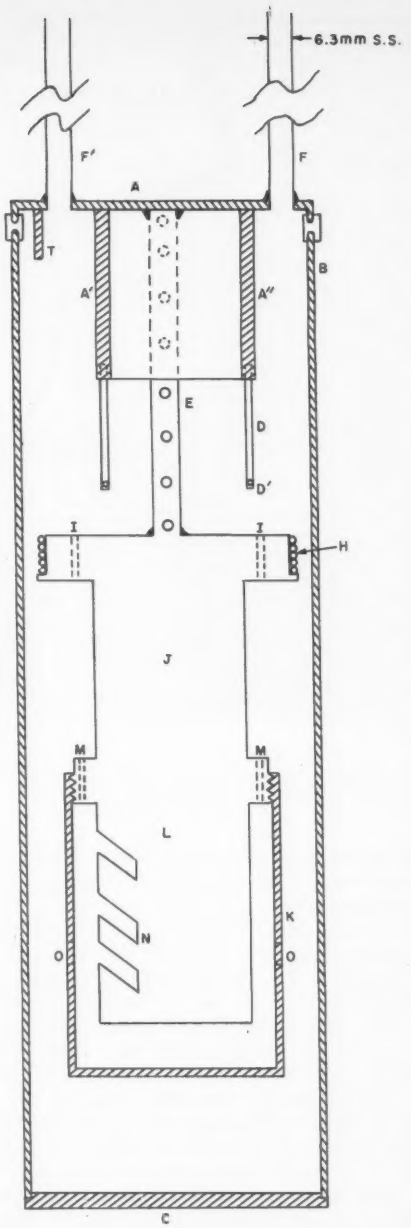

FIGURE 1. *Design of comparator—the low temperature component of apparatus employed in calibrating germanium thermometers from 2.1° to 5.0 °K.*

around *T*, a small loop was made to allow for thermal contraction of the leads within the tube F′. Next, about 60 cm of the leads were spirally wound about the thermal anchor A′ and afterwards, coatings of G.E. varnish #7031 were applied to the wires and surfaces of T and A′ to enhance the thermal contact between

237-679 O-67—3

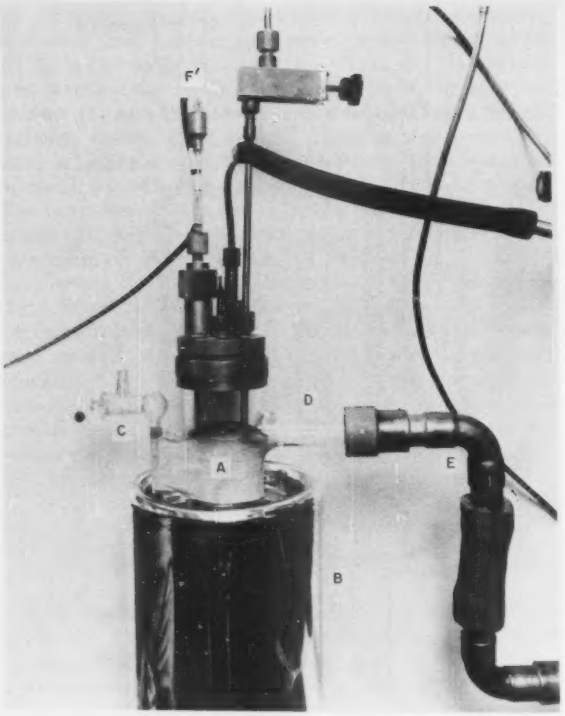

FIGURE 2. *A view of the upper portion of the cryostat that contains the calibration comparator.*

the lead wires and thermal anchors. This treatment will greatly reduce the heat leaks along the wires from room temperatures to the resistors. Additional lengths of wire were then spiralled around the three Teflon posts D and strung through holes D′ drilled near the end of the Teflon rods. One pair of leads was separated from the group and connected to the heater coil. The remaining 6 pairs were conducted through I, 0.159 cm holes that had been previously lined with Teflon, and thence spiralled around J where #7031 varnish was also applied. Next, the wires were then led through M, 0.159 cm holes also lined with Teflon, wrapped once around L and thence soldered to the germanium resistor leads with Wood's metal. The soldered connections are enclosed by spun glass spaghetti to avoid electrical shorting or grounding of the leads.

In use, the vacuum can B and its top A are exposed to a bath temperature that is less than 2 °K, while the cylindrical block J is maintained at calibration temperatures that exceed 2 °K. Thus, without proper precautions, large undesired heat-flows could occur and cause: (i) a temperature instability of the block J with resultant gradients; (ii) abnormally large evaporation rates of the surrounding liquid helium bath; and (iii) a lack of thermal equilibrium between the resistors that are to be calibrated. The comparator has been designed to reduce and control the flow of heat toward and away from J. (1). Radiant transfer from J or K to the outer can B is small. (2). The continuous evacuation of B minimizes heat transfer through gas conduction and convection. (3) Heat conduction through the leads and mechanically supporting members has been reduced.

There are several other component systems that are used in conjunction with the comparator. Temperature control of L or J (fig. 1) is effected by an automatic electronic system. A germanium sensor, mounted in a cavity N of L (fig. 1) serves as one leg of a Wheatstone bridge. Any unbalance of the bridge is amplified and fed into a controller which in turn regulates current flow through the heater H (fig. 1).

Shown in figure 2, is the upper portion of the cryostat that consists of a glass Dewar A (7.0 cm I.D. and 100 cm long), which contains the liquid helium in which the comparator is immersed, and an external Dewar that contains liquid nitrogen for thermally shielding the liquid helium Dewar. The figure shows a vacuum tight Dewar cap that accommodates the two tubes, which lead to the comparator (tubes F and F′ of fig. 1), and permits filling of the Dewar with liquid helium. Also shown, is the Dewar's horizontal sidearm D that connects to a vacuum pumping line E—by "pumping" on the vapor pressure through this line, helium bath temperatures of less than 2 °K are achieved. The vertical tubing, which includes the vacuum valve, leads from an external "high vacuum" pumping system to the insulating vacuum space of the comparator; electrical lead ingress to the comparator is afforded by the tubing on the left. All of the apparatus, with the exception of the helium vapor pressure pumping system, is located within a shielded room that isolates the equipment from local rf interference [7].

3.2. Comparator Operating Procedure

The resistors that were involved in a calibration were mounted in the copper block J (fig. 1) in a medium of Apiezon stopcock grease to enhance thermal contact. The outer can B was soldered in place with Wood's metal and the 14 electrical leads then checked for electrical continuity. After appropriate leak detection the comparator was mounted in the cryostat, a small amount of helium gas was bled into the vacuum space (within can B) and the apparatus precooled to liquid nitrogen temperatures. Next, liquid helium was transferred into the inner Dewar, resistor lead continuity checks performed again, and then the liquid helium bath cooled to 1.5 °K. After the helium exchange gas was sufficiently evacuated, the resistance of the Wheatstone bridge was set to correspond to the 2.1 °K resistance value (determined in an initial calibration) of the temperature controlling sensor. The three control dials—proportional band, rate time and reset—of the servocontrol unit were set to obtain adequate temperature control of the comparator. Proper settings of the three controls result in a temperature control as fine as 1×10^{-4} °K at 2.1 °K. This has been evidenced by repetitive resistance deter-

minations for resistor #1 over a period of 30 min. Generally, once a good setting has been obtained at the lowest calibration temperature, the dials need not be changed for the remainder of the calibration.

In establishing any given calibration control point, a value of resistance was dialed on the Wheatstone bridge and sufficient time was allowed for the recorder pen of the temperature controlling unit to reach the control or zero position. (Generally about 10 min was required to attain temperature stability after an increase of 0.1 °K in the temperature of the comparator.) Initial measurements on resistor #1 often indicated a deviation of approximately several millidegrees from a desired calibration temperature. In this event appropriate corrections were made on the Wheatstone bridge settings, five additional minutes allowed for equilibrium and measurements were again made across #1. This process was repeated until the resistance of #1 indicated a value that was within ±0.5 mdeg of the desired calibration temperature.

4. Germanium Resistance Thermometers

For all of the germanium resistors, whose calibrations are being reported in this paper, we have a thermal cycling history. That is, the resistors have been thermally cycled from room temperature to 4.2 °K and systematic calibrations of resistance and temperature performed at 4.2 °K. The methods of cycling and calibration have been previously described [1], and the reproducibilities of particular resistors were stated. The previous resistor identification symbols will apply to precisely the same resistors in this report. All of the resistors are four lead models and are hermetically encapsulated in platinum containers filled with helium gas. However, the calibrator design and method of mounting resistors in the comparator are such that a leaking encapsulation will probably not affect the general validity of a calibration. Most of the resistors are similar in that their values of resistance are comparable at 4.2 °K—this probably means that their "dopings" are similar and consequently, that similar equations will represent the resistance temperature calibration data.

5. Experimental Results

5.1. From the Stabilized Helium Bath

Resistors 1, 2, and 3 (reproducible to approximately 1 mdeg under thermal cycling [1]) have been calibrated simultaneously in the "constant temperature" helium bath from 2.1 to 5.0 °K at intervals of 0.1 °K; the results are listed in table 2. A log-log plot of resistance versus temperature for #1, #2, and #3, shown in figure 3, suggests the possibility of representing the calibration data by a polynomial of the form

$$\log_{10} R = \sum_{n=0}^{m} A_n (\log_{10} T)^n.$$

TABLE 2. *Calibrated resistances obtained in the highly stabilized liquid helium baths*

Resistor #1	#2	#3	Temperature [a]
Ω	Ω	Ω	°K
13281.	12435.	13739.	2.0993
11749.	10982.	12064.	2.2013
10528.	9821.0	10740.	2.2995
9491.6	8839.0	9611.0	2.3984
8588.0	7979.0	8632.0	2.5003
7841.0	7271.7	7832.3	2.5994
7106.4	6572.9	7042.0	2.7130
6611.8	6108.0	6519.0	2.8005
6119.1	5639.4	6000.0	2.8996
5681.2	5227.1	5537.5	2.9986
5287.2	4855.8	5128.3	3.0997
4938.8	4527.8	4766.3	3.1997
4625.8	4232.8	4443.0	3.2997
4345.1	3968.7	4155.1	3.3996
4090.2	3729.9	3894.6	3.4999
3859.6	3513.4	3660.6	3.5996
3650.4	3317.0	3448.2	3.6996
3457.4	3136.9	3253.8	3.7999
3279.7	2970.6	3075.3	3.9007
3118.8	2820.7	2914.7	4.0000
2972.0	2683.4	2768.6	4.0981
2829.8	2551.8	2627.8	4.2000
2699.2	2430.2	2498.7	4.3014
2579.6	2318.9	2381.1	4.4011
2468.6	2216.2	2272.1	4.5002
2363.2	2119.0	2169.7	4.6009
2266.3	2029.0	2075.1	4.6998
2173.4	1942.8	1985.4	4.7999
2086.6	1862.7	1901.4	4.9004
2005.4	1787.9	1823.1	5.0005

[a] Temperatures are derived from the "1958 He^4 Scale of Temperatures" [2] using values of vapor pressure that were obtained with a jacketed vapor pressure thermometer.

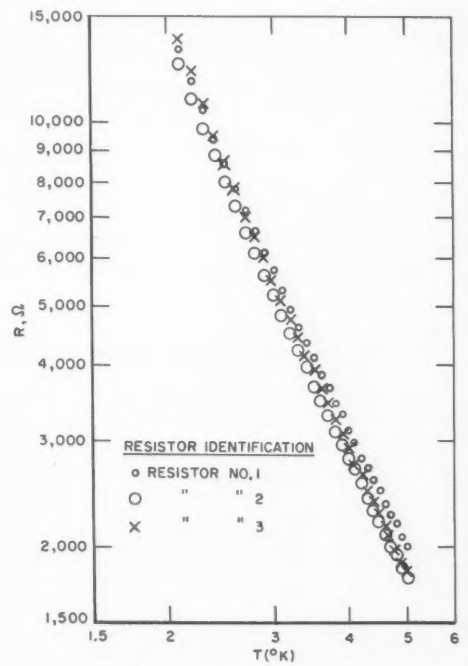

FIGURE 3. *A plot of the resistance-temperature calibration data for resistors 1, 2 and 3.*
Temperatures were derived from liquid helium-4 vapor pressures.

Consequently, the resistance temperature calibration data (obtained from the bath calibration) were programmed on a computer for a least squares fitting to the above polynomial. The program was "cascaded" so that a succession of least squares fitting was performed for upper limits of m that extended consecutively from 3, . . ., 8. The results require discussion since there are at least two ways of considering the representation of the calibration data.

(a) Except for the effect of spurious errors, the limiting accuracy of a calibration could possibly approach ± 0.001 °K. This would probably occur at the lowest temperatures and would be mainly associated with the accuracy of our helium vapor pressure measurements.

(b) If, however, one feels that the 0.001 °K assessment of error is high or might be smoothed out in the polynomial fitting, it is not obvious as to how far one should proceed with the polynomial fitting.

Because of these two considerations we felt compelled to present, in this paper, results which would be in accordance with either (a) or (b) of the preceding paragraph. In the computer analyses for the three resistors, the polynomial $\log_{10} R = \sum_{n=0}^{3} A_n (\log_{10} T)^n$ could possibly represent the data within the limits of condition (a). However there exists an obvious systematic deviation between the fitted function (R_{calc}, T) and the input calibration data (R_{data}, T_{data}). This is apparent in figure 4 where points of inflection occur near 2.8, 3.6, and 4.4 °K. While the general conclusion from figure 4 might be the indication that the input data has been adequately fitted within the limits of experimental errors, another possibility is suggested—the data is more consistent than ± 0.001 °K and the function that would represent the data is not adequately approximated by $\log_{10} R = \sum_{n=0}^{3} A_n (\log_{10} T)^n$. Consequently we have continued the analysis to higher order polynomials. Table 3 contains the evaluated polynomial coefficients for resistor #1; a double precision computer program prepared by the National Bureau of Standards Statistical Engineering Laboratory was used to overcome the roundoff error characteristic of fitting high order polynomials, and in this case the roundoff error was several orders of magnitude smaller than other experimental uncertainties.

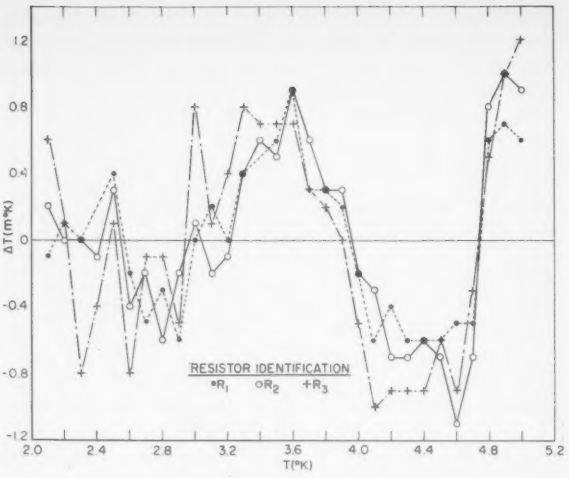

FIGURE 4. *Differences between the fitted functions, log* $R = \sum_{n=0}^{3} A_n (\log T)^n$ *and the calibration data for resistors 1, 2 and 3.*

(a) The residuals $\Delta T = (R_{Gen.} - R_{Data})dT/dR$ is the temperature equivalent of $(R_{Gen} - R_{Data})$ which is the difference between the fitted polynomial function evaluated at T_{Data} (R_{Gen}) and the resistance value of the calibration (R_{Data}, T_{Data}). dR/dT is the temperature coefficient of resistance.

(b) The residual plots apply to the three resistors [#1 (·), #2 (0) and #3 (+)]; the calibration data for each resistor have been individually fitted to third order polynomials.

As higher order polynomials are used, the systematic differences—between the fitted polynomial and the input data—gradually diminish up to the 7th order where apparently random residuals result. Figure 5 is the plot of these residuals resulting from fitting the seventh order polynomial for resistors 1, 2, and 3. For $n = 7$ of table 3, it is apparent that the

TABLE 3. *Coefficients of the polynomial,* $\log_{10} R = \sum_{n=0}^{m} A_n (\log_{10} T)^n$, *fitted to the calibration data of Resistor #1*

Polynomial order	$m=3$		$m=4$		$m=5$		$m=6$		$m=7$		$m=8$	
Coefficient	Coef.	δC [a]	Coef.	δC [a]	Coef.	δC [a]	Coef.	δC [a]	Coef.	δC [a]	Coef.	δC [a]
A_0	5.202	(0.0023)	5.180	(0.0112)	5.380	(0.0396)	5.685	(0.198)	2.219	(0.735)	[1.86]	(2.63)
A_1	−4.249	(.0145)	−4.062	(.0922)	−6.160	(.411)	−9.995	(2.48)	40.873	(10.72)	[46.9]	(43.7)
A_2	3.304	(.0287)	2.732	(.279)	11.348	(1.68)	31.136	(12.74)	−284.78	(66.3)	[−329.]	(316)
A_3	−1.593	(.0185)	−.8355	(.369)	−18.206	(3.37)	−71.870	(34.41)	1004.6	(225)	[1186]	(1291)
A_4			−.3687	(.179)	16.846	(3.33)	[97.546] [b]	(51.61)	−2076.8	(454)	[−2538]	(3268)
A_5					−6.715	(1.30)	[−70.554]	(40.77)	2533.5	(542)	[3278]	(5248)
A_6							[20.767]	(13.26)	−1692.1	(356)	[−2435]	(5221)
A_7									477.6	(99.3)	[897]	(2943)
A_8											[−103]	(720)
Std. Dev.	1.12×10^{-4}		1.06×10^{-4}		7.4×10^{-5}		7.2×10^{-5}		5.1×10^{-5}		5.2×10^{-5}	

[a] δC is the standard error of a coefficient.
[b] The brackets indicate that the enclosed coefficient is poorly defined; that is, the ratio of the coefficient to its standard error is less than 2.

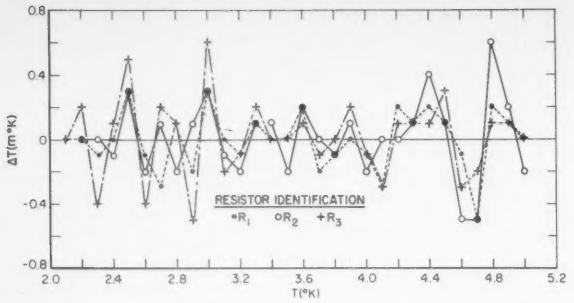

FIGURE 5. *Differences between the fitted functions, log* $R = \sum_{n=0}^{7} A_n$ *(log T)^n and the calibration data for resistors 1, 2 and 3.*

(a) See (a) of figure 4.
(b) The residual plots apply to the three resistors [#1 (.), #2 (0) and #3 (+)]; the calibration data for each resistor have been individually fitted to seventh order polynomials.

first coefficient is the least defined coefficient of the column. Since random residuals, exhibited in figure 5, were achieved by the seventh degree polynomial and the coefficients of the eighth degree are poorly determined, we did not attempt to extend the fitting to higher order polynomials. (It does seem, for resistor 1 in table 3, that odd order polynomials provide a better functional fit than even orders. This observation is generally applicable to other germanium resistor calibrations between 2 and 5 °K and will be discussed later in the paper.)

In comparing figures 4 and 5, one observes that not only has the systematic deviation of figure 4 been removed by progressing to the polynomial fitting portrayed in figure 5, but also, the values of standard deviation that are listed in the last row of table 3 have been reduced by a factor of two. Despite this, one should be cautious about inferring: either (a), the calibration data were valid to ±0.0005 °K; or (b), the polynomial fitting is completely satisfactory; or (c), conclusions concerning the He^4 vapor pressure scale against which calibrations were performed. These items will require further clarification.

Since resistor #1 was to serve as a basis for calibrating additional resistors, a decision had to be made regarding its calibration representation. Although it is somewhat arbitrary, we decided to use the 7th order polynomial because it might have the effect of smoothing out experimental errors in resistor #1's calibration. The seventh order coefficients (table 3) were used to generate R, $\frac{dR}{dT}$ and $\frac{d^2R}{dT^2}$ for resistor #1 at intervals of 0.0001 °K from 2.1 to 5.0 °K; this generated table is the basis for calibrating additional resistors against resistor #1. It is pertinent to state that both the generated $\frac{dR}{dT}$ and $\frac{d^2R}{dT^2}$ did not exhibit a sign change in the range of generation; that is, the fitted seventh order polynomial is a smooth function in the range of use.

In general the polynomial fittings of resistors #2 and #3 produce results that parallel the findings for resistor #1. This is indicated by the plots of residuals for resistors #2 and #3 in figures 4 and 5.

5.2. Comparison Calibrations With Reference to Resistor #1

Ten resistors have been calibrated in the isothermal comparator with reference to the calibrated resistor #1 and the data are listed in tables 4 to 8. In each of the indicated runs, three "unknowns" were calibrated against resistor #1 (the data for the third resistor is not included in table 4). As a control on the stability of the calibrations, resistor I was measured in each of the five calibration runs. Thus there appears in each table the measured resistances of resistors #1 and I and two unknowns (one unknown in table 4). Temperatures, which are assigned to the resistance values of resistor #1, are taken from the Resistance-Temperature generation that was derived from a seventh order polynomial fitting (sec. 5.1).

It is also readily noted that particular calibration temperatures, in the 5 separate runs, are generally realized within a few millidegrees. This was intentional and eliminates interpolation inaccuracies that

TABLE 4

Run 3

Calibration data for Resistor I and Resistor L

R_1	T[a]	R_1	R_L
Ω	°K	Ω	Ω
13241	2.1017	17117	15178
11754	2.2010	14905	13304
10584	2.2945	13192	11849
9515.4	2.3960	11652	10530
8604.7	2.4985	10365	9420.9
7842.2	2.5991	9303.5	8499.4
7107.7	2.7125	8295.7	7620.1
6610.6	2.8008	7624.3	7030.5
6119.9	2.8992	6969.6	6453.0
5681.7	2.9987	6392.7	5941.1
5285.5	3.1001	5877.7	5483.3
4940.6	3.1990	5433.0	5085.5
4625.3	3.2999	5033.2	4726.3
4343.9	3.4000	4680.2	4407.7
4090.7	3.4996	4365.1	4121.8
3859.0	3.6000	4081.3	3863.6
3457.2	3.7999	3595.4	3419.0
3279.3	3.9009	3383.8	3224.3
3118.6	4.0000	3194.4	3049.0
2972.2	4.0976	3023.1	2890.0
2830.4	4.1997	2859.0	2737.3
2698.7	4.3019	2707.5	2596.1
2579.8	4.4010	2572.0	2469.2
2467.7	4.5010	2445.6	2350.3
2362.5	4.6013	2327.3	2239.0
2266.2	4.6993	2220.2	2137.7
2173.3	4.8001	2117.5	2040.3
2086.7	4.9002	2021.9	1949.9
2005.5	5.0002	1933.6	1865.6

[a] T is the temperature associated with the adjacent value of resistance for R_1, which was previously calibrated against T_{58} [2].

TABLE 5

Run 5

Calibration data for Resistor H, Resistor M, and Resistor I

R_I	T[a]	R_H	R_M	R_I
Ω	°K	Ω	Ω	Ω
13246.0	2.1014	14596	13819	17121
11742.0	2.2018	12801	12165	14882
10579.0	2.2949	11425	10894	13182
9507.0	2.3968	10173	9725.7	11639
8609.8	2.4979	9130.1	8754.7	10371
7840.1	2.5994	8245.1	7924.5	9298.5
7107.0	2.7127	7402.4	7137.8	8292.8
6609.6	2.8010	6845.5	6607.1	7620.4
6121.2	2.8990	6293.9	6088.5	6969.8
5682.7	2.9985	5804.0	5623.7	6392.8
5287.8	3.0995	5366.1	5208.4	5879.1
4941.5	3.1988	4981.9	4843.3	5433.9
4626.7	3.2995	4636.0	4513.9	5034.3
4344.7	3.3997	4329.6	4219.9	4681.1
4091.9	3.4991	4056.7	3956.7	4367.1
3859.6	3.5998	3806.8	3716.1	4082.2
3650.4	3.6993	3584.0	3500.1	3828.0
3458.5	3.7992	3379.7	3302.4	3597.3
3280.0	3.9005	3190.9	3118.9	3384.7
3118.9	3.9998	3020.9	2954.1	3194.5
2973.4	4.0968	2869.1	2805.7	3024.8
2830.1	4.1999	2718.8	2659.8	2858.5
2699.1	4.3015	2582.8	2526.6	2707.9
2579.1	4.4015	2459.8	2406.0	2571.5
2468.3	4.5004	2345.7	2294.1	2446.7
2363.9	4.5999	2238.3	2188.3	2328.9
2266.7	4.6988	2139.6	2091.0	2221.1
2173.6	4.7997	2044.6	1897.4	2117.8
2086.4	4.9006	1956.5	1910.2	2022.0
2005.1	5.0007	1874.4	1829.3	1933.3

[a] T is the temperature associated with the adjacent value of resistance for R_I, which was previously calibrated against T_{58} [2].

TABLE 6

Run 6

Calibration data for Resistor C, Resistor G, and Resistor I

R_I	T[a]	R_C	R_G	R_I
Ω	°K	Ω	Ω	Ω
13244	2.1015	14995	14431	17120
11747	2.2015	13165	12649.5	14889
10580.5	2.2949	11754	11276.5	13185.5
9513.5	2.3962	10471	10031	11649
8611.0	2.4977	9395.1	8986.7	10372.3
7841.3	2.5993	8486.1	8105.1	9300.4
7105.7	2.7129	7623.0	7268.8	8291.2
6612.7	2.8004	7048.8	6713.2	7626.1
6121.6	2.8989	6481.7	6165.1	6971.2
5681.5	2.9988	5976.7	5676.4	6390.3
5287.1	3.0997	5527.7	5243.6	5879.7
4939.7	3.1993	5132.5	4862.5	5432.2
4625.7	3.2998	4777.7	4520.8	5033.1
4344.8	3.3997	4463.5	4217.5	4680.6
4090.9	3.4995	4180.6	3945.2	4366.8
3859.7	3.5997	3924.0	3699.0	4082.5
3650.0	3.6995	3692.5	3476.8	3827.9
3457.9	3.7995	3482.0	3275.9	3597.2
3280.6	3.9001	3287.6	3089.0	3385.6
3119.1	3.9997	3112.2	2921.2	3194.9
2972.1	4.0977	2953.4	2769.9	3023.3
2829.8	4.2001	2799.9	2623.6	2858.0

[a] T is the temperature associated with the adjacent value of resistance for R_I, which was previously calibrated against T_{58} [2].

TABLE 7

Run 7

Calibration data for Resistor F, Resistor J, and Resistor I

R_I	T[a]	R_F	R_J	R_I
Ω	°K	Ω	Ω	Ω
13238	2.1019	15290	15228	17092.5
11745	2.2016	13364	13293.5	14873.5
10579.5	2.2949	11880.5	11807.0	13173.5
9509.8	2.3965	10532.0	10455.4	11632.6
8608.0	2.4981	9409.7	9336.2	10355.8
7843.9	2.5989	8472.0	8398.6	9297.2
7108.4	2.7124	7578.0	7509.6	8286.5
6609.3	2.8010	6979.5	6912.6	7615.6
6119.5	2.8993	6395.9	6332.4	6960.7
5680.5	2.9990	5880.2	5820.4	6384.4
5287.2	3.0996	5422.9	5366.3	5875.4
4938.4	3.1997	5018.7	4965.9	5427.2
4624.8	3.3001	4661.1	4611.4	5029.8
4345.4	3.3994	4342.6	4296.0	4680.1
4089.7	3.5000	4055.4	4011.6	4362.6
3859.9	3.5996	3799.7	3760.0	4081.6
3649.8	3.6996	3567.2	3530.2	3825.6
3457.3	3.7998	3355.6	3322.3	3594.6
3279.7	3.9006	3162.5	3131.4	3382.9
3118.7	3.9999	2987.0	2959.6	3192.4
2972.1	4.0977	2830.8	2805.2	3022.7
2830.1	4.1999	2678.2	2655.6	2856.5
2699.4	4.3013	2539.8	2519.1	2707.0
2579.6	4.4011	2414.4	2396.0	2571.2
2467.9	4.5008	2296.9	2280.6	2445.1
2363.1	4.6007	2187.8	2173.4	2327.3
2266.4	4.6991	2088.0	2075.3	2219.9
2173.0	4.8004	1992.0	1981.4	2116.6
2086.8	4.9001	1903.5	1894.2	2022.1
2005.1	5.0007	1820.7	1813.2	1932.9

[a] T is the temperature associated with the adjacent value of resistance for R_I, which was previously calibrated against T_{58} [2].

might otherwise arise in comparing the five individual calibrations of resistor I. Table 6 possesses no calibration data above 4.2 °K because obvious experimental difficulties,[3] which rendered the data invalid, occurred at calibration temperatures above 4.2 °K.

The calibration data for resistor I will be treated separately in a later section of the paper. The data for the other nine resistors has been subjected to computer fitting and analysis for a polynomial of the form

$$\log_{10} R = \sum_{n=0}^{m} A_n (\log_{10} T)^n.$$

The determined coefficients and their uncertainties are given in table 9. Again it is to be noted that: the calibrations of resistors in run VI cover a shorter temperature interval (2.1 to 4.2 °K); and the polynomial fitting of this data would be expected to produce coefficients that are significantly different from the coefficients representing the calibration of other resistors.

[3] The experimental difficulty applies to run 6 (table 6) only, and was connected with the determination of the current that flowed through the resistor circuit during the 4.3 to 5.0 °K calibration.

TABLE 8

Run 9

Calibration data for Resistor K, Resistor E, and Resistor I

R_1	T^a	R_K	R_E	R_I
Ω	°K	Ω	Ω	Ω
13251	2.1011	14099	16802	17134
11750	2.2013	12377	14658	14889
10603	2.2928	11073	13043	13215
9519.2	2.3956	9845.9	11541	11645
8605.8	2.4984	8827.4	10291	10366
7845.3	2.5987	7979.3	9257.5	9302.0
7108.5	2.7124	7167.2	8273.2	8293.0
6615.9	2.7998	6628.7	7622.6	7626.2
6124.4	2.8983	6094.3	6979.8	6971.4
5683.6	2.9983	5616.8	6411.0	6392.9
5291.4	3.0985	5198.0	5908.8	5883.6
4946.7	3.1972	4827.1	5470.8	5440.2
4631.6	3.2978	4492.5	5075.0	5040.1
4350.9	3.3974	4195.7	4725.7	4688.3
4096.8	3.4971	3928.4	4411.8	4372.5
3865.3	3.5972	3686.7	4129.0	4088.7
3656.9	3.6961	3469.9	3876.4	3835.6
3465.5	3.7954	3271.4	3646.0	3605.0
3281.9	3.8993	3082.2	3426.8	3386.4
3120.3	3.9989	2916.5	3235.7	3195.7
2971.1	4.0984	2763.9	3060.6	3021.5
2827.7	4.2017	2618.0	2892.8	2855.2
2700.5	4.3004	2489.1	2745.6	2709.4
2580.8	4.4001	2368.1	2607.5	2572.8
2469.4	4.4994	2255.3	2479.6	2446.8
2363.8	4.6000	2150.2	2360.2	2329.3
2266.7	4.6988	2052.7	2250.1	2220.6
2173.8	4.7995	1960.1	2145.3	2117.9
2086.9	4.8999	1874.0	2048.9	2022.6
2006.4	4.9990	1794.5	1958.9	1934.7

[a] T is the temperature associated with the adjacent value of resistance for R_1, which was previously calibrated against T_{58} [2].

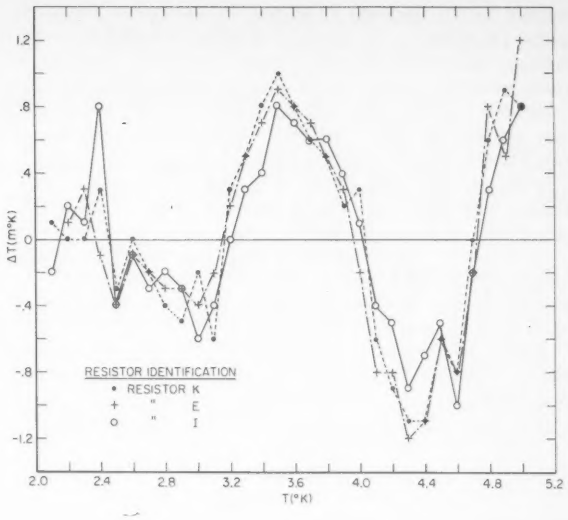

FIGURE 6. *Differences between the fitted functions,*

$$log\ R = \sum_{n=0}^{3} A_n\ (log\ T)^n$$

and the calibration data for resistors K, E, *and* I.

(a) See (a) of figure 4.

(b) The residual plots apply to the three resistors [K (.), E (+) and I (0)]; the calibration data for each resistor have been individually fitted to third order polynomials.

Similarities are to be detected in comparing the general characteristics of the coefficients in table 9. The third and fifth order polynomial fittings yield well determined coefficients while the fourth and sixth order coefficients, in some instances, leave much to be desired. The A_0's of the seventh order are generally not statistically significant.

The plots, for resistors K and E, in figures 6, 7, and 8 are representative of corresponding plots for resistors C, F, G, H, J, L, and M. That is, the systematic deviations (between the calibration data points [R_{data}, T_{data}] and the fitted functions [R_{calc}, T_{data}]) portrayed in figures 6 and 7 are most similar to residual plots of identical polynomial orders for the other seven resistors. The randomness of deviations for the seventh order polynomial (fig. 8) is also representative.

It is interesting to note that, with the exception of run VI, the corresponding coefficients for all of the resistors are generally of comparable magnitudes and identical signs. This observation is most pertinent to the coefficients of the third and fifth order polynomials, where the coefficients are properly significant; and, excepting A_0's, to the coefficients of the seventh order as well.

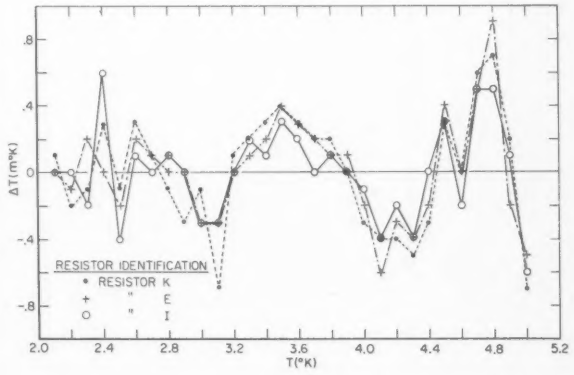

FIGURE 7. *Differences between the fitted functions,*

$$log\ R = \sum_{n=0}^{5} A_n\ (log\ T)^n$$

and the calibration data for resistors K, E, *and* I.

(a) See (a) of figure 4.

(b) The residual plots apply to the three resistors [K (.), E (+) and I (0)]; the calibration data for each resistor have been individually fitted to fifth order polynomials.

TABLE 9. *Coefficients determined from fitting the polynomial* $\log_{10} R = \sum_{n=0}^{m} A_n (\log_{10} T)^n$ *to the calibration data of resistors*

		Run III		Run V				Run VI				Run VII				Run IX			
		Resistor L		Resistor H		Resistor M		Resistor C		Resistor G		Resistor F		Resistor J		Resistor K		Resistor E	
		Coef.	δC [b]	Coef.	δC [b]	Coef.	δC [b]	Coef.	δC [b]	Coef.	δC [b]	Coef.	δC [b]	Coef.	δC [b]	Coef.	δC [b]	Coef.	δC [b]
$n=3$	A_0	5.367	(0.003)	5.328	(0.004)	5.280	(0.003)	5.330	(0.003)	5.317	(0.004)	5.388	(0.003)	5.398	(0.003)	5.319	(0.003)	5.439	(0.003)
	A_1	−4.638	(.02)	−4.538	(.02)	−4.478	(.02)	−4.486	(.02)	−4.467	(.03)	−4.683	(.02)	−4.724	(.02)	−4.597	(.02)	−4.733	(.02)
	A_2	3.522	(.04)	3.385	(.05)	3.492	(.03)	3.308	(.04)	3.196	(.06)	3.471	(.04)	3.466	(.04)	3.575	(.04)	3.542	(.04)
	A_3	−1.685	(.03)	−1.573	(.03)	−1.737	(.02)	−1.537	(.03)	−1.467	(.04)	−1.611	(.02)	−1.556	(.03)	−1.752	(.03)	−1.667	(.03)
	σ [a]	1.6×10^{-4}		1.8×10^{-4}		1.4×10^{-4}		8.5×10^{-5}		1.1×10^{-4}		1.4×10^{-4}		1.6×10^{-4}		1.6×10^{-4}		1.6×10^{-4}	
$n=4$	A_0	5.313	(.014)	5.285	(.017)	5.239	(.012)	5.385	(.014)	5.395	(.016)	5.343	(.012)	5.346	(.014)	5.271	(0.14)	5.385	(.014)
	A_1	−4.186	(.11)	−4.174	(.14)	−4.136	(.10)	−4.969	(.12)	−5.164	(.14)	−4.308	(.10)	−4.293	(.11)	−4.200	(.11)	−4.282	(.11)
	A_2	2.147	(.34)	2.276	(.43)	2.448	(.30)	4.884	(.40)	5.469	(.45)	2.329	(.29)	2.154	(.36)	2.364	(.35)	2.167	(.34)
	A_3	[.135]	(.45)	[−.104]	(.56)	[−.355]	(.40)	−3.787	(.56)	−4.711	(.65)	[−.099]	(.39)	[.182]	(.47)	[−.147]	(.46)	[.154]	(.45)
	A_4	−.885	(.22)	−.715	(.27)	−.672	(.20)	1.185	(.3)	1.709	(.34)	−.736	(.19)	−.845	(.23)	−.781	(.22)	−.886	(.22)
	σ [a]	1.3×10^{-4}		1.6×10^{-4}		1.1×10^{-4}		6.2×10^{-5}		7.2×10^{-5}		1.1×10^{-4}		1.3×10^{-4}		1.3×10^{-4}		1.3×10^{-4}	
$n=5$	A_0	5.588	(.04)	5.578	(.06)	5.466	(.04)	5.422	(.084)	5.412	(.097)	5.531	(.05)	5.580	(.06)	5.506	(.05)	5.642	(.04)
	A_1	−7.059	(.44)	−7.243	(.66)	−6.511	(.42)	−5.379	(.93)	−5.344	(1.1)	−6.273	(.48)	−6.733	(.58)	−6.662	(.55)	−6.968	(.46)
	A_2	13.94	(1.8)	14.87	(2.7)	12.19	(1.7)	[6.683]	(4.0)	[6.26]	(4.7)	10.389	(2.0)	12.164	(2.3)	12.466	(2.2)	13.19	(1.9)
	A_3	−23.65	(3.6)	−25.47	(5.4)	−19.98	(3.4)	[−7.677]	(8.7)	[−6.42]	(10.1)	−16.337	(4.0)	−19.984	(4.7)	−20.506	(4.5)	−22.05	(3.8)
	A_4	22.69	(3.6)	24.41	(5.4)	18.77	(3.4)	[5.340]	(9.3)	[3.53]	(11.)	15.347	(3.9)	19.128	(4.7)	19.39	(4.5)	21.11	(3.7)
	A_5	−9.198	(1.4)	−9.797	(2.1)	−7.580	(1.3)	[−1.753]	(3.9)	[−.78]	(4.6)	−6.270	(1.5)	−7.787	(1.8)	−7.864	(1.7)	−8.577	(1.4)
	σ [a]	7.7×10^{-5}		1.2×10^{-4}		7.6×10^{-5}		6.4×10^{-5}		7.5×10^{-5}		8.6×10^{-5}		1.0×10^{-4}		9.9×10^{-5}		8.3×10^{-5}	
$n=6$	A_0	6.015	(0.2)	6.197	(0.31)	5.656	(0.21)	3.992	(0.37)	3.941	(0.48)	5.7	(0.24)	5.9	(2.8)	5.8	(0.27)	6.03	(0.22)
	A_1	−12.43	(2.5)	−15.02	(3.9)	−8.89	(2.6)	13.69	(5.0)	14.27	(6.4)	−8.8	(3.)	−11.3	(3.5)	−10.3	(3.4)	−11.79	(2.7)
	A_2	41.63	(13.)	54.96	(20.)	[24.49]	(13.5)	−98.1	(27.)	−101.5	(35.)	[23.]	(15.)	35.66	(18.)	[31.]	(17.)	38.06	(14.)
	A_3	−98.72	(35.)	−134.2	(54.)	[−53.31]	(37.)	296.	(79.)	306.2	(101.)	[−52.]	(42.)	[−84.]	(49.)	[−71.]	(47.)	−89.49	(38.)
	A_4	135.6	(52.)	187.8	(80.)	[68.87]	(55.)	−485.	(127.)	−501.1	(162.)	[69.]	(62.)	[115.]	(73.)	[95.]	(71.)	122.5	(57.)
	A_5	−98.49	(41.)	−139.0	(63.)	[−47.20]	(43.)	416.	(108.)	429.3	(138.)	[−49.]	(49.)	[−83.]	(58.)	[−68.]	(56.)	−88.79	(45.)
	A_6	29.05	(13.)	42.01	(21.)	[12.9]	(14.)	−147.	(38.)	−151.2	(49.)	[14.]	(16.)	[25.]	(19.)	[20.]	(18.)	[26.09]	(15.)
	σ [a]	7.2×10^{-5}		1.1×10^{-4}		7.6×10^{-5}		4.7×10^{-5}		6.0×10^{-5}		8.6×10^{-5}		1.0×10^{-4}		9.8×10^{-5}		7.9×10^{-5}	
$n=7$	A_0	1.635	(0.5)	[1.780]	(1.4)	1.371	(0.66)	[3.8]	(2.3)	[4.3]	(3.0)	[1.396]	(0.9)	[.545]	(1.0)	[.305]	(0.8)	2.353	(0.9)
	A_1	51.82	(7.5)	49.78	(20.)	53.96	(9.7)	[16.]	(36.)	[9.]	(46.)	54.79	(13.)	67.86	(14.6)	70.26	(12.)	42.10	(13.)
	A_2	−357.2	(46.)	−347.2	(124.)	−365.7	(60.)	[−116.]	(238.)	[−68.]	(303.)	−371.3	(83.)	−455.6	(90.)	−469.	(75.)	−296.5	(77.)
	A_3	1260.	(157.)	1236.	(419.)	1276.	(203.)	[362.]	(863.)	[183.]	(1100.)	1292.5	(280.)	1589.	(306.)	1633.	(256.)	1051.	(263.)
	A_4	−2607.	(316.)	−2578.	(845.)	−2614.	(408.)	[−629.]	(1860.)	[−235.]	(2400.)	−2645.	(564.)	−3262.	(620.)	−3346.	(516.)	−2180.	(529.)
	A_5	3184.	(378.)	3172.	(1010.)	3165.	(488.)	[601.]	(2390.)	[87.]	(3060.)	3200.	(674.)	3959.	(736.)	4053.	(616.)	2669.	(632.)
	A_6	−2129.	(248.)	−2135.	(663.)	−2099.	(321.)	[−278.]	(1700.)	[91.]	(2200.)	−2122.	(443.)	−2633.	(484.)	−2691.	(405.)	−1788.	(415.)
	A_7	601.3	(69.)	606.9	(185.)	589.	(89.)	[39.]	(510.)	[−73.]	(650.)	595.3	(123.)	740.7	(135.)	756.	(113.)	505.6	(116.)
	σ [a]	3.4×10^{-5}		9.3×10^{-5}		4.5×10^{-5}		4.9×10^{-5}		6.2×10^{-5}		6.2×10^{-5}		6.8×10^{-5}		5.8×10^{-5}		5.9×10^{-5}	

[a] σ is the standard deviation computed from the residuals resulting from the polynomial least squares fitting.
[b] δC is the standard error of the adjacent coefficient.
[ ] Statistically, the bracketed coefficients are poorly determined.

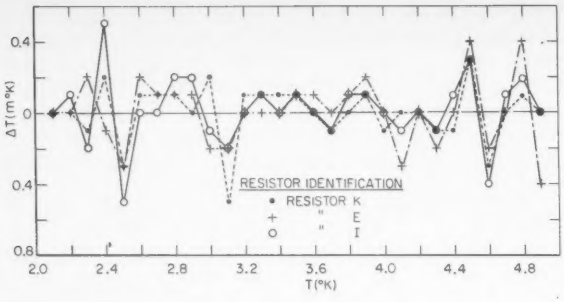

FIGURE 8. *Differences between the fitted functions,*

$$\log R = \sum_{n=0}^{7} A_n (\log T)^n,$$

and the calibration data for resistors K, E, *and* I.

(a) See (a) of figure 4.
(b) The residual plots apply to the three resistors [K (.), E (+) and I (0)]; the calibration data for each resistor have been individually fitted to seventh order polynomials.

5.3. Analysis of the Control Resistor Data

The five individual calibrations of resistor I have been afforded a separate consideration since this resistor served as a "control" through all of the reported calibrations. Its values of resistance, when compared with the corresponding values for resistor #1 (or more appropriately temperatures derived from resistor #1), indicated that all calibrations of resistor I were consistant within ±0.0007 °K. While no progressive drifting of the calibrations was observed (from Run III to IX), Run VII accounted for the largest portion of the maximum calibration deviation within the group of five runs; we are unable to ascertain specific causes for this occurrence.

The calibration data for resistor I have been functionally fitted in the same manner as was described in 5.1. Each of the five calibrations was treated independently and the resulting coefficients are listed in table 10. (The statistical uncertainty of each coefficient is within the adjacent parenthesis.) Since the coefficients of Run VI (table 9) are based upon calibration data that terminated at 4.2 °K, one must be cautious in comparing these coefficients with those of the other four calibration runs. Consequently, the general comparison between corresponding coefficients will be limited to Runs III, V, VII, and IX. Several conclusions are readily apparent.

(a) Third order fittings—the four coefficients are in excellent agreement (within, of course, the limits of

TABLE 10. *Coefficients determined from fitting the polynomial* $\log_{10} R = \sum_{n=0}^{m} A_n (\log_{10} T)^n$ *to the calibration data of resistor I*

	Run III		Run V		Run VI		Run VII		Run IX		Combined data	
	Resistor	δC [b]	Resistor	δC [b]	Resistor	δC [b]	Resistor	δC [b]	Resistor	δC [b]	Resistor	δC [b]
A_0	5.473	(0.0036)	5.473	(0.003)	5.459	(0.004)	5.474	(0.0027)	5.476	(0.0034)	5.473	(0.002)
A_1	−4.806	(.02)	−4.805	(.020)	−4.713	(.025)	−4.815	(.017)	−4.823	(.0206)	−4.806	(.011)
A_2	3.488	(.04)	3.487	(.039)	3.289	(.054)	3.508	(.033)	3.522	(.0409)	3.489	(.022)
A_3	−1.556	(.03)	−1.555	(.025)	−1.416	(.038)	−1.569	(.021)	−1.577	(.026)	−1.556	(.014)
σ [a]	1.7×10^{-4}		1.5×10^{-4}		1.0×10^{-4}		1.2×10^{-4}		1.6×10^{-4}		1.8×10^{-4}	
A_0	5.425	(.015)	5.426	(.013)	5.521	(.017)	5.443	(.012)	5.454	(.017)	5.438	(.008)
A_1	−4.404	(.13)	−4.42	(.11)	−5.265	(.15)	−4.540	(.10)	−4.639	(.14)	−4.512	(.070)
A_2	2.265	(.39)	2.31	(.34)	5.089	(.49)	2.671	(.31)	2.962	(.42)	2.590	(.21)
A_3	[.0632]	(.51)	[.0008]	(.44)	− 3.985	(.7)	[−.460]	(.41)	[−.835]	(.55)	[−.363]	(.28)
A_4	−.787	(.25)	−.76	(.22)	1.354	(.37)	−.539	(.20)	[−.361]	(.27)	−.582	(.14)
σ [a]	1.4×10^{-4}		1.3×10^{-4}		$.8\times10^{-5}$		1.2×10^{-4}		1.6×10^{-4}		1.7×10^{-4}	
A_0	5.724	(.05)	5.710	(.04)	5.714	(.094)	5.655	(.046)	5.780	(.053)	5.714	(.035)
A_1	−7.539	(.51)	−7.386	(.38)	−7.407	(1.03)	−6.757	(.47)	−8.045	(.55)	−7.409	(.37)
A_2	15.14	(2.1)	14.48	(1.5)	14.48	(4.5)	11.765	(1.9)	16.936	(2.2)	14.50	(1.5)
A_3	−25.89	(4.2)	−24.52	(3.1)	−24.30	(9.8)	−18.782	(3.9)	−29.00	(4.5)	−24.43	(3.0)
A_4	24.94	(4.2)	23.53	(3.0)	23.05	(10.4)	17.607	(3.8)	27.54	(4.4)	23.31	(3.0)
A_5	−10.04	(1.6)	−9.47	(1.2)	−9.154	(4.4)	−7.074	(1.5)	−10.88	(1.7)	−9.34	(1.2)
σ [a]	9.0×10^{-5}		6.7×10^{-5}		7.2×10^{-5}		8.4×10^{-5}		9.8×10^{-5}		1.4×10^{-4}	
A_0	5.966	(0.25)	5.98	(.18)	4.069	(0.41)	5.60	0.24	6.09	.27	5.89	0.18
A_1	−10.57	(3.1)	−10.8	(2.3)	14.536	(5.4)	16.04	(3.0)	−11.98	(3.4)	−9.61	(2.3)
A_2	[30.78]	(16.)	32.0	(11.7)	−106.14	(30.)	[8.06]	(15.)	37.21	(17.4)	25.86	(11.7)
A_3	[−68.31]	(43.)	−71.9	(32.)	325.5	(86.)	[−8.73]	(41.)	[−84.00]	(47.0)	[−55.27]	(32.)
A_4	[88.7]	(65.)	94.7	(47.4)	−541.6	(138.)	[2.51]	(62.)	[110.2]	(70.5)	[69.8]	(47.)
A_5	[−60.5]	(51.)	[−65.8]	(37.4)	472.1	(118.)	[4.87]	(49.)	[−76.267]	(55.7)	[−46.]	(38.)
A_6	[16.4]	(17.)	[18.3]	(12.1)	−169.2	(41.)	[−3.88]	(16.)	[21.3]	(18.1)	[12.]	(12.)
σ [a]	9.0×10^{-5}		6.6×10^{-5}		5.1×10^{-5}		8.6×10^{-5}		9.8×10^{-5}		1.4×10^{-4}	
A_0	[0.193]	(0.5)	2.0915	(.51)	[2.7]	(2.5)	2.049	(1.1)	3.015	(1.3)	1.857	(0.90)
A_1	74.11	(7.4)	46.26	(7.4)	[35.]	(39.)	45.98	(15.)	33.18	(18.7)	49.60	(13.1)
A_2	−495.	(46.)	−322.	(46.)	[−244.]	(255.)	−314.8	(95.)	−243.2	(116.)	−342.1	(81.2)
A_3	1722.	(155.)	1134.	(155.)	[828.]	(926.)	1091.	(322.)	871.4	(394.)	1200.	(276.)
A_4	−3526.	(312.)	−2340.	(313.)	[−1628.]	(2000.)	−2217.	(649.)	−1819.	(793.)	−2467.	(557.)
A_5	4266.	(373.)	2849.	(374.)	[1870.]	(2568.)	2661.	(775.)	2234.	(948.)	2995.	(666.)
A_6	−2828.	(245.)	−1899.	(246.)	[−1160.]	(1819.)	−1750.	(509.)	−1499.	(623.)	−1990.	(438.)
A_7	793.	(68.)	534.	(68.)	[299.]	(548.)	4867.	(142.)	424.	(174.)	559.	(1.22)
σ [a]	3.4×10^{-5}		3.5×10^{-5}		5.2×10^{-5}		7.1×10^{-5}		8.9×10^{-5}		1.3×10^{-4}	

[a] σ is the standard deviation computed from the residuals resulting from the polynomial least squares fitting.
[b] δC is the standard error of the adjacent coefficient.
[ ] Statistically, the bracketed coefficients are poorly determined.

the stated statistical uncertainties). Furthermore, the ratio of an individual coefficient to its respective uncertainty indicates rather well defined coefficients, and the standard deviations of the individual least squares fittings are comparable.

(b) Fourth order fittings—while similarities exist between some coefficients, two features clearly indicate that this order of polynomial fitting presents no advantage. The A_3's are not defined, and the standard deviations, σ, show little improvement over the third order of fittings.

(c) Fifth order fittings—the coefficients, with respect to their statistical uncertainties, are clearly not as well defined as those of the third order polynomial; but the ratios are generally greater than six to one. More important, the standard deviations in polynomial fitting have materially improved over the third order thus indicating the superiority of the fifth degree for representing the calibration data. Here also, most of the corresponding coefficients i.e., A_0's, . . . A_5's, are nearly identical within the limits of their statistical uncertainties. Those from run VII exhibit noticeable divergencies; several paragraphs earlier we pointed out that the calibration data for run VII exhibited maximum variance with the other calibrations.

(d) Sixth order fittings—clearly, a sixth order polynomial produces no beneficial result.

(e) Seventh order fitting—while we should like to employ a seventh order polynomial for the data representation, the inconsistencies of the coefficients (A_0 and A_1 in particular) for run III clearly imply the possibility of its impropriety.

The polynomial coefficients for run VI, where the data is terminated at the upper limit of 4.2 °K, generally exhibit different qualitative trends, but are in quantitative agreement with the corresponding coefficients of the other runs for the fifth order polynomial. The general conclusion, which may be drawn from the comparison of the determined coefficients, strongly suggests that a fifth order polynomial offers a consistant representation for all of the calibration data (for resistor I) and that the standard deviation of such a fitting is about 9×10^{-5}. Deviations of the individual data points (Resistor I) from the fitted third order polynomial (run IX) are shown in figure 6. The curves' significant features are duplicated, within a spread of ± 0.0002 °K, for the corresponding representations of runs III, V, and VII. In the case of run VI, the general departures from the base line are reduced in size.

Figure 7, which portrays the deviations of individual data points (Resistor I) from the fitted fifth order polynomial (run IX), is also representative of the other complete calibrations of resistor I. While it exhibits systematic deviations, they are much less than those exhibited in figure 6. A comparable plot (figure 8), associated with the seventh order polynomial, exhibits a random distribution; although this condition is desirable, the indeterminacy of run III's seventh order coefficients causes us to hesitate in advocating use of the seventh order polynomial for representing this calibration data.

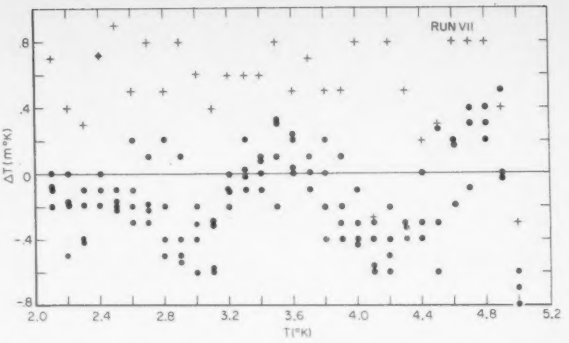

FIGURE 9. *Differences between the fitted function,*

$$log\ R = \sum_{n=0}^{5} A_n\ (log\ T)^n,$$

and all of the calibration data for resistor I.

(a) See (a) of figure 4.

(b) The residual plots apply to all of resistor I's calibration data (Runs III, V, VI, VII, and IX) which have been fitted to a fifth order polynomial. Residuals for Run VII are specifically identified (+).

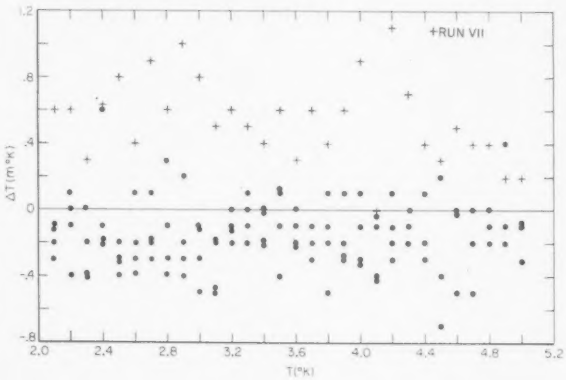

FIGURE 10. *Differences between the fitted function,*

$$log\ R = \sum_{n=0}^{7} A_n\ (log\ T)^n$$

and all of the calibration data for resistor I.

(a) See (a) of figure 4.

(b) The residual plots apply to all of resistor I's calibrated data (Runs III, VI, VII, and IX) which have been fitted to a seventh order polynomial. Residuals for Run VII are specifically identified.

In summary, the preceeding paragraphs have indicated that through the five calibration runs: the reference resistor #1 and the control resistor I have exhibited relative calibration constancies that are within a temperature equivalent of ± 0.0007 °K; additionally, for I, the third and fifth order polynomial coefficients are consistantly determined within the limits of their computed uncertainties.

Recognizing that the polynomial fittings of individual calibrations for I are somewhat restrictive in intercomparisons between different calibrations, we have "polyfitted" all of the resistor I data. The resulting coefficients, listed in the last column of table 10, are generally not significantly different (within the limits of the coefficients' uncertainties) from the coefficients of runs III, V, VII, and IX. Figures 9 and 10 are plots of deviations between the calibration data (R_{data}, T_{data}) and the fitted polynomials (R_{calc}, T_{data}) for the 5th and 7th order polynomials respectively. It is obvious in both plots that the data points from run VII consistently deviate from the rest of the calibration data and this accounts for the increased standard deviation that appears in the polynomial fittings of the last column. For each calibration temperature in figures 9 and 10 it is apparent that all of the calibrations agree within ± 0.0007 °K.

As a final criterion on the general validity of calibrations within the calibrator we have spot-checked the calibrations of run IX. Resistors I, K, and E were calibrated directly against helium-4 vapor pressures, in a constant temperature bath, at 2.2, 3.0, and 4.2 °K. Comparisons were made with the previous calibrations of run IX and the calibration differences (in temperature equivalents) are shown in table 11. Overall, the agreement between the calibrations is reasonable although the discrepancies at 4.2 and 3.0 °K for resistor I are somewhat large.

TABLE 11. *Intercomparison of calibrations from two methods* [a]

	Temperature difference		
4.2 °K	*mdeg* [b] +1.4	*mdeg* [b] +0.2	*mdeg* [b] −0.75
3.0 °K	−1.2	0.0	−0.7
2.2 °K	+0.5	+0.2	−0.1
	Resistor I [c]	Resistor K [c]	Resistor E [c]

[a] Method A—the resistors were calibrated within the calibrator against resistor #1.
Method B—the resistors were calibrated within a "constant temperature" liquid helium bath against T_{58} [2] by means of vapor pressure measurements.
[b] The positive sign (+) means, for the same value of resistance, T (°K) of method B is greater than T (°K) of method A.
[c] Previous thermal histories indicated that, under 86 thermal cyclings between ambient temperatures and 4.2 °K, the 4.2 °K calibrations of resistors I, K, and E were reproducible to 0.8, 1.1 and 1.0 mdeg respectively.

6. Conclusions

We have shown that the resistance-temperature calibration (from 2.1 to 5.0 °K) for a particular group of ten similar germanium resistors can be represented by a polynomial function within the approximate limits of the calibration errors. In each case, based upon appropriate polynomial coefficients (fourth degree polynomials for resistors C and G, and fifth degree for the rest), generations of R, $\frac{dR}{dT}$ and $\frac{d^2R}{dT^2}$ as a function of T (every 0.010 °K) have demonstrated that the determined polynomials are smooth (within the range 2.1 to 5.0 °K); the first and second derivatives do not change sign. While these conclusions are encouraging for the prospects of employing a fitted polynomial function to interpolate between calibration points, it should be stressed that the results apply to a select group of resistors. Also, caution should be employed in any attempts to use the polynomials for extrapolations beyond the calibration region.

The type of polynomial that has been used in this work,

$$\log_{10} R = \sum_{n=0}^{m} A_n (\log_{10} T)^n,$$

has been selected somewhat arbitrarily. There is no theoretical basis for selecting this polynomial to represent the resistors' calibration data, and the fitting of the polynomial has been an empirical procedure that is applicable to the limited range of calibration data. The values of the determined A_0's for any given resistor in table 10, indicate the inappropriateness of extrapolations based upon the determined polynomials. Additionally, when we have occasionally performed R, $\frac{dR}{dT}$ and $\frac{d^2R}{dT^2}$ generations (based on fitted polynomials) that extended beyond the calibration range, we found that the functions became erratic at external temperatures.

We believe that the polynomial, which we have employed, is not necessarily the most appropriate function for representing the calibration data of these resistors. However it does serve as an interpolation aid that can be cautiously used until a more meaningful representation is achieved. In the immediate future we shall seek to find improved functions not only for the data presented in this paper but for more extensive calibration data (2.3 to 20 °K) that we have previously published [1].

7. References

[1] M. H. Edlow and H. H. Plumb, J. Res. NBS **70C** (Eng. and Instr.), No. 4, 245 (1966).
[2] F. G. Brickwedde, H. van Dijk, M. Durieux, J. R. Clement, and J. K. Logan, J. Res. NBS **64A** (Phys. and Chem.), No. 1, 1 (1960).
[3] G. Cataland, M. H. Edlow, and H. H. Plumb, Rev. Sci. Instr. **32,** 980 (1961); W. G. Brombacher, D. P. Johnson, and J. L. Cross, NBS Monograph **8** (1960).
[4] G. Cataland, M. H. Edlow, and H. H. Plumb, in Temperature, Its Measurement and Control in Science and Industry, C. M. Herzfeld, ed., **3,** F. G. Brickwedde, ed., Pt. 1, 413 (Reinhold Publishing Corp., New York, 1962).
[5] M. Durieux, Thesis, University of Leiden (1960); M. H. Edlow and H. H. Plumb in Advances in Cryogenic Engineering, K. D. Timmerhaus, ed. **6,** 542 (Plenum Press, Inc., New York, 1961).
[6] K. W. Taconis, J. J. Beenakker, A. O. C. Nier, and L. T. Aldrich, Physica **15,** 733 (1949); H. A. Kramers, ibid, p. 971; D. A. Ditmars and G. T. Furukawa, J. Res. NBS **69C** (Phys. and Chem.), No. 1, 35 (1965).
[7] E. Ambler and H. H. Plumb, Rev. Sci. Instru. **31,** 656 (1960).

(Paper 71C1–441)

JOURNAL OF RESEARCH of the National Bureau of Standards—C. Engineering and Instrumentation
Vol. 71C, No. 1, January–March 1967

Least Squares Technique for the Analysis of Periodic Temperatures of the Earth's Surface Region

Tamami Kusuda

Institute for Applied Technology, National Bureau of Standards, Washington, D.C. 20234

(October 19, 1966)

A least squares technique has been applied to periodic earth temperature data for the purpose of determining basic characteristics of earth temperature cycles, such as thermal diffusivity, average temperature, amplitude, and phase angle of the temperature cycle. A new procedure was developed for obtaining a single thermal diffusivity which represents an average over time and depth at a particular temperature site. This thermal diffusivity was obtained as a nonlinear part of least squares constants which yielded a best-fit harmonic curve to a given set of observed earth temperatures. The thermal diffusivity thus calculated and the calculation method developed are preferred to those obtained by current practice, which yields two thermal diffusivities, one based on amplitude decay and another on phase angle shift.

Key Words: Earth temperature, least squares technique, thermal diffusivity of earth.

Nomenclature

$A_0, A_1, A_2, \ldots A_N$ = Least squares constants or best unbiased estimates of $a_0, a_1, a_2, \ldots a_N$ (°C)

$a_0, a_1, a_2, \ldots a_N$ = Cosine coefficients of expected earth temperature function (°C)

$B_1, B_2, B_3, \ldots B_N$ = Least squares constants or best unbiased estimates of $b_1, b_2, b_3, \ldots b_N$ (°C)

$b_1, b_2, b_3, \ldots b_N$ = Sine coefficient of expected earth temperature function (°C)

$\hat{B}_i(x)$ = ith harmonic amplitude of earth temperature cycle at depth x (°C)

C_i or $C_{i,K}$ = Linearized variables (dimensionless)

D = A least squares estimate of average thermal diffusivity, α (cm²/sec)

$F(\theta)$ = Surface temperature function

G_i = Amplitude of ith harmonic coefficients = $\sqrt{a_i^2+b_i^2}$ (°C)

M = Total number of temperature data (number of time data multiplied by number of depth data) (dimensionless)

M_t = Total number of cycles to be considered (dimensionless)

M_x = Total number of depths to be considered (dimensionless)

N = Highest order of harmonics to be included for expected earth temperature function (dimensionless)

$\hat{P}_i(x)$ = Phase angle of ith harmonic of earth temperature cycle at depth x, (radians)

SS = Sum of squares of all of the differences between observed and expected earth temperatures

S_i or $S_{i,k}$ = Linearized variables (dimensionless)

T = Period of cyclic data (31,557,600 sec for annual cycle)

t = Earth temperature (°C)

t_∞ = Earth temperature at $x \to \infty$ (°C)

t_k = Observed earth temperature (°C)

x = Depth in earth (cm)

x_k = Observed depth in earth (cm)

Greek Characters

α = Expected thermal diffusivity of earth (cm²/sec)

β_i = Temperature decay factor = $\sqrt{\frac{i\pi}{\alpha T}}$ (cm^{-1})

$\bar{\beta}_i$ = Estimate of $\beta_i = \sqrt{\frac{i\pi}{DT}}$ (cm^{-1})

$\delta = \frac{\partial SS}{\partial D}$

θ = Time coordinate used in the text, measured from January 1 (sec)

θ_k = Observed time with datum point at January 1 (sec)

Φ_i = Phase angle of ith harmonic of earth temperature, (radians) $\Phi_i = \tan^{-1}\frac{b_i}{a_i}$

Δ = Root mean squared deviation (defined in the text).

1. Objective

The purpose of this paper is to discuss a harmonic analysis of cyclic temperatures at selected depths of earth. The existing techniques employing a simple

harmonic equation [Kusuda, 1965; Penrod, 1960] or Fourier analysis [Carson, 1963] have the disadvantage of yielding different thermal diffusivities for a given set of data, depending upon the choice of data reduction method, choice of cyclic period, choice of two depths, and the choice of computational method. The technique introduced in this paper eliminates this disadvantage and it is statistically more sound than previous methods for the analysis of periodic depth temperatures of earth. Furthermore, the method derived herein may be applied for the accurate calculation of thermal diffusivity of the surface layer of other celestial bodies in the event cyclic patterns of their depth temperatures are obtained in the future.

2. Introduction and General Background

Numerous investigators in the past have studied earth temperatures with reference to the earth's thermal diffusivity. A recent publication of Kusuda and Achenback [1965] includes an extensive bibliography on the subject. Most of the analyses in the papers listed in this bibliography apply the well-known periodic heat conduction formula for either diurnal or annual (or both) cycles of observed earth temperatures.

These analyses have been made to establish the average, the amplitude, and the phase angle of cyclic temperature patterns at various depth levels, so that earth temperatures may be predicted by a computational method. The amplitude decays and phase angle shifts of temperature cycles with respect to depths have been used to estimate the thermal diffusivity of the station where the earth observations were made. The analysis of periodic earth temperatures, therefore, eventually ends up with four basic parameters: thermal diffusivity, average temperature, amplitude, and phase angle of the surface temperature cycle from a given datum time point.

The investigators have encountered the following problems during the course of their studies. (1) The earth surface was difficult to define and earth surface temperatures were subject to disturbances from climatic changes above the surface, such as rainfall, cloud cover, evaporation of water, and wind velocity. (2) The actual earth temperatures observed did not follow an ideal simple-harmonic pattern. Moreover, their cyclic patterns varied from year to year and from day to day. Except in the work of Carson and in that of Kusuda and Achenbach, some degree of arbitrary human judgment was exercised to establish meaningful periodic patterns. For example, when several years of monthly average earth temperature records were available, the annual thermal diffusivity was calculated for each set of annual data. Such calculations imply an annual change of thermal diffusivity, which is a misapplication of basic heat conduction theory, as explained later. (3) For a given station, thermal diffusivities were computed both from the difference of logarithmic amplitudes and from the difference of phase angles for two different depths. Unfortunately, the diffusivities calculated by these two methods usually did not agree, differing by a factor of two in some instances [Kusuda, 1965]. (4) When the thermal diffusivities were computed at two different pairs of two-depth levels at a given temperature station, two different estimates of the diffusivity were obtained, even when a consistent method of diffusivity computation was employed.

These four problems resulted in uncertainties of thermal diffusivities due to time, due to depth, due to method of computation, and due to the method of data reduction for a given set of earth conditions at a given locality.

Most of the investigators also attempted to predict earth temperatures based on an average of thermal diffusivities thus computed, and on other basic parameters; namely, the earth surface temperature amplitude, the phase angle of the earth surface temperature cycle measured from a certain reference datum point, and the average earth temperature during the cycle.

Mathematical description of an earth temperature cycle by a Fourier series technique, similar in nature with the least squares technique, has been tried by several authors. The most recent and comprehensive description was made by Carson [1963] for the soil of Lemont, Ill. The Fourier series technique is basically applicable only to a single complete cycle where data points consist of a unique set of temperatures for equally incremented time coordinates. Carson applied the technique to each individual one-year set of monthly average earth temperature cycles over a period of three years, resulting in three sets of Fourier coefficients, which did not agree with each other.

Kusuda and Achenbach [1965] applied a least squares technique in fitting observed earth temperature data to simple harmonic expressions for the purpose of computing the four basic parameters of earth temperature cycles.

In their least squares technique, Kusuda and Achenbach [1965] incorporated several years' records simultaneously, thus treating the temperature data as statistical variables or variates rather than functional variables, which is the case in a Fourier analysis. The least squares technique fits a sinusoidal curve to the observed data in such a manner that the variance calculated from the residual deviations of the observed temperature from the fitted curve is a minimum. The number of data points, the time intervals for the temperature observations, and the number of data for a given time are not restricted as they are in a Fourier analysis.

Kusuda and Achenbach [1965], however, began with the premise that the earth temperature cycles follow a simple harmonic mode. This premise may be reasonably applied to annual cycles of monthly average earth temperatures, but it is not quite valid for diurnal temperature cycles. They, however, still obtained two thermal diffusivities based upon the amplitude decay and phase angle shift techniques, same as those used by other investigators.

The extension of the least squares technique to cover the higher harmonic terms is also desirable if the

method is to be applicable to diurnal earth temperature cycles of the earth theoretically differing from the simple harmonic pattern because of a complex nonlinear surface heat exchange with the sun and the surrounding space.

In the following section the basic heat conduction relation of the periodic temperature cycle is first reviewed. The least squares technique is then applied to annual cycles of monthly average earth temperatures as an illustrative example.

3. Basic Heat Conduction Theory on a Semi-Infinite Solid

The surface layer of earth may be assumed to be a semi-infinite solid having a homogeneous thermal property, as far as the heat conduction theory is concerned. This assumption, however, may be inadequate in some cases, and a more refined model, such as composite solids (an upper layer of finite thickness over an infinitely thick solid bed of different thermal properties), is desirable. As a theory, this composite model probably represents more closely the actual surface of earth than the homogeneous model. But the thickness of the top layer, and the variation of properties between the top layer and the bottom bed are usually unknown, which makes the composite layer nodel less meaningful than the homogeneous model. Also, the mathematical complexity involved for the composite solid model may not be justified in finding an accurate thermal diffusivity of a surface layer from the observed depth temperature cycles. Hence, the homogeneous semi-infinite solid model is used to calculate average thermal diffusivity represented by the surface region of the earth. Or, conversely, temperature cycles at various depths are approximated by the equation derived for semi-infinite heat conduction models of homogeneous thermal properties.

The heat conduction of the semi-infinite homogeneous solid can be mathematically expressed as follows:

$$\alpha \frac{\partial^2 t}{\partial x^2} = \frac{\partial t}{\partial \theta} \tag{1}$$

$$\left.\begin{array}{ll} \text{at } x \to \infty & t \to t_\infty \\ \text{at } x = 0 & t = F(\theta) \\ \text{and } F(\theta + T) = F(\theta) & \end{array}\right] \tag{2}$$

In actuality it is difficult to define a unique $F(\theta)$ that represents daily or annual cyclic observations of earth surface temperatures, since the character of these cycles varies from one period to the next. This variation is due to the varying nature of heat exchange over the earth surface with respect to climatic conditions. It is postulated that other celestial bodies without atmosphere may experience a much more consistent and stable $F(\theta)$ than the earth experiences. In this paper it is assumed that there exists a unique $F(\theta)$, which may be a statistical average of many periodic cycles. Since $F(\theta)$ is a periodic function of period T, it is possible to expand it as follows:

$$F(\theta) = a_0 + \sum_{i=1}^{\infty} a_i \cos\left(\frac{2\pi i}{T}\theta\right) + \sum_{i=1}^{\infty} b_i \sin\left(\frac{2\pi i}{T}\theta\right). \tag{3}$$

The values of $a_0, a_1, a_2, \ldots b_1, b_2, b_3$ are dependent upon the actual nature of the assumed surface temperature cyclic pattern.

The cyclic earth temperature [Eckert, 1959] at depth x that satisfies (1), (2), and (3) is

$$t = t_\infty + \sum_{i=1}^{\infty} a_i e^{-\sqrt{\frac{i\pi}{\alpha T}}x} \cos\left(\frac{2\pi i\theta}{T} - \sqrt{\frac{i\pi}{\alpha T}}x\right) + \sum_{i=1}^{\infty} b_i e^{-\sqrt{\frac{i\pi}{\alpha T}}x} \sin\left(\frac{2\pi i\theta}{T} - \sqrt{\frac{i\pi}{\alpha T}}x\right) \tag{4}$$

(It should be noted from eqs (3) and (4) that $A_0 = t_\infty$). Formula (4) can also be expressed as

$$t = t_\infty + \sum_{i=1}^{\infty} G_i e^{-\sqrt{\frac{i\pi}{\alpha T}}x} \cos\left(\frac{2\pi i\theta}{T} - \Phi_i - \sqrt{\frac{i\pi}{\alpha T}}x\right) \tag{5}$$

where

$$\left.\begin{aligned} G_i &= \sqrt{a_i^2 + b_i^2} \\ \tan \Phi_i &= \frac{b_i}{a_i}. \end{aligned}\right\} \tag{6}$$

By letting

$$\left.\begin{aligned} &G_i e^{-\sqrt{\frac{i\pi}{\alpha T}}x} = \hat{B}_i(x) = \text{depth amplitude} \\ &\Phi_i - \sqrt{\frac{i\pi}{\alpha T}}x = \hat{P}_i(x) = \text{depth phase angle,} \end{aligned}\right\} \tag{7}$$

the thermal diffusivity α can be readily calculated by knowing $\hat{B}_i(x)$ and $\hat{P}_i(x)$ at two different depths x_1 and x_2 by the following formulas:

$$\alpha_{Bi} = \frac{i\pi}{T}\left[\frac{x_1 - x_2}{\log \dfrac{\hat{B}_i(x_2)}{\hat{B}_i(x_1)}}\right]^2, \qquad i = 1, 2 \ldots \infty \tag{8}$$

and

$$\alpha_{Pi} = \frac{i\pi}{T}\left[\frac{x_1 - x_2}{\hat{P}_i(x_1) - \hat{P}_i(x_2)}\right]^2, \qquad i = 1, 2 \ldots \infty. \tag{9}$$

In formulas (8) and (9), notation α_B and α_P are used instead of α to signify that these two thermal diffusivities are computed by amplitudes and by phase angles

of ith harmonic constants, respectively. Theoretically, of course

$$\alpha_{Bi}=\alpha_{Pi}=\alpha \text{ for } i=1, 2, 3, \ldots . \tag{10}$$

Unfortunately, however, these relations have seldom been found in practice. Most previous researchers have made extensive studies on α_{B1} and α_{P1} only, ignoring higher harmonics. Even for the first harmonic constants, agreement between α_{B1} and α_{P1} was poor. Not only that, the values of α_{B1} and α_{P1} varied, as mentioned before, depending upon the choice of x_1 and x_2 of formulas (8) and (9). These difficulties have been chiefly attributed to the fact that the earth surface is not quite homogeneous and the heat conduction characteristics and surface temperature cycle of the earth surface region vary with respect to physical condition and time. The previous difficulties are, however, mostly due to the misuse of formula (4). It is not correct to use formula (4) either for analysis of one given periodic cycle of observation, or for analysis of depth variation of thermal diffusitivity. Instead, formula (4) should be used for the entire temperature data, covering the entire depth and the entire time period. For instance, if ten years of monthly average earth temperature cycles were complete with five depth readings, all of the 600 data points should be considered simultaneously for formula (4) to yield the best fit values of t_∞, $(a_i,\ i=1, 2, 3, \ldots)$ and $(b_i,\ i=1, 2, 3 \ldots)$ as well as the best fit value of α.

It is important here to mention that the foregoing statements are based upon the following statistical hypothesis:

Time data (including all the cyclic periods) follow basically a given harmonic function of a period T (8766 hr for an annual earth cycle). Any deviation of actual cycles from a prescribed harmonic function are statistical rather than functional.

4. The Least Squares Technique

Although the technique described in this paper applies to any kind of periodic temperature data observed at several depths of any semi-solid system, the specific treatment will be given for annual cycles comprising monthly average earth temperatures taken at selected depths.

Assume that the number of annual cycles of earth temperature is M_t and each annual cycle consists of twelve monthly average readings at each of M_x depths. If there are no missing data, although this is not a requirement, the total number of observations M should be

$$M=M_t\times M_x\times 12.$$

Equation (4), however, should be modified to include only the finite number of harmonic terms up to some larger number N. In other words, it is assumed that a_i and b_i will be numerically insignificant for all $i>N$.

The best unbiased estimates of a_0, a_1, . . . a_N, b_1, b_2 . . . b_N, and D, that of α are given by the solutions of the following equations

$$\left.\begin{aligned}&\frac{\partial SS}{\partial A_0}=0\\ &\left.\begin{aligned}&\frac{\partial SS}{\partial A_i}=0\\ &\frac{\partial SS}{\partial B_i}=0\end{aligned}\right\}\text{ for } i=1,2 \ldots N\end{aligned}\right] \tag{11}$$

$$\delta=\frac{\partial SS}{\partial D}=0 \tag{11-a}$$

where A_0, A_1, A_2, . . . A_N, B_1, B_2, . . . B_N and D are the best estimates of a_0, a_1, a_2, . . . a_N, b_0, b_1, b_2, . . . b_N, and α.

$$\text{And}\quad SS=\sum_{k=1}^{M}\left[t_k-A_0-\sum_{i=1}^{N}A_i e^{-\bar{\beta}_i x_k}\cos\left(\frac{2\pi i}{T}\theta_k-\bar{\beta}_i x_k\right)\right.$$
$$\left.-\sum_{i=1}^{N}B_i e^{-\bar{\beta}_i x_k}\sin\left(\frac{2\pi i}{T}\theta_k-\bar{\beta}_i x_k\right)\right]^2 \tag{12}$$

where

$$\bar{\beta}_i=\sqrt{\frac{i\pi}{DT}}.$$

By letting

$$C_{i,k}=e^{-\bar{\beta}_i x_k}\cos\left(\frac{2\pi i}{T}\theta_k-\bar{\beta}_i x_k\right) \tag{13}$$

$$S_{i,k}=e^{-\bar{\beta}_i x_k}\sin\left(\frac{2\pi i}{T}\theta_k-\bar{\beta}_i x_k\right) \tag{14}$$

and by noting that

$\frac{\partial SS}{\partial D}=0$ is also satisfied by $\frac{\partial SS}{\partial \beta_i}=0$ as long as $D\neq 0$,

the equations in (11) can be expressed simply by the linear matrix equation shown in table 1. The left-hand side of the equal sign of table 1 is actually the product of two matrices, one square matrix of $(2N+1)\times(2N+1)$ and one column matrix of dimension $(2N+1)$. Equation (11-a) is nonlinear and is expressed in terms of linearized variables, $C_{i,k}$ and $S_{i,k}$ as is shown in table 2.

Determination of A_0, A_1, A_2, . . . A_N, B_1, B_2, . . . B_N as a best estimate of a_0, a_1, a_2, . . . a_N, b_1, b_2, . . . b_N is straightforward if the $C_{i,k}$'s and $S_{i,k}$'s are known. However, these variables include an unknown D which is to be solved by (11-a).

The method employed in this paper is to calculate a number of sets of A_0, A_i, B_i; $i=1, 2, \ldots N$, for several assumed D's. These calculated sets are then applied to the equation in table 2. By an iterative procedure, a set of A_0, A_i, B_i; $i=1, 2, \ldots N$, and D

TABLE 1. *Matrix expression of least squares equations (normal equations)*

Least Squares Equations

M (1×1)	$\sum_{k=1}^{M} C_{j,k}$ $j=1,N$ $(1\times N)$	$\sum_{k=1}^{M} S_{j,k}$ $j=1,N$ $(1\times N)$	A_0 (1×1)		$\sum_{k=1}^{M} t_k$ (1×1)
$\sum_{k=1}^{M} C_{i,k}$ $i=1,N$ $(N\times1)$	$\sum_{k=1}^{M} C_{i,k}C_{j,k}$ $(N\times N)$	$\sum_{k=1}^{M} C_{i,k}S_{j,k}$ $(N\times N)$	A_i $i=1,N$ $(N\times1)$	$=$	$\sum_{k=1}^{M} C_{i,k}t_k$ $(N\times1)$
$\sum_{k=1}^{M} S_{i,k}$ $i=1,N$ $(N\times1)$	$\sum_{k=1}^{M} S_{i,k}C_{j,k}$ $(N\times N)$	$\sum_{k=1}^{M} S_{i,k}S_{j,k}$ $(N\times N)$	B_i $i=1,N$ $(N\times1)$		$\sum_{k=1}^{M} S_{i,k}t_k$ $(N\times1)$

$$C_{i,k}=e^{-\sqrt{\frac{i\pi}{DT}}x_k}\cos\left(\frac{2\pi i}{T}\theta_k-\sqrt{\frac{i\pi}{DT}}x_k\right)$$

$$S_{i,k}=e^{-\sqrt{\frac{i\pi}{DT}}x_k}\sin\left(\frac{2\pi i}{T}\theta_k-\sqrt{\frac{i\pi}{DT}}x_k\right)$$

$$t=A_0+\sum_{i=1}^{N}A_iC_{i,k}+\sum_{i=1}^{N}B_iS_{i,k}$$

TABLE 2. *Mathematical formula for the partial derivative of the sum of squares of all of the differences between observed and expected earth temperatures with respect to thermal diffusivity*

$$\sum_{i}^{N}\sqrt{i}(A_i+B_i)\sum_{k}^{M}t_kx_kC_{i,k}-\sum_{i}^{N}\sqrt{i}(A_i-B_i)\sum_{k}^{M}t_kx_kS_{i,k}$$

$$-A_0\sum_{i}^{N}\sqrt{i}(A_i+B_i)\sum_{k}^{M}x_kC_{i,k}+A_0\sum_{i}^{N}\sqrt{i}(A_i-B_i)\sum_{k}^{M}x_kS_{i,k}$$

$$-\sum_{i}^{N}A_i\sum_{j}^{N}\sqrt{j}(A_j+B_j)\sum_{k}^{M}C_{i,k}C_{j,k}x_k+\sum_{i}^{N}A_i\sum_{j}^{N}\sqrt{j}(A_j-B_j)\sum_{k}^{M}C_{i,k}S_{j,k}x_k$$

$$-\sum_{i}^{N}B_i\sum_{j}^{N}\sqrt{j}(A_j+B_j)\sum_{k}^{M}S_{i,k}C_{j,k}X_k+\sum_{i}^{N}B_i\sum_{j}^{N}\sqrt{j}(A_j-B_j)\sum_{k}^{M}S_{i,k}S_{j,k}x_k$$

$$=\delta=0$$

can be found to satisfy $\delta=0$ (see table 2). These coefficients and the assumed D are then substituted into formula (12) for the calculation of the mean squared deviation of the fitted least square values from the observed data by the following equation:

$$\Delta^2=\frac{SS}{M}. \tag{15}$$

The value of Δ, or the square root of the average of the sum of squares of deviations is called hereafter the root mean squared deviations (RMSD) of the observed temperatures from those calculated by eq (4). The term "standard deviation" is purposely avoided here since the properties of these deviations resulting from the iterated nonlinear fitting procedure are not known.

237-679 O-67—4

TABLE 3. *Observed earth temperature data of Lemont, Ill., by Carson*

Month	Depth (cm)						
	1	10	20	50	100	305	884
1	−0.4	−0.2	0.2	1.8	4.0	9.7	11.3
2	−0.2	−0.3	0.	1.2	3.0	8.3	11.3
3	4.0	3.3	3.0	2.9	3.5	7.3	11.4
4	8.1	7.1	6.8	6.3	6.0	7.2	
5	16.2	15.5	14.4	12.4	10.2	7.9	
6	22.4	22.5	21.3	18.7	15.5	9.7	
7	24.6	24.4	23.5	21.4	18.7	12.0	10.1
8	24.0	23.7	23.0	21.7	19.8	13.8	10.1
9	19.2	18.8	19.0	19.1	18.8	14.9	10.3
10	14.1	14.2	14.6	15.3	15.9	14.8	10.4
11	6.9	7.2	8.2	10.1	12.1	13.9	10.6
12	1.8	1.9	2.8	4.8	7.8	12.5	11.0
13	−0.6	−0.5	0.2	1.8	4.6	10.5	11.1
14	1.1	0.8	0.9	1.8	3.5	8.9	11.2
15	2.4	2.1	2.3	2.9	3.9	8.0	11.2
16	10.7	10.1	9.3	7.9	6.7	7.5	11.0
17	14.9	14.2	13.4	12.1	10.6	8.4	10.7
18	23.6	22.9	21.4	18.6	15.4	10.0	10.6
19	25.3	24.7	23.8	21.7	19.0	12.3	10.4
20	23.9	23.2	22.8	21.4	19.7	14.2	10.5
21	20.0	19.7	19.7	19.4	18.9	15.1	10.6
22	13.5	13.3	14.0	15.2	16.1	15.2	10.9
23	6.2	6.0	6.9	8.7	10.9	14.2	11.1
24	1.3	1.1	1.9	4.0	7.2	12.3	11.3
25	0.5	0.4	1.0	2.7	4.8	10.3	11.4
26	0.	−0.4	−0.1	1.2	3.4	9.0	11.5
27	2.9	2.1	2.1	2.6	3.6	7.8	11.5
28	11.3	11.0	10.2	8.6	7.1	7.4	11.1
29	16.7	16.5	15.7	13.9	11.8	8.7	11.0
30	20.6	20.1	19.3	17.4	15.0	10.4	10.7
31	26.7	26.0	24.7	21.8	18.7	12.3	10.5
32	25.5	25.1	24.4	22.9	20.7	14.2	10.5
33	19.5	19.2	19.3	19.3	19.0	15.3	10.7
34	13.3	13.1	13.6	14.7	15.7	15.3	10.8
35	4.5	4.3	5.2	7.7	10.6	14.0	11.0
36	−0.3	−0.4	0.4	2.7	5.8	12.1	11.4

Sample Calculations: The normal equations of tables 1 and 2 have been solved for annual earth temperature data of Lexington, Ky., and Lemont, Ill., which had been obtained by Penrod [1960] and Carson [1963], respectively. The Kentucky data covered five years, from 1952 through 1956, at six depths, 0, 61, 122, 183, 244, and 305 cm. Except for the data at 61 cm and 122 cm during July and August of 1953, the data are complete. Lemont data shown in table 3 are complete for the period of three years, from 1953 through 1955, at seven depths, 1, 10, 20, 50, 100, 305, and 884 cm, except at the depth of 884 cm during May, June, and July of 1953.

Figures 1 and 2 illustrate the trend of δ (table 2) and corresponding values of Δ calculated for several values of thermal diffusivities for the earth temperature data of Carson and Penrod, respectively. The calculations in figures 1 and 2 were carried out for $N=4$.

It is seen in figure 2 that the value of Δ, the RMSD of calculated temperatures from the observed data, decreases rapidly to the value of 1.07 °C as the assumed thermal diffusivity increases to a value at 0.005 cm²/sec. On the other hand it is seen from figure 2 that the diffusivity values that satisfy $\delta=0$ for the Lemont data is $\alpha=0.0058$ cm²/sec. Also it will be interesting to compare these thermal diffusivities with those calculated by conventional techniques by means of amplitude decay and phase angle shift by Penrod

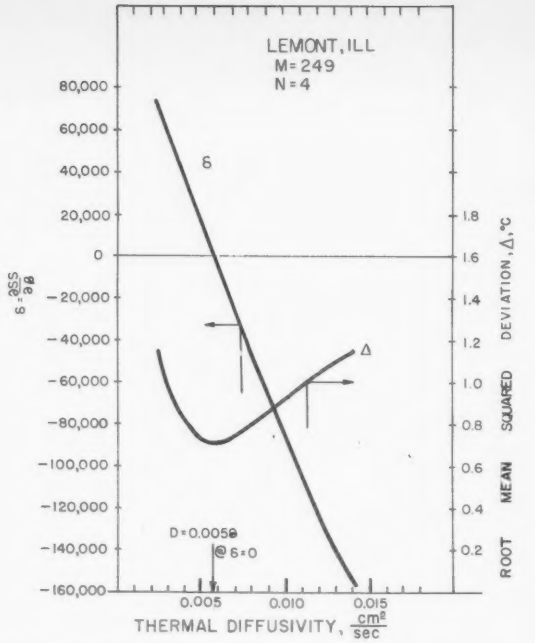

FIGURE 1. $\delta=\frac{\partial SS}{\partial \beta}$ *and* Δ *plotted against thermal diffusivity for earth temperature data of Lemont, Ill.*

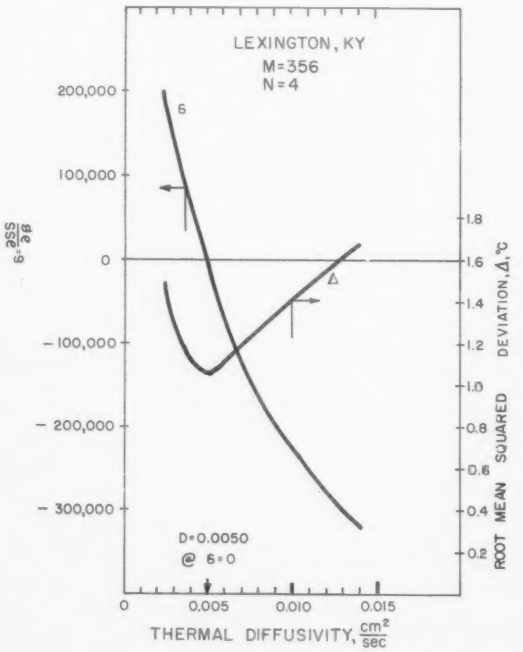

FIGURE 2. $\delta=\frac{\partial SS}{\partial \beta}$ *and* Δ *plotted against thermal diffusivity for earth temperature data of Lexington, Ky.*

from his Lexington data and with the data deduced from Carson's data for Lemont, Ill.

$$\text{Lexington data } \alpha_{B1} = 0.0088 \text{ cm}^2/\text{sec}$$

$$\alpha_{P1} = 0.0056 \text{ cm}^2/\text{sec}$$

$$\text{Lemont data } \alpha_{B1} = 0.0048 \text{ cm}^2/\text{sec}$$

$$\alpha_{P1} = 0.0045 \text{ cm}^2/\text{sec}.$$

Although the thermal diffusivities calculated by conventional amplitude and phase angle techniques differ from one another considerably, the values of Δ corresponding to their diffusivities are all less than 1.3 °C in their ranges, as seen in figures 1 and 2. (This small change of Δ with respect to a wide range of thermal diffusivity may be the very reason that the two methods can yield quite different thermal diffusivities.)

The mean squared deviation Δ^2 may not be as insensitive to the thermal diffusivity for the other types of periodic temperature data as it has been found to be in the analysis on annual cycles of monthly average earth temperatures.

The Lexington earth temperature data were used to examine the influence of including higher harmonic terms on the values of Δ and it was found that the least squares analysis, including the higher harmonic terms up to degrees 2, 4, and 8, do not yield values of Δ which are significantly different from the results of the analysis ignoring all of the higher harmonics for all the thermal diffusivities assumed.

Sample sets of least squares constants calculated for these two stations are shown in table 4.

TABLE 4. *Least squares constants for earth temperature data of Lexington, Ky., and of Lemont, Ill.*

	Lexington, Ky.	Lemont, Ill.
M	346	249
N	4	4
D	0.0050	0.0058
Δ	1.05	.72
A_0	14.48	11.39
A_1	−10.58	−10.63
A_2	−0.30	0.08
A_3	−.54	−.16
A_4	.24	−.30
B_1	−7.13	−7.97
B_2	−0.38	0.59
B_3	0.37	.21
B_4	.14	.39

It may be interesting to compare the calculated earth temperatures based upon the least squares constants with the original observed data. Table 5 shows the calculated earth temperatures when $N = 4$ is employed for formulas of table 1 on the observed data of Lemont, Ill. (table 3). Similar calculations such as those for table 4 for $N = 1$ were also made to evaluate the improvement of taking higher harmonics over using the simple harmonic expression for the annual cycle of Lemont data. According to such comparison changes in the calculated results due to the inclusion of higher harmonic terms are very small. Table 5 also may be compared with table 6, which is the arithmetic average (or norm) of the 3-year cyclic data of table 3. Significant discrepancy of the arithmetic average from the least squares result exists for the region near the surface.

TABLE 5. *Predicted earth temperatures for Lemont, Illinois, using least squares constants up to fourth harmonics*

Month	Depth (cm)						
	1	10	20	50	100	305	884
1	−0.5	−0.1	0.4	1.9	4.1	10.5	11.7
2	−0.3	−0.0	0.3	1.4	3.1	9.0	11.7
3	2.6	2.6	2.6	2.8	3.6	8.0	11.7
4	9.4	9.0	8.6	7.6	6.7	7.7	11.6
5	15.9	15.3	14.7	13.0	10.9	8.5	11.4
6	21.8	21.1	20.3	18.2	15.4	10.0	11.3
7	25.3	24.7	24.0	22.1	19.2	12.0	11.1
8	23.7	23.5	23.2	22.3	20.5	13.9	11.0
9	19.2	19.2	19.3	19.4	19.0	15.0	11.1
10	13.2	13.6	14.0	15.0	15.9	15.1	11.2
11	5.3	6.0	6.7	8.7	11.1	14.2	11.4
12	0.5	1.1	1.8	3.7	6.6	12.5	11.5

$M = 249$.
$N = 4$.
$D = .0058$.

TABLE 6. *Arithmetic average earth temperature of Lemont, Illinois, earth temperature data in table 3*

Month	Depth (cm)						
	1	10	20	50	100	305	884
1	−0.2	−0.1	0.5	2.1	4.4	6.8	11.3
2	.3	.0	.3	1.4	3.3	8.7	11.3
3	.9	3.1	2.5	2.8	3.7	7.1	11.4
4	10.0	9.4	8.8	8.7	6.6	7.4	11.1
5	15.9	15.4	14.5	12.8	10.9	8.3	10.8
6	22.2	21.8	20.7	18.3	15.3	10.0	10.7
7	25.5	25.1	24.0	21.6	18.8	12.2	10.3
8	24.4	24.0	23.4	22.0	20.1	14.1	10.4
9	19.6	19.2	19.3	19.3	18.9	16.1	10.6
10	13.6	13.6	14.1	15.1	15.9	15.1	10.7
11	5.9	5.8	6.8	8.8	11.2	14.1	10.9
12	0.9	0.9	1.7	3.8	6.9	12.3	11.2

Figure 3 compares the least squares calculation of the first harmonic constants with those derived from the observed three annual cycles of earth temperature in Lemont, Ill.

The coordinates a_x and b_x of the figure represent first harmonic constants describing the observed earth temperature at a depth x from the ground surface. Since the Lemont data consists of seven depth observations for a period of three years, each depth point is indicated with three numerals representing the first, second, and third year.

The solid curve was obtained by connecting a_x and b_x calculated by theoretical relation (depicted in the upper right corner of fig. 3) for several depths. The calculations of a_x and b_x were made with the least squares constants indicated in table 5. The curve representing the computed values of a_x and b_x fit extremely well for all of seven groups of three points. A similar comparison was made for the second harmonic constants of the same earth temperature data.

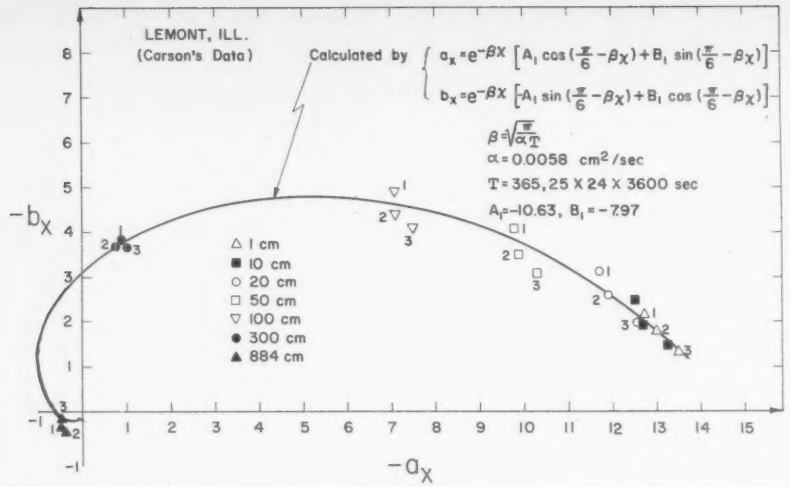
LEMONT, ILL.
(Carson's Data)
Calculated by
$a_x = e^{-\beta x}\left[A_1 \cos\left(\frac{\pi}{6} - \beta x\right) + B_1 \sin\left(\frac{\pi}{6} - \beta x\right)\right]$
$b_x = e^{-\beta x}\left[A_1 \sin\left(\frac{\pi}{6} - \beta x\right) + B_1 \cos\left(\frac{\pi}{6} - \beta x\right)\right]$
$\beta = \sqrt{\frac{\pi}{\alpha T}}$
$\alpha = 0.0058$ cm²/sec
$T = 365.25 \times 24 \times 3600$ sec
$A_1 = -10.63$, $B_1 = -7.97$
1 cm
10 cm
20 cm
50 cm
100 cm
300 cm
884 cm
$-b_x$
$-a_x$

FIGURE 3. *Graphical representation of harmonic constants for the earth temperature cycles of Lemont, Ill.*

Although the scatter of these second harmonic constants derived from observed data is much more than those indicated in figure 3, the computed curve did closely follow the centroid of the three points.

5. Conclusions

With the use of annual cyclic earth temperature data of Lexington, Ky., and of Lemont, Ill., a new technique is illustrated to yield single thermal diffusivity that will satisfy the least squares relation from the entirety of observed data. The technique requires an iterative solution of a nonlinear part of normal equations. The calculated earth temperatures based upon the theoretical heat conduction relation agrees very well with the average annual cyclic data of the monthly average earth temperatures when the least squares constants are properly evaluated.

It has also been found in this analysis that the deviation of the observed earth temperatures from the calculated temperatures is fairly insensitive to the thermal diffusivity as long as the thermal diffusivity is in the neighborhood of 0.005 cm²/sec, at least for the annual cycles of monthly average earth temperatures for two stations studied in this paper. This insensitivity may be the very reason that the current and existing techniques resulted in two quite different thermal diffusivities depending upon the method of calculation used, the amplitude method or the phase angle method.

The method developed in this paper is recommended as the preferred method for the determination of thermal diffusivity from the periodic data of depth temperatures, not only of the earth surface by of other celestial bodies as well, in the event such data becomes available.

This paper is a modification of a report prepared under the contracted research for the Office of Civil Defense. The permission from OCD to release the paper for publication is appreciated.

The author greatly appreciates much critical review given by A. McNish of the National Bureau of Standards.

6. References

Carson, J. E., Analysis of soil and air temperature by Fourier technique, J. Geophys. Res. **68**, No. 8, 2217–2232 (Apr. 15, 1963).

Eckert, E. R. G., and Drake, R. M., Heat and Mass Transfer (McGraw-Hill Book Co., Inc., New York, N.Y.); Toronto, Canada; London, England, 99–107, 1959.

Kusuda, T., and Achenbach, P. R., Earth temperature and thermal diffusivity at selected stations in the United States, Transactions of American Society of Heating, Refrigerating and Air Conditioning Engineers **71**, Pt. 1, 61–75 (1965).

Penrod, E. B., Variations of soil temperature at Lexington, Ky., from 1952 to 1956, Engineering Experiment Station Bulletin, University of Kentucky, No. 47 (Sept. 1960).

(Paper 71C1–442)

JOURNAL OF RESEARCH of the National Bureau of Standards—C. Engineering and Instrumentation
Vol. 71C, No. 1, January–March 1967

A New Near-Zone Electric-Field-Strength Meter*

Frank M. Greene**

Institute for Basic Standards, National Bureau of Standards, Boulder, Colo. 80302

(May 17, 1966)

The National Bureau of Standards has recently completed the development of prototype instrumentation for measuring the electric-field components of complex, high-level, near-zone electromagnetic fields. The instrumentation is intended for use in evaluating hazards of high-level electromagnetic radiation to electroexplosive ordnance devices at military installations. The measuring range is from 0.1 to 1000 V per meter, at frequencies from 150 kHz to 30 MHz, with a present uncertainty of less than ±2 dB.

The design of the NBS meters is based on the use of a novel form of telemetry, which apparently has not been fully exploited heretofore. This involves the use of a completely nonmetallic electrical transmission line over which the field information is transmitted from the measuring antenna to a remote readout unit. The line is essentially "transparent" to the field being measured, and reduces the perturbation of the field two orders of magnitude below that normally experienced when using a metallic line. The high r-f line loss involved necessitates miniaturizing the r-f portions of the receiving and calibrating instrumentation and placing them and their associated battery supplies *inside* the measuring antenna. The design and performance of the meters are discussed in some detail.

Key Words: Device, electroexplosive ordnance; field, near-zone electromagnetic; hazards, electromagnetic radiation; line, nonmetallic electrical transmission; line, semiconducting plastic transmission; meter, electric field-strength; telemetry, novel form of.

1. Introduction

The National Bureau of Standards, under the sponsorship of the Defense Atomic Support Agency, has recently completed the development of prototype instrumentation for measuring the electric-field components of complex, high-level, near-zone electromagnetic fields. The instrumentation is capable of measuring both the magnitude and direction of elliptically polarized CW electric fields having strengths in the range from 0.1 to 1000 V per meter at frequencies from 150 kHz to 30 MHz. This represents one step in the effort to develop accurate and meaningful measuring and calibrating instrumentation, for use in evaluating hazards of electromagnetic radiation to electroexplosive ordnance devices. It is well known that high-level fields of powerful nearby radio transmitters may cause premature detonation of missile and rocket type weapons during storage or loading operations on shipboard, or at other military installations. It was from the standpoint of improving both the weapons reliability, as well as the safety of operating personnel and equipment, that the program was undertaken.

The design of the NBS meters is based on the use of a novel form of telemetry, employing a completely nonmetallic electrical transmission line to avoid perturbing the field being measured. This approach has apparently not been fully exploited, heretofore. The extremely high r-f loss of the line used attenuates any r-f currents induced on the line by the surrounding field and essentially eliminates reradiation from the line, or unwanted coupling between the line and the measuring antenna. The high line-loss, however, necessitates miniaturizing the r-f portions of the receiving and calibrating instrumentation and placing them and the associated battery supplies *inside* the measuring antenna. The field information contained in the detected DC-AF output of the receiver is transmitted over the line to a remote readout unit, where the strength of the electric-field component parallel to the axis of the antenna is read directly.

Interim electric-field standards and calibration techniques were also develped at NBS to evaluate the performance of the field-strength meters during their development, as well as to provide a tentative calibration of the completed instruments. The present uncertainty of the standards is believed to be less than ±2 dB, but further development effort is expected to reduce this to less than ±1 dB.

2. The New "Semiconducting" Plastic Transmission Line

2.1. Errors Caused by Metallic Lines

In the past, electric field-strength meters have usually made use of a long *metallic* r-f transmission

*For complete design details the reader is referred to "A New Near-Zone Electric-Field-Strength Meter"—Frank M. Greene, National Bureau of Standards Technical Note No. 345, November 15, 1966. For sale by the Superintendent of Documents, U.S. Government Printing Office, Washington, D.C. 20402. Price 35 cents.

**Radio Standards Engineering Division, National Bureau of Standards, Boulder, Colo. 80302.

line to connect the measuring antenna with its receiver, usually located at a point remote from the antenna. Such metallic lines often cause large measurement errors, especially when measuring near-zone fields having complex spatial distributions. In these cases, a neutral-field path, along which the line can be placed, either seldom exists, or the orientation of such a path, if it *does* exist is usually not known in advance of making the measurements. Under these conditions, it is difficult or impossible to orient the line so that it is everywhere normal to existing electric-field components. Thus, the line not only may perturb the field being measured, but unwanted r-f currents induced on the line can be coupled into the antenna and contribute to the total response of the field-strength meter.

2.2. The Use of a Nonmetallic Line

The NBS near-zone meters avoid this difficulty by making use of a special nonmetallic balanced transmission line in which the conductor r-f loss has been purposely made extremely high compared to that of the usual copper line. If the conductors are made of sufficiently high resistance material, the line can be made essentially "transparent" to the surrounding field. This is to say that the r-f currents induced on the transmission line by the field will be negligibly small, resulting in insignificant reradiation, or that any r-f energy propagating along the line will be heavily attenuated because of the extremely high loss of the line. It has been found that this can be achieved if the volume resistivity of the conductor material used is of the order of a million times or more higher than that of copper. This is roughly midway (on a logarithmic scale) between the volume resistivity of metals, on the one hand, and that of insulators such as glass or mica on the other. Such materials can therefore be said to be "semiconducting."

2.3. Description of the "Semiconducting" Line

The material used in the NBS lines is basically polytetrafluoroethylene (PTFE), rendered "semiconducting" by uniformly dispersing finely divided carbon black (approximately 30 percent by weight) throughout the plastic while it is in the semifluid state during its manufacture. Tests at NBS have indicated the PTFE material to be more stable electrically than other types tried, such as silicone rubber, polyethylene, carbon-coated multifiber glass, etc. Other types of conductor materials (including high-resistance metallic alloy wire and thin deposited metallic films) were examined, but were not found to be practical for this use, either because of unsuitable electrical characteristics or excessive cost.

Several parallel-conductor balanced transmission lines were made at NBS using the semiconducting PTFE material. The line conductors are in the form of 0.03 in diam monofilaments in place of the usual copper conductors. They are coated with a thin nylon film (approximately 0.005 in thick) to further improve their strength and electrical stability. Each of the filaments is in turn enclosed in a vinyl-coated woven fiber glass sleeve approximately 0.1 in O.D. Two such insulated conductors are encased in a polyvinyl chloride outer jacket, for added strength and protection, to form the completed transmission line. Military Type JJ–048 or PJ–291 twin-conductor plugs are used at the two ends for connecting to the dipole antenna, and to the remote indicator unit, respectively. The overall length of the lines is approximately 30 ft.

2.4. Electrical Characteristics of the Line

The semiconducting PTFE material used in the line has a volume resistivity of approximately 3.0 Ω-cm (compared to 1.7×10^{-6} Ω-cm for copper), giving a resistance of approximately 20,000 Ω per lineal foot, or a loop resistance of approximately 1.2 MΩ for a line 30 ft in length. The measured mutual capacitance between the two line conductors is approximately 10 pF per foot, or roughly 300 pF for the entire line. The transmission loss, to the desired field-strength information at dc and low af, is negligible if a high-impedance d-c a-f vacuum-tube voltmeter is used as the readout device at the receiving end of the line. The line attenuation increases as the square-root of frequency, reaching a theoretical as well as a measured value of approximately 53 dB per foot at a frequency of 30 MHz, for the differential mode of transmission. The common-mode attenuation with the line lying flat on a metal ground plane turns out to have essentially the same value. The use of a high-loss, parallel-conductor, balanced transmission line of this type has been found to reduce the perturbation of the surrounding field by more than *two* orders of magnitude below that existing in the case of a copper line. This renders any effect of the line on the field wholly negligible in most instances. A type of "flexural" noise is generated on the transmission line when it is suddenly flexed or moved physically. The common-mode component of this "noise" may be relatively high, having a peak value of several volts on open circuit. However, the differential-mode component is appreciably smaller and does not present a problem in the NBS meters at the level of d-c transmission used (see table 1).

3. Description of the Near-Zone Field-Strength Meters

3.1. Principles of Operation

Two prototype near-zone field-strength meters were developed for the Defense Atomic Support Agency, and cover the frequency ranges 150 to 250 kHz, and 18 to 30 MHz, respectively. These meters make use of a tuned r-f type of receiver to amplify the voltage induced in the receiving antenna by the component of

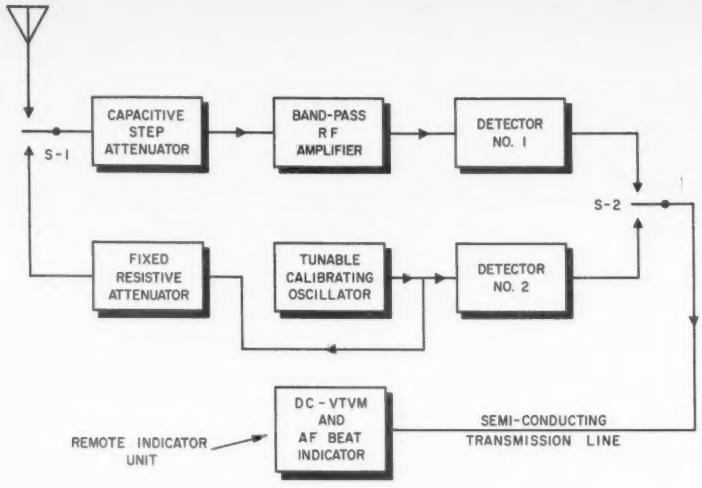

FIGURE 1. *Block diagram of the NBS field-strength meter.*

the electric field being measured. A tunable CW oscillator is included to permit calibrating the overall receiver gain periodically during a sequence of measurements in the field. A block diagram of the basic circuitry is shown in figure 1. The meters employ the same basic method of receiver-gain calibration that has been used in CW-type field-strength meters in this country for many years. The receiver portion of the field-strength meter consists basically of an r-f input capacitive step attenuator, a fixed-tuned band-pass r-f amplifier (with manual gain control), and a diode detector. The r-f output level of the oscillator is monitored by its own detector. When calibrating, the receiver gain is simply adjusted until the d-c outputs of the two detectors are identical. In this method, the exact level of the calibrating signal is not important, and does not have to be known. However, it *is* important that the oscillator monitoring detector remain stable.

TABLE 1. *Distribution of nominal operating rf-voltage levels (in the TRF field-strength meter)*

E(V/m)	α(dB)	V_i(volts)	V_0(volts)	V_1(volts)	V_2(volts)	V_3(volts)
0.1–1.0	0	0.015–0.15	0.003–0.03	0.003–0.03	0.3–3.0	0.75–7.5
1.0–10	20	0.15–1.50	0.03–0.30	0.003–0.03	0.3–3.0	0.75–7.5
10.–10^2	40	1.50–15.0	0.30–3.00	0.003–0.03	0.3–3.0	0.75–7.5
10^2–10^3	60	15.0–150.	3.00–30.0	0.003–0.03	0.3–3.0	0.75–7.5

E(V/m) = Electric field strength, volts per meter
α(dB) = Measuring dipole attenuator setting
V_i = Induced voltage in measuring dipole
V_0 = Output voltage of measuring dipole
V_1 = Input voltage to rf amplifier
V_2 = Output voltage of rf amplifier
V_3 = Output voltage of amplifier detector (DC).

A list of the various ranges of r-f voltage over which the principal components operate is shown in table 1 for the range of electric field strength from 0.1 to 1000 V per meter. An explanation of how the ranges were calculated is given in the following:

Effective length of measuring dipole..., $L_{eff} \cong 0.15$ m
Induced voltage in dipole....., $V_i = E \cdot L_{eff}$
Dipole voltage-transfer ratio, $V_0/V_i = C_a/(C_a+C_s) \cong 0.20$
$C_a \equiv$ Internal capacitance of dipole....., $C_a \cong 3$ pF
$C_s \equiv$ Residual gap and circuit capacitance, $C_s \cong 12$ pF
RF amplifier nominal voltage gain....., $V_2/V_1 \cong 100$.

3.2. Electrical Design

The Dipole Antenna. A cutaway view of the dipole assembly is shown in figure 2, and a view of an assembled unit is shown in figure 3. The dipole is made of 1/16 in wall copper tubing 1 3/8 in O.D. The length is approximately 13 in with a 1/32 in insulated gap at the center. The miniaturized solid-state receiver and its battery supply are contained in the left half, and the CW calibrating oscillator and its battery supply are in the right half. The capacitive step attenuator, the DPDT line-transfer switch, and the oscillator ON-OFF control comprise the five rotary switch wafers seen in the central portion of the dipole assembly. The balanced transmission-line plug connects to two insulated stainless steel pins at the center of the dipole. The line enters the interior of the dipole through a two-section balanced RC filter to help preserve the electrical symmetry or balance of the dipole with respect to the transmission line, and to attenuate any differential, as well as common-mode r-f pickup that might exist on the line. The symmetry is important if the antenna is to respond only to the component of the electric field parallel to its axis. The symmetry of the NBS dipole is such that its response to the cross-polarized component of the electric field is 40 dB or more below the principal response.

It can be shown that if the length of the measuring dipole does not exceed 0.03 wavelength, its effective

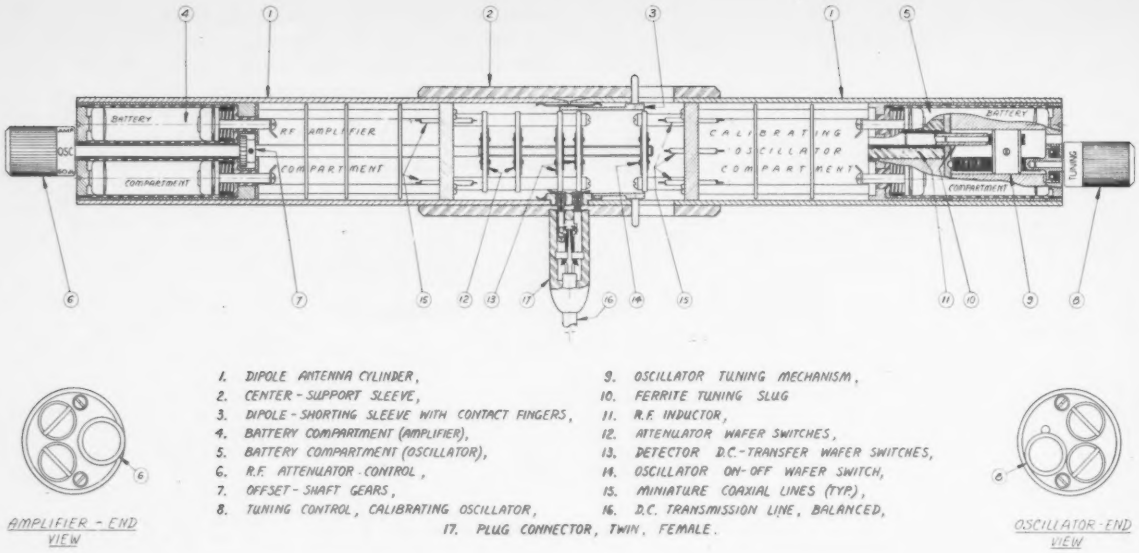

FIGURE 2. *Cutaway drawing of the measuring dipole.*

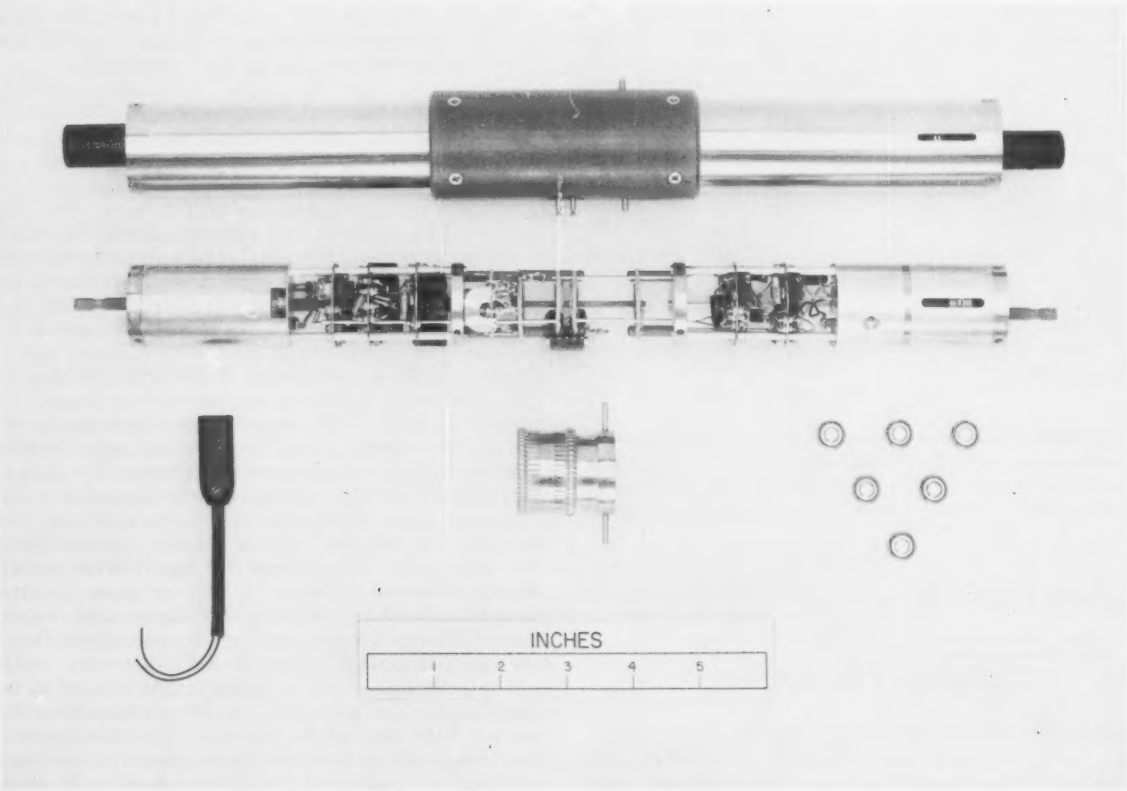

FIGURE 3. *View of the complete measuring dipole.*

length when measuring a field having a highly complex spatial distribution will not differ by more than 2 or 3 percent (in the worst case) from the effective length when immersed in a uniform plane wave. Likewise, the interaction error, resulting from coupling between such a short antenna and its image, will be small provided the loading is light and that measurements are not made closer than 2 or 3 ft to the ground or large metallic objects.

RF Capacitive Step Attenuator. This attenuator has four principal steps, 0, 20, 40, and 60 dB, with two additional 0 dB positions, calibrate A(OSC) and calibrate B(AMP). In the latter two positions, the calibrating oscillator is automatically turned ON, and the "semiconducting" transmission line can then be switched between the d-c outputs of the oscillator and amplifier detectors, while calibrating the amplifier gain. The attenuator is constructed using special subminiature rotary wafer switches. Miniature low-temperature coefficient ceramic capacitors are used in either an "L" or a "Pi" configuration for the various attenuator pads. The attenuator steps are accurate to ± 0.1 dB. The attenuator module is approximately 1 in O.D. by 1 in long.

Band-Pass Amplifier and Detector. In order to provide a high input impedance, so as not to appreciably load the dipole antenna or the capacitive step attenuator, a metal-oxide-silicon field-effect transistor (MOS–FET) is used in the first stage as an untuned input-impedance converter. This is followed by a six-pole, fixed-tuned, bandpass filter having a 3 dB pass-band of 150 to 250 kHz, and 18 to 30 MHz respectively in the two units and a 40 dB pass-band of 100 to 300 kHz and 12 to 36 MHz, respectively. The filter is followed by a 3-stage r-f amplifier. In the low-frequency unit, this is broadband resistance-coupled, using overall negative r-f feedback to improve gain stability with respect to temperature and supply-voltage variations. In the high-frequency unit, the r-f amplifier has 3 stages using wide-band synchronously tuned interstage transformers. The overall gain of both amplifiers can be manually adjusted to the required operating value of approximately 40 dB. The output detectors of both amplifiers employ two stable silicon diodes in a voltage-doubling circuit, to ease voltage-swing requirements on the final stage and consequently to reduce battery drain. A 12 V silver-oxide battery supply is used, having a useful life of from 10 to 20 hr. The complete amplifier module measures 1¼ in O.D. by 5 in long including its filter and battery supply.

Calibrating Oscillator and Detector. This unit is also transistorized. It consists of a permeability-tuned Clapp-Colpitts oscillator followed by a two-stage automatic-level-control amplifier to maintain the r-f output essentially constant over its tuning range. The tuning range of each of the two oscillators is the same as the 3 dB bandwidth of the band-pass amplifier with which it is used. The r-f output of the oscillator is adjustable to roughly 3.0 V and fed into a fixed 30 dB resistive attenuator pad. When calibrating the gain of the band-pass amplifier, the output of approximately 0.1 V from the pad is applied to the amplifier input through a small variable capacitor (adjusted to approximately 3 pF) which simulates the dipole probe capacitance. The detector circuit is identical to that used with the band-pass amplifiers and is used to monitor the 3.0 V oscillator level at the input terminals of the 30 dB pad. A 13.5 V silver-oxide battery supply is used, having a useful life of about 20 hr. A portion of the supply is Zener regulated and applied to the transistor base circuits for improved amplitude stability. The complete calibrating oscillator module measures 1¼ in O.D. by 5 in long including the battery supply.

The Remote Indicator Unit. This unit consists basically of a battery-operated, balanced d-c vacuum-tube voltmeter, with its d-c microammeter, on which the magnitude of the electric field strength is indicated. This VTVM has exceptionally good stability and linearity of response because of the large amount of negative d-c feedback employed in its design. It is used over a single 20 dB input range of approximately 0.75 to 7.5 V. The balanced input circuitry provides from 40 to 60 dB rejection of common mode input in the 60 to 400 Hz power-frequency range. In addition, a two-section balanced r-f filter provides at least 40 dB suppression of common and differential-mode input at the higher r-f frequencies. An output circuit in the VTVM is used to drive a transistorized audio amplifier and loud speaker. These units are used as a zero-beat indicator when adjusting the frequency of the calibrating oscillator to that of the field being measured. Separate, self-contained battery supplies are used with the VTVM and a-f amplifier. The complete remote indicator is housed in a drawn-aluminum case, using a tight-fitting panel to minimize r-f leakage into the unit. A small drawn-aluminum case is used to enclose the rear side of the d-c microammeter to reduce r-f entry through the meter face.

The Assembled Field-Strength Meter. The measuring dipole of the near-zone field-strength meter is mounted on a hollow fiber-glass shaft which is perpendicular to its axis. This shaft is in turn supported in plastic bearings in a circular reinforced polyfoam gimbal, approximately 21 in. in diameter, as shown in figure 4. This assembly is mounted on a sturdy wooden surveyor's tripod, in such a manner that manual adjustments in both azimuth and elevation can be readily made in the orientation of the dipole. A view of the complete field-strength meter is shown in figure 5. The balanced transmission line connects to the dipole through the hollow shaft on the right. The other end of the 30 ft line connects to the remote indicator unit, a closeup view of which is shown in figure 6.

3.3. Performance

The two near-zone field-strength meters underwent extensive field tests at the U.S. Naval Weapons Laboratory at Dahlgren, Va. Electric field strengths were

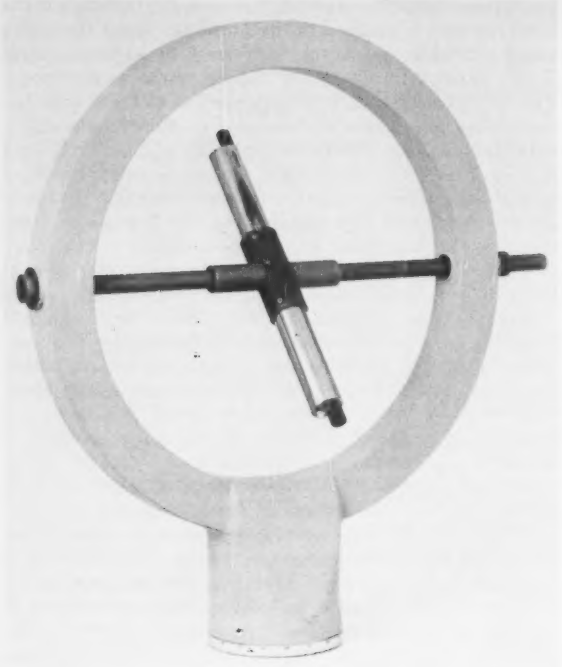

FIGURE 4. *View of the measuring dipole and mounting gimbal.*

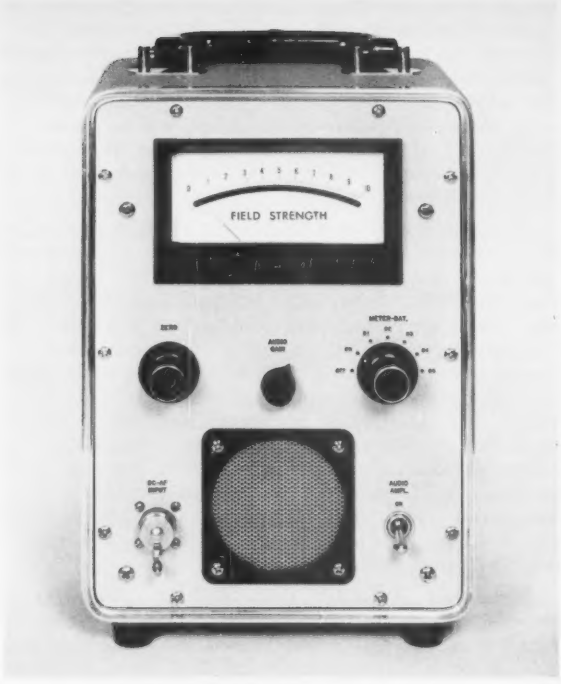

FIGURE 6. *View of the remote indicator unit.*

FIGURE 5. *The complete near-zone field-strength meter.*

measured without difficulty over the entire range from 0.1 to 1000 V per meter (CW-RMS). There was no observable susceptibility to out-of-band CW signals having levels as high as 200 V per meter, or to pulsed signals from nearby high-powered radar transmitters. No interaction was observed between the semiconducting transmission line and the field being measured. In general, the agreement was about ± 1 dB between the instrument readings as calibrated in the NBS standard field at Boulder and those obtained in the NWL standard field at Dahlgren. The uncertainty in the calibration accuracy of the instruments is believed to be less than ± 2 dB. Further development effort on the standard fields is expected to reduce this to less than ± 1 dB.

The work described in this paper was performed for the Field Command, Defense Atomic Support Agency, under DASA Order No. HD-1102-3171-0001 (June 20, 1963).

The author wishes to acknowledge the valuable assistance of William E. Jessen of NBS-BL in the assembly and performance evaluation of the instrumentation described herein. The assistance of Ezra B. Larsen in the standard-field development work is also gratefully acknowledged.

4. Bibliography

[1] Stoker, W. C., et al., An investigation of electromagnetic coupling devices for the measurement of noise fields, Final Report, Rensselaer Polytechnic Institute, Troy, N.Y., Signal Corps Contract No. DA 36-039 sc-207 (Sept. 1952).

[2] Abromavage, M. M., et al., Electromagnetic coupling to ordnance systems, Report No. N178-7604, August 1961, Jansky & Bailey Div., Atlantic Research Corp., Alexandria, Va.

[3] Bartfeld, R. A., et al., Study of methods of improved measurement for electromagnetic field components, Final Report, 26 May 1960 to 30 June 1962, University of Pennsylvania, Philadelphia, Pa., USNCEL Contract NBy-3200.

[4] Cowles, W. W., et al., Study of methods of implementing Poynting-vector measurements, Final Report 1 July 1962 to 31 December 1964, University of Pennsylvania, Philadelphia, Pa., USNCEL Contract NBy-32219.

[5] Harrison, R. P., and Lewis, E. A., A method for accurately measuring the vertical electric field strength of a propagating VLF wave, IEEE Trans. on I&M, **IM-14**, P1/2, pp. 89-97 (Mar.-June 1965).

[6] Clark, D. B., et al., Electromagnetic field-strength measurements in a quasi-absolute monopole field, Final Report August 1963 to October 1964, TR-R-361, U.S. Naval Civil Engineering Lab., Port Hueneme, Calif. (Mar. 1965).

[7] Cowdell, R. B., HERO ground-plane measurements and development of the near-field field-intensity meter, Final Report No. 2667-7191, 30 April 1965, and Addendum No. 1, July 1965, Genistron, Incorporated, College Park, Md.

(Paper 71C1-443)

JOURNAL OF RESEARCH of the National Bureau of Standards—C. Engineering and Instrumentation
Vol. 71C, No. 1, January–March 1967

Inductance and Characteristic Impedance of a Strip-Transmission Line

R. L. Brooke,* C. A. Hoer,* and C. H. Love*

Institute for Basic Standards, National Bureau of Standards, Boulder, Colo. 80302

(October 25, 1966)

A general method is developed for determining the inductance and characteristic impedance of uniform transmission lines. A non-uniform current distribution is allowed in the transverse plane. The system is represented by a matrix equation which can be programmed for computer solution. The correct inductance and impedance are obtained as the result of a simple limiting process. The method is applied to one particular geometry, a four-tape stripline system. Results are given for the inductance, resistance, and current distribution as functions of frequency and resistivity for a particular geometry. A method for extending the results to strip lines with proportional dimensions is developed. An accuracy of one part in 10^5 was found to be feasible for the determination of the inductance per unit length.

Key Words: Characteristic impedance, inductance, and strip-transmission lines.

1. Introduction

The determination of the inductance, capacitance, or characteristic impedance of coaxial systems has been the subject of numerous reports. The system considered here is the special case of a strip-transmission line consisting of four vanishingly thin parallel tapes.

The approach used in this paper is to determine the current distribution in a transverse plane and therefore the transverse magnetic field configuration. Knowing the current distribution, the effective inductance per unit length is found directly. The characteristic impedance of a lossless line can then be determined from the inductance.

Almost all previous authors have used the approach of calculating the capacitance per unit length, C, after determining the configuration of the transverse electric field. The result is then used to calculate the characteristic impedance of the lossless line, using the relationship

$$Z_0 = 1/vC \tag{1}$$

where v is the velocity of propagation in the line. Several applications of this approach are listed in the references [1–4].[1] The results of Cohn [2] and Bates [3] give analytic results which are useful design tools.

The approach used in this paper, while nonanalytic, is quite general and without any geometric limitation in the transverse plane. The effect of finite conductor losses and frequency dependence can also be included. It is not necessary to assume any distribution or magnitude for the interdependent variables as this approach determines all necessary information simultaneously.

2. Consideration of Finite Losses

If the line has finite losses, the characteristic impedance and propagation constant, γ, can be calculated from

$$Z_0 = \sqrt{\frac{R+j\omega L}{G+j\omega C}} \tag{2a}$$

$$\gamma \equiv \alpha + j\beta = \sqrt{(R+j\omega L)(G+j\omega C)} \tag{2b}$$

where R and G are the series resistance and shunt conductance per unit length of the line and α and β are the attenuation and phase constant of the line. For a low-loss line, (2a) and (2b) can be closely approximated by

$$Z_0 = vL\left[1 + j\left(\frac{1}{2Q_c} - \frac{1}{2Q_L}\right)\right] \tag{3a}$$

$$\alpha = \frac{R}{2vL} + \frac{GvL}{2} \tag{3b}$$

$$\beta = \omega\sqrt{LC} = \frac{\omega}{v} \tag{3c}$$

* Microwave Circuits Standards, Radio Standards Engineering, NBS Laboratories, Boulder, Colo. 80302.

[1] Figures in brackets indicate the literature references at the end of this paper.

where $Q_L \equiv \omega L/R$ and $Q_c \equiv \omega C/G$. Terms involving Q^2 have been neglected. It is also assumed that

$$\frac{\sigma_c}{\omega \epsilon_c} \gg 1, \text{ and } \frac{R_s}{\eta} \ll 1$$

which must be satisfied for transmission line theory to be valid [5] where σ_c and ϵ_c are the conductivity and dielectric constant of the conductor, R_s is the skin-effect surface resistivity of the conductor, and η is the intrinsic impedance of the dielectric.

Both R and L are functions of frequency and resistivity as well as geometry for lines with finite loss. The inductance is therefore a function of resistance so that R must also be calculated to obtain accurate values of L. A computer method for calculating R and L as a function of frequency, resistivity, and geometry is developed in this paper. Values of v and G are readily obtained from properties of the dielectric material in the line. These values together with R and L can be used to obtain the attenuation constant from (3b). If the contribution of Q_L and Q_c in (3a) can be ignored, the characteristic impedance can be obtained from the simple relationship

$$Z_0 = vL.$$

which is analogous to (1).

3. D-C Inductance

Figure 1 shows the cross section of a four-tape stripline. The conductors marked 1 and 2 are to act as a single outer conductor while conductors 3 and 4 act as a single inner conductor in a go-and-return circuit. For conductors with finite resistance the current will be uniformly distributed throughout the outer and inner conductors at zero frequency. The total inductance of the system, $\mathscr{L}$, can be calculated from

$$\mathscr{L} = \frac{1}{4} \sum_{i=1}^{4} \sum_{j=1}^{4} M_{ij} \tag{4}$$

where M_{ij} is the mutual inductance between tape i and j, and M_{ii} is the self inductance of tape i. A recent report by Hoer and Love [6] gives exact equations for the inductances of rectangular conductors carrying a uniform current. Using these equations to calculate the M_{ij}, the exact d-c inductance of any rectangular coaxial system can be obtained.

4. A-C Resistance and Inductance

When an alternating voltage is applied to the system, the current is no longer uniformly distributed throughout the cross section of the conductors. The inductance as well as resistance then differs from the d-c values.

Consider a short length of a long uniform line, such as shown in figure 2. Writing V_2 in terms of V_1 gives

$$V_2 = V_1 \cosh \gamma \Delta l - I_1 Z_0 \sinh \gamma \Delta l. \tag{5}$$

Choose Δl such that $|\gamma \Delta l| \ll |$. Then (5) can be approximated by

$$V_2 = V_1 - I_1 Z_0 \gamma \Delta l$$

or

$$\frac{V_1 - V_2}{\Delta l} = I Z_0 \gamma. \tag{6}$$

Substituting (1) and (2) into (5) gives

$$\frac{\Delta V}{\Delta l} \equiv \frac{V_1 - V_2}{\Delta l} = I(R + j\omega L). \tag{7}$$

Our object now will be to calculate the total current, I, for some arbitrary value of $\Delta V/\Delta l$ and from this result obtain R and L from (7). With R and L known, the transmission line constants may be obtained from (3).

To determine the total current in the stripline, each tape is mathematically divided into a number of smaller, parallel sections as shown in figure 3. An equivalent circuit of the transmission line then looks

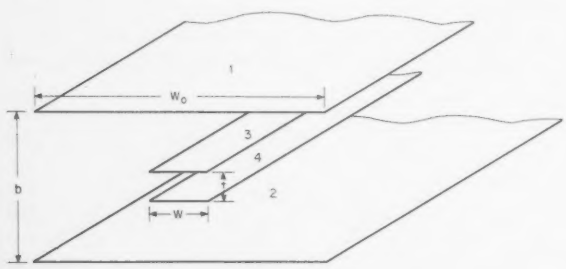

FIGURE 1. *Cross section of a four-tape stripline.*

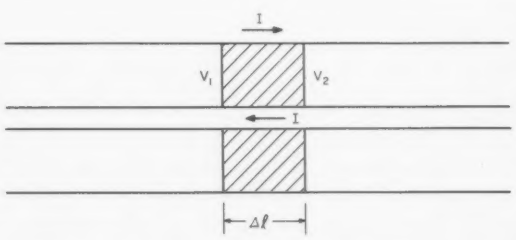

FIGURE 2. *Short length of a long uniform transmission line.*

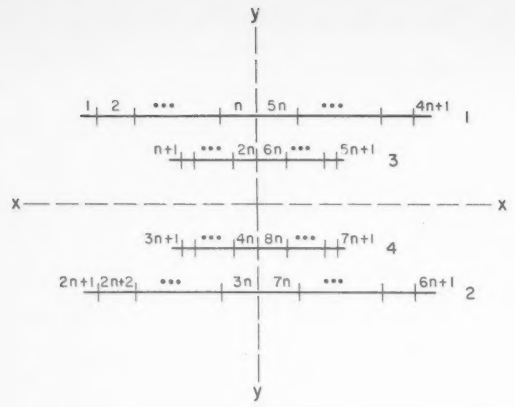

FIGURE 3. *Cross section of the stripline showing how the sections are labeled.*

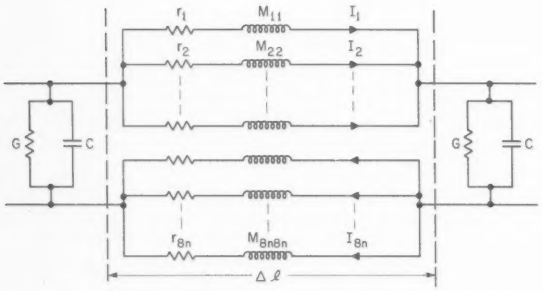

FIGURE 4. *Equivalent circuit for the stripline with the tapes divided into small parallel sections.*

like that in figure 4. The width of each section is chosen small enough so that the current density may be considered uniform throughout that section. The appendix contains dc inductance equations which can be used to calculate the self, and the mutual inductance per unit length of these sections. The resistance per unit length of each section will be the dc resistance.

Although the method of subdivision is almost completely arbitrary, one system will be explained, which, although strange in appearance, will simplify later expressions considerably. Each tape is divided into $2n$ sections labeled in such a way that the index increases as the y axis is approached from any edge as shown in figure 3. The widths of the sections need not be equal and indeed will not be in later calculations. Since the geometry has symmetry about the origin and both axes, this symmetry is retained in subdividing the tapes. Symmetry produces the following relations between the currents in the different sections. For the outer tapes,

$$I_j = I_{2n+j} = I_{4n+j} = I_{6n+j}, \quad j = 1, 2, \ldots, n.$$

For the inner tapes,

$$I_{n+j} = I_{3n+j} = I_{5n+j} = I_{7n+j}, \quad j = 1, 2, \ldots, n.$$

The total voltage drop per unit length along the length of any one section may be written,

$$V_k = r_k I_k + j\omega \sum_{l=1}^{8n} M_{kl} I_l. \tag{8}$$

For the purposes of this report the d-c resistance per unit length, r_k, of each section will be used in the form of resistivity/area. There are $8n$ equations which may be written in matrix form as

$$\begin{pmatrix} V_1 \\ \cdot \\ \cdot \\ \cdot \\ V_{8n} \end{pmatrix} = \left[\begin{pmatrix} r_1 & & 0 \\ & \cdot & \\ & & \cdot \\ 0 & & r_{8n} \end{pmatrix} + j\omega \begin{pmatrix} M_{1,1} & \cdots & M_{1,8n} \\ \cdot & & \cdot \\ \cdot & & \cdot \\ M_{8n,1} & \cdots & M_{8n,8n} \end{pmatrix} \right] \begin{pmatrix} I_1 \\ \cdot \\ \cdot \\ \cdot \\ I_{8n} \end{pmatrix} \tag{9}$$

As a result of the current symmetry conditions, only $2n$ of the equations are independent. The four groups $k = 1$ to $2n$, $2n+1$ to $4n$, $4n+1$ to $6n$, and $6n+1$ to $8n$ are all equivalent.

Choosing the first group, with $k = 1$ to $2n$ as the $2n$ independent equations to be solved, rewrite (9) as

$$\begin{pmatrix} V_1 \\ \cdot \\ \cdot \\ \cdot \\ V_{2n} \end{pmatrix} = \left[\begin{pmatrix} r_1 & & 0 \\ & \cdot & \\ & & \cdot \\ 0 & & r_{2n} \end{pmatrix} + j\omega \begin{pmatrix} \mathcal{M}_{1,1} & \cdots & \mathcal{M}_{1,2n} \\ \cdot & & \cdot \\ \cdot & & \cdot \\ \mathcal{M}_{2n,1} & \cdots & \mathcal{M}_{2n,2n} \end{pmatrix} \right] \begin{pmatrix} I_1 \\ \\ \\ I_{2n} \end{pmatrix} \tag{10}$$

where

$$\mathcal{M}_{ij} = \sum_{p=0}^{3} M_{i,2pn+j}, \qquad i, j = 1, 2, \ldots 2n.$$

Equation (10) can now be written in the form

$$V = [R + j\omega \mathcal{M}] I. \tag{11}$$

Since V_k and I_k from (8) are complex, let

$$V_k = e_k + jf_k, \qquad I_k = a_k - jb_k. \tag{12}$$

In terms of column matrices,

$$V=E+jF, \qquad I=A-jB. \tag{13}$$

Substituting (13) into (11) produces two real matrix equations:

$$E=RA+\omega\mathcal{M}B, \tag{14}$$

$$F=-RB+\omega\mathcal{M}A. \tag{15}$$

Solving for A and B produces

$$A=R^{-1}[(1)+(\omega\mathcal{M}R^{-1})^2]^{-1}[E+(\omega\mathcal{M}R^{-1})F] \tag{16}$$

$$B=R^{-1}[(1)+(\omega\mathcal{M}R^{-1})^2]^{-1}[(\omega\mathcal{M}R^{-1})E-F]. \tag{17}$$

In these equations for A and B, E and F have not yet been determined. To simplify their determination the following matrix definitions are used:

$$\psi=R^{-1}[(1)+(\omega\mathcal{M}R^{-1})^2]^{-1}$$

$$\phi=\omega\mathcal{M}R^{-1}$$

$$\tau=(1_1, \ldots, 1_n, -1_{n+1}, \ldots, -1_{2n})$$

$$\theta=(0_1, \ldots, 0_n, 1_{n+1}, \ldots, 1_{2n}) \tag{18}$$

Since the total current in the outer conductor must equal the total current in the inner conductor, we have

$$\sum_{k=1}^{n} a_k-\sum_{k=n+1}^{2n} a_k\equiv 0$$

$$\sum_{k=1}^{n} b_k-\sum_{k=n+1}^{2n} b_k\equiv 0$$

or in matrix notation, using (16) and the definitions in (18)

$$\tau A=\tau\psi[E+\phi F]\equiv 0 \tag{19}$$

$$\tau B=\tau\psi[\phi E-F]\equiv 0. \tag{20}$$

The scalar voltage drops in the inner sections and outer sections obey the following conditions:

$$\left.\begin{matrix} f_1=f_k \\ e_1=e_k \end{matrix}\right\} k=1, 2, \ldots, n$$

$$\left.\begin{matrix} f_{n+1}=f_l \\ e_{n+1}=e_l \end{matrix}\right\} l=n+1, n+2, \ldots 2n$$

$$e_1+e_{n+1}+j(f_1+f_{n+1})=\Delta v/\Delta l.$$

Since the value of $\Delta v/\Delta l$ is arbitrary, it is set equal to $1+j0$. This condition applied to the above results produces

$$e_1+e_{n+1}=1$$

$$f_1+f_{n+1}=0.$$

The column matrices E and F can now be written in terms of known matrices and one scalar unknown each:

$$\begin{aligned} E&=\theta^T+e_1\tau^T \\ F&=f_1\tau^T \end{aligned} \tag{21}$$

where the superscript T indicates the transposed matrix. Substituting (21) into (19) and (20) and solving for e_1 and f_1 produces

$$e_1=-\frac{(\tau\psi\phi\tau^T)(\tau\psi\phi\theta^T)+(\tau\psi\theta^T)(\tau\psi\tau^T)}{(\tau\psi\tau^T)^2+(\tau\psi\phi\tau^T)^2} \tag{22}$$

and

$$f_1=\frac{(\tau\psi\phi\theta^T)(\tau\psi\tau^T)-(\tau\psi\theta^T)(\tau\psi\phi\tau^T)}{(\tau\psi\tau^T)^2+(\tau\psi\phi\tau^T)^2} \tag{23}$$

Every term in parenthesis on the right sides of these equations is a calculable scalar. The result obtained can be substituted into (16) and (17) and the current in each section can be determined. With the currents known, the approximate inductance and resistance per unit length can be calculated from (7), which in terms of the components of the current in each section becomes

$$L_{\text{eff}}=\frac{\frac{1}{4\omega}\sum_{k=1}^{n} b_k}{\left(\sum_{k=1}^{n} a_k\right)^2+\left(\sum_{k=1}^{n} b_k\right)^2} \tag{24}$$

and

$$R_{\text{eff}}=\frac{\frac{1}{4}\sum_{k=1}^{n} a_k}{\left(\sum_{k=1}^{n} a_k\right)^2+\left(\sum_{k=1}^{n} b_k\right)^2}. \tag{25}$$

5. Limiting Value of L_n and R_n

The correct value of inductance and resistance per unit length is obtained in the limit as n becomes infinite. A good estimate of the correct L and R can be obtained from several approximations calculated for different values of n. The approximate values of L and R are plotted against n as shown in figure 5 and 6. The asymptotes to these curves are the values as n becomes infinite.

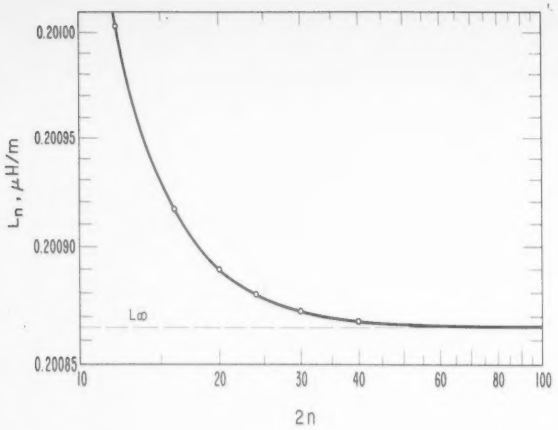

FIGURE 5. *Approximate inductance versus number of subdivisions, showing limiting value of inductance for infinite* n.

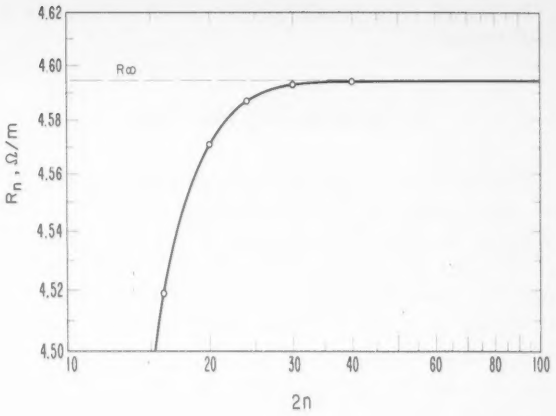

FIGURE 6. *Approximate resistance versus number of subdivision, showing limiting value of resistance for infinite* n.

The curve of L versus n can be approximated by an equation of the form

$$L_n = L\infty + a_n - \mathscr{S} \tag{26}$$

where L_n is the approximate inductance obtained from (24) for a given n, $L\infty$ is the inductance as n becomes infinite, and a and $\mathscr{S}$ are constants. Equation (26) can be solved for $L\infty$ if L_n is calculated for four different n's chosen such that

$$\frac{n_1}{n_2} = \frac{n_3}{n_4}. \tag{27}$$

Then from (26)

$$L\infty = L_{n_4} - \frac{(L_{n_3} - L_{n_4})(L_{n_2} - L_{n_4})}{(L_{n_1} - L_{n_2}) - (L_{n_3} - L_{n_4})}. \tag{28}$$

A plot of $(L_n - L\infty)$ versus n for these 4 values of L_n will be a straight line on log−log paper only if (26) is a valid representation of the curve L_n versus n. Thus, four points can be used to verify (26) as well as to calculate $L\infty$. Once it has been shown that (26) is a valid representation of the curve, $L\infty$ can be calculated from three values of n chosen such that

$$\frac{n_1}{n_2} = \frac{n_2}{n_3}. \tag{29}$$

Then (26) gives

$$L\infty = L_{n_3} - \frac{(L_{n_2} - L_{n_3})^2}{(L_{n_1} - L_{n_2}) - (L_{n_2} - L_{n_3})}. \tag{30}$$

The value of $L\infty$ for the curve shown in figure 5 was calculated from three sets of values of n. For values of n equal to 4, 6, and 9, (30) gave a value of $L\infty = 0.201352$ μH/m. For values of n equal to 9, 12, and 16, (30) gave a value of $L\infty = 0.201344$. For values of n equal 12, 15, 16, and 20, (28) gave a value of $L\infty = 0.201343$. The maximum difference is 5 parts in 10^5. The latter value of $L\infty$ was used to obtain the curve of $(L_n - L\infty)$ versus n shown in figure 7. The time to run these sets of n on a large high speed computer was 10, 35, and 75 seconds respectively.

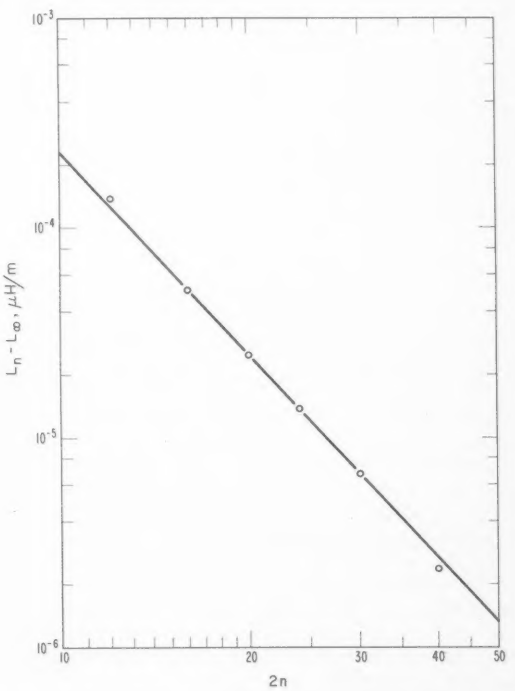

FIGURE 7. *Difference between approximate and limiting value of inductance versus number of subdivisions.*

237-679 O-67—5

No simple approximation was found for the curve of R versus n.

6. Subdividing the Tapes

The exponent, $\mathscr{S}$, in (26) is an indication of the rate of convergence of L_n to its limiting value, $L\infty$. Subdividing the tapes into segments of equal width gave a $\mathscr{S}$ of approximately 1. The variation of the current density across the width of the inner and outer tapes is shown in figure 8. This curve suggests that the width of the segments of the inner tapes be made smaller near the edges where the curve is steepest. One such method of subdivision is to let the width, w_{kn+j} of the $kn+j$ segment be given by,

$$w_{kn+j}=\frac{C}{(n+2-j)^{\eta}} \cdot k=1, 3, 5, 7. \quad j=1, 2, \ldots n \tag{31}$$

where C is determined by setting the sum of the widths equal to $W/2$. Thus

$$\sum_{j=1}^{n} \frac{C}{(n+2-j)^{\eta}}=\frac{W}{2}$$

or

$$C=\frac{W}{2\sum_{j=1}^{n} \frac{1}{(n+2-j)^{\eta}}}. \tag{32}$$

The constant, η, was chosen such that the rate of convergence was near maximum. With the outer tape divided into segments of equal width and the inner tape divided into segments having widths calculated from (31), an η of 3 was sufficient to yield a $\mathscr{S}$ of approximately 3.

7. Typical Results

If the line has losses, the R and L will be a function of the actual dimensions instead of just the ratios t/b, W/b and W_0/b. The R and L of a stripline having dimensions $b=W=0.5$ cm and $t=0.025$ cm, was calculated as a function of frequency f, resistivity ρ, and width of outer conductor W_0. The thickness, T, of all tapes was assumed to be equal and small enough to permit calculation of the M_{ij} in (10) using inductance equations for zero thickness tapes.[2] Machine storage limitations prevented including the variation of current density with thickness. This limits the strict application of these results to tapes whose thickness is of the order of a skin depth. For the geometry considered here the errors introduced even at high frequencies should be negligible.

[2] See appendix.

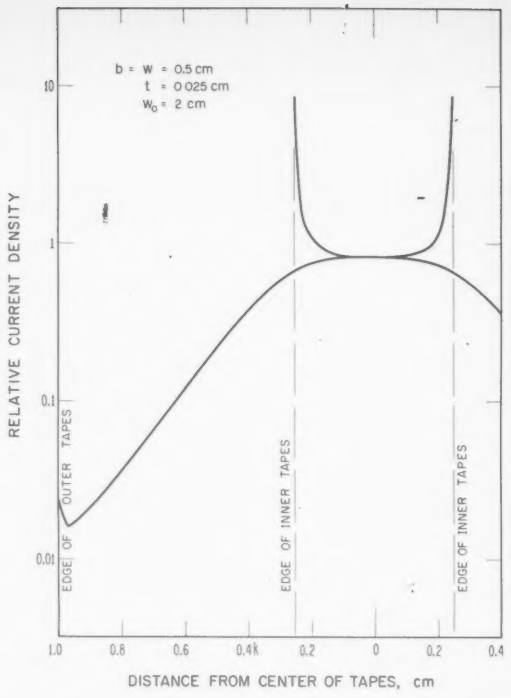

FIGURE 8. *Variation of current density in the inner and outer tapes.*

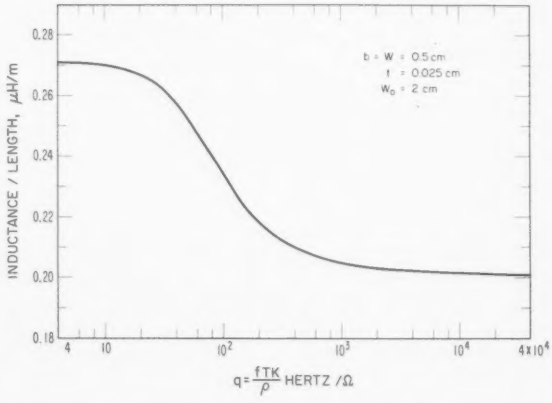

FIGURE 9. *Variation of inductance per unit length with* q.

The variation of inductance per unit length with frequency and resistivity is shown in figure 9. The reason for using the variable $q=fTk/\rho$ is that one curve of L versus q is sufficient for all f, T, k, and ρ, provided that T meets the requirements just discussed. The scale factor k is a dimensionless proportionality constant for striplines having proportionate dimensions and shape. If all dimensions, except the thickness,

are multiplied by a scale factor, k, the matrix M in (16) and (17) remains unchanged. The matrix R^{-1} in (16) and (17) is a function of k and may be written

$$R^{-1}=\begin{pmatrix} \frac{Tkw_1}{\rho} & & 0 \\ & \ddots & \\ 0 & & \frac{Tkw_{2n}}{\rho} \end{pmatrix}=\frac{Tk}{\rho}\mathcal{W} \qquad (33)$$

where

$$\mathcal{W}=\begin{pmatrix} w_1 & & 0 \\ & \ddots & \\ 0 & & w_{2n} \end{pmatrix}.$$

Equations (16) and (17) can now be written,

$$A=\frac{Tk}{\rho}\mathcal{W}\left[(1)+\left(\frac{\omega Tk}{\rho}\mathcal{M}\mathcal{W}\right)^2\right]^{-1} \cdot\left[E+\left(\frac{\omega Tk}{\rho}\mathcal{M}\mathcal{W}\right)F\right] \qquad (34)$$

$$B=\frac{Tk}{\rho}\mathcal{W}\left[(1)+\left(\frac{\omega Tk}{\rho}\mathcal{M}\mathcal{W}\right)^2\right]^{-1} \cdot\left[\left(\frac{\omega Tk}{\rho}\mathcal{M}\mathcal{W}\right)E-F\right]. \qquad (35)$$

Since the matrices $\mathcal{M}$ and $\mathcal{W}$ are independent of f, T, k, and ρ, one curve of L versus the variable $q=fTk/\rho$ will be sufficient for all f, T, k, and ρ. The same result is true for R/R_{dc} versus q. For the strip line under consideration, with $T=10^{-4}$ cm, $\rho=2\times10^{-6}$ Ω cm, and $k=1$, a q of 5×10^4 hertz/Ω corresponds to a frequency of 10^3 hertz.

A curve of R/R_{dc} for the stripline versus q is shown in figure 10. An explanation of the shape of the curve can be had from an examination of the current density curves such as shown in figures 8 and 11. The current density in the outer tapes remains uniform up to about $q=5$. From $q=5$ to about $q=5000$ the current distribution is changing. Above a q of about 5000 the current distribution in the outer tapes no longer changes. The resistance of the outer tape would therefore remain constant up to a q of 5, increase until a q of 5000 is reached and then remain constant again. The current density in the inner tapes remains uniform up to a q of 50. The current then begins to crowd to

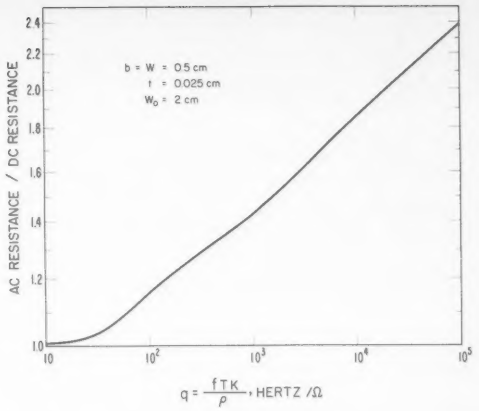

FIGURE 10. *Variation of resistance with* q.

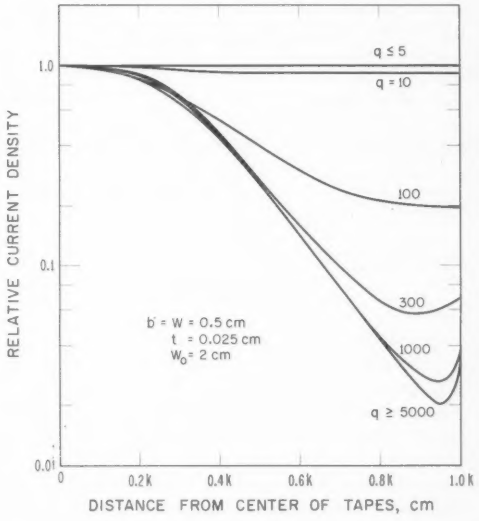

FIGURE 11. *Normalized current density in outer tapes as a function of* q.

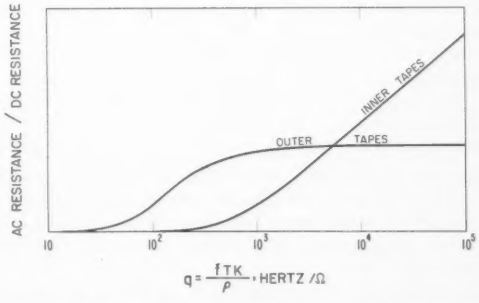

FIGURE 12. *Variation of Resistance with* q *for the outer and inner tapes.*

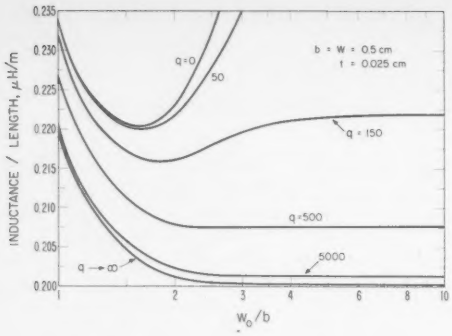

FIGURE 13. *Variation of inductance per unit length with width of outer tapes.*

the edges of the inner tapes. The current continues to move to the edges as long as the value of q increases, never reaching a constant distribution as the current in the outer tape does. The curves of the change in resistance of the outer and the inner tapes with q would look like those shown in figure 12. The sum of these two curves gives a curve like that shown in figure 10.

The variation of inductance per unit length with the width of the outer tapes is shown in figure 13 for different values of q, for the dimensions given above.

8. Summary

The inductance and resistance per unit length of strip transmission line are functions of the current distribution in the conductors. At frequencies where the current distribution throughout the conductors is uniform, the inductance and resistance can be calculated exactly. For frequencies where the current distribution is not uniform, the conductors are divided into sections. From these sections the approximate current distribution of the conductors is calculated. Approximate values of the inductance and resistance per unit length are then calculated from the approximate current distribution. Using high speed computers, it is not difficult to divide the conductors into sufficiently small sections to calculate the inductance to an accuracy of one part in 10^5 or better. The accuracy on resistance is considerably less, depending on frequency. Other methods of subdividing the tapes are being considered to improve the convergence of R_n to its limiting value, R_∞.

The variation of the inductance per unit length with frequency, resistivity, and width of the outer conductors is given for a particular geometry. Tables and graphs of the inductance and resistance per unit length for other geometries are being prepared for future publication.

The technique of calculating R and L as given in this paper for a stripline can be applied to other lines having more complicated cross sections provided that the conductors can be divided into sections whose d-c self and mutual inductances can be calculated. This technique is used in a forthcoming paper by Brooke and Cruz [7] to calculate the L and hence Z_0 of a lossless, rectangular line with a rotating center conductor.

The authors gratefully acknowledge the assistance and helpful criticism of C. M. Allred, and W. E. Little.

9. Appendix

The mutual inductance per unit length between two long, thin, parallel tapes such as shown in figure 14 can be obtained from equation 8 of reference [6] and is

$$\mathscr{M}_t=\frac{0.2}{ad}\left[\frac{P^2-x^2}{4}\ln(P^2+x^2)-xP\,\mathrm{Tan}^{-1}\frac{x}{P}\right]_{E+d-a,\,E}^{E-a,\,E+d}(x)+0.2\left[\ln 2l+\frac{1}{2}\right],\ \mu\mathrm{H/m}\qquad(A1)$$

where the limits, which have been retained for compactness, are substituted as follows:

$$[f(x)]_{s_2s_4}^{s_1s_3}(x)\equiv\sum_{i=1}^{4}(-1)^{i+1}f(s_i).$$

The origin coincides with the left edge of one tape. If the left edge of the second tape is in any quadrant other than the first as shown, one or both of the values of E and P will be negative. The self-inductance per unit length of a long thin tape is

$$L_t=0.2\ln\frac{1}{a}+0.2\left[\ln 2l+\frac{1}{2}\right],\ \mu\mathrm{H/m}.\qquad(A2)$$

In both of these expressions it is assumed that the current density is uniform throughout the conductors.

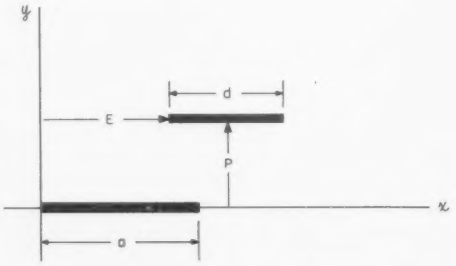

FIGURE 14. *Cross sectional view of two long parallel thin tapes.*

Note that the term

$$0.2\left[\ln 2l+\frac{1}{2}\right] \tag{A3}$$

appears in both M_l and L_l as the only term involving length. However, if M_l and L_l are substituted into (8), the terms involving length will exactly cancel. Substituting (A1) and (A2) into (8) gives

$$V_k = r_k I_k + j\omega \sum_{l=1}^{8n} M'_{kl} I_l + j\omega \left[0.2\left(\ln 2l+\frac{1}{2}\right)\right] \sum_{l=1}^{8n} I_l \tag{A4}$$

where the M'_{kl} are the expressions in (A1) and (A2) with the (A3) term excluded. But the last term is zero because

$$\sum_{l=1}^{8n} I_l = 0.$$

That is, the total current in the outer conductors is equal and opposite to the total current in the inner conductors. Therefore the M_k in (8) may be calculated from (A1) and (A2) with the (A3) term excluded.

10. References

[1] O. R. Cruzan and R. V. Garver, Characteristic impedance of rectangular coaxial transmission lines, IEEE Trans. on Microwave Theory and Techniques **MTT-12,** pp. 489–495 (Sept. 1964).

[2] S. B. Cohn, Characteristic impedance of the shielded-strip transmission line, IRE Trans. **MTT-2,** pp. 52–57 (July 1954).

[3] R. H. T. Bates, The characteristic impedance of the shielded slab line, IRE Trans. **MTT-4,** pp. 28–33 (Jan. 1956).

[4] H. E. Green, The numerical solution of some transmission line problems, IEEE Trans. on Microwave Theory and Techniques **MTT-13,** pp. 676–692 (Sept. 1965).

[5] Ramo, Whinnery, and Van Duzer, *Fields and Waves in Communication Electronics*, p. 400 (John Wiley & Sons, Inc., New York, N.Y., 1965).

[6] C. A. Hoer and C. H. Love, Exact inductance equations for rectangular conductors with applications to more complicated geometries, J. Res. NBS **69C2** (Engr. and Instr.), No. 2, 127–137 (Apr.–June 1965).

[7] R. L. Brooke and J. E. Cruz, High frequency current distribution and impedance of lossless conductor systems, to be published.

(Paper 71C–444)

JOURNAL OF RESEARCH of the National Bureau of Standards—C. Engineering and Instrumentation
Vol. 71C, No. 1, January–March 1967

Tensor Permeability Measurements at L-Band Frequencies Using a Degenerate Mode Cavity

L. B. Schmidt,* R. D. Harrington,* and W. E. Case *

Institute for Basic Standards, National Bureau of Standards, Boulder, Colo. 80302

(October 18, 1966)

The exact solution for the field equations of a cylindrical TM_{110} mode cavity has previously allowed accurate measurements of tensor permeability to be obtained at X-band frequencies. It is demonstrated that this method is also applicable at frequencies down to 1 GHz. A brief description of the cavity and measurement system for obtaining data at these lower frequencies is given. Both intrinsic and external permeability results on three commercially available polycrystalline garnets are shown. The larger size rods required for measurements at these frequencies result in some sample size effects in the data. In addition, a previously unreported absorption in the external tensor permeability of the materials was observed.

Key Words: Degenerate mode cavity, L-band cavity, polycrystalline garnets, tensor permeability.

1. Introduction

A knowledge of the tensor permeability components as described by Polder [1][1] of a ferrimagnetic material is often required in the theory and design of ferrite devices at microwave frequencies. Considerable effort has been directed towards the measurement of these parameters in recent years. Most of these tensor permeability studies have been carried out using cavity techniques [2–18]. In particular, degenerate mode cavities excited with either a positive or negative pure circularly polarized wave have been the most accurate means available for obtaining measurements of this type. Both TE and TM mode cavities have been used in this manner. In comparing the degenerate mode cavity methods, the measurement of rod-shaped samples placed along the axis of a TM_{110} mode cylindrical cavity has been particularly attractive since this geometry allows an exact solution to be obtained for the field equations [19–20].

The measurement of tensor permeability using the TM_{110} mode cavity as well as any of the other cavity methods has in general been confined to frequencies of 3 GHz or higher. Exceptions to this may be found in the work of Ogasawara [21–23] as well as Waldron and Maxwell [24–27], who use stripline techniques for measurements from 3 GHz down to the UHF range. Ogasawara describes measurements of disks in crossed stripline cavities. Waldron and Maxwell use thin rectangular plates in a single stripline cavity. In either case, the use of disk or rectangular shaped samples in stripline may be subject to errors due to sample geometry effects, nonuniform electromagnetic fields, etc. [28–29].

It appears feasible that some of the errors associated with sample measurements in stripline could be avoided, at least in the frequency range down to about 1 GHz, by the use of the previously mentioned TM_{110} mode cylindrical cavity at these lower frequencies. This cavity offers advantages over other waveguide cavities at lower frequencies for two reasons. First, this mode allows a flat cylindrical type cavity to be designed which is sufficiently thin along the axis, even at these lower microwave frequencies, to fit between the pole pieces of an electromagnet. Second, the rod-shaped samples and exact solution for the field equations mentioned above should help to avoid sample shape errors appearing in other methods.

This paper describes a feasibility study which uses a TM_{110} mode cavity for tensor permeability measurements in the L-band region. A brief description is given of the measurement method, the cavity, and the associated circuitry used in these measurements. Several improvements in the TM_{110} mode cavity are noted which are also applicable to the use of this method at higher frequencies. This is followed by a description of typical data obtained on three commercially available polycrystalline garnets at 1106 MHz.

2. Measurement Technique

2.1. General Method

The general procedure for measuring tensor permeability using degenerate mode cavities is based on

*Radio and Microwave Materials, Radio Standards Physics, NBS Laboratories, Boulder, Colo. 80302.

[1] Figures in brackets indicate the literature references at the end of this paper.

the fact that the magnetic flux b in a magnetic material is related to a circularly polarized field h_i inside the material by the relation [4]

$$b_{\pm}=(\mu\pm\alpha)h_{i_{\pm}}. \tag{1}$$

In this equation, μ and α are both complex and are the diagonal and off diagonal components of the intrinsic tensor permeability. The subscripts refer to either a positive or a negative circularly polarized wave.

In a typical measurement, the frequency shift and change in Q of a cavity containing a small sample are determined as a function of an applied d-c field for each of the two senses of circular polarization. In most cases, the experimental relationship between $(\mu\pm\alpha)$ and the changes in the resonant frequency and Q of the cavity are determined from cavity perturbation theory. However, in the case of the TM_{110} mode cylindrical cavity containing a rod-shaped sample along the axis, the correspondingly more exact relations may be obtained from a direct application of Maxwell's equations to the sample and cavity geometry as shown by Bussey and Steinert [19–20]. This approach is well described in their papers and will not be repeated here. It suffices to point out that the intrinsic permeability data in this paper have been calculated with the aid of a computer from eqs (10) and (11) of their paper [20].[2]

To accurately identify the resonant field and the maximum value of the imaginary part of $(\mu+\alpha)$, it was necessary to know the d-c field value at increments of one oersted immediately above and below resonance. The accuracy of the available equipment for measuring the d-c field in the range of values used in these measurements was not adequate to obtain this resolution. The relation between the measured frequency and the applied d-c field was very nearly linear. This made it possible to plot this relation and interpolate between experimentally observed points. The experimental data and the data obtained by this interpolation were combined to obtain the intrinsic permeability data shown in this paper.

It should be emphasized that the permeability $(\mu\pm\alpha)$ defined in eq (1) and calculated from the formulas of Bussey and Steinert is the intrinsic permeability which does not depend upon the geometry of the sample. This situation arises because the field h_i in eq (1) refers to the rf field inside the sample. In some cases a so-called "external" permeability $(\eta\pm\kappa)$ has been referred to in the literature. This is defined in terms of the rf field h_0 existing in the absence of the specimen. In this case, we have an analogy to eq (1)

$$b_{\pm}=(\eta\pm\kappa)h_{0_{\pm}}, \tag{2}$$

where η and κ are again complex and are the diagonal and off diagonal components of the external permeability. In the case of a rod sample, Waldron [30] has shown that the external permeability is related to intrinsic permeability by the relation

$$\eta\pm\kappa=\frac{2(\mu\pm\alpha)}{1+(\mu\pm\alpha)}. \tag{3}$$

In this paper, we are primarily concerned with the evaluation of the intrinsic permeability. However, the above concept of external permeability is included primarily because we have observed previously unreported absorption phenomena.

2.2. Cavity Details

A simplified drawing of the circular TM_{110} mode cavity developed for making tensor permeability measurements at L-band frequencies is shown in figure 1. A resonant frequency of 1106 MHz was chosen which results in a cavity having an inside diameter of about 13 in. and an inside height along the axis of approximately 1.4 in. As previously mentioned, this readily allows the cavity to be placed between the pole pieces of a typical electromagnet since the magnetic field is applied parallel to the axis of the sample and cavity.

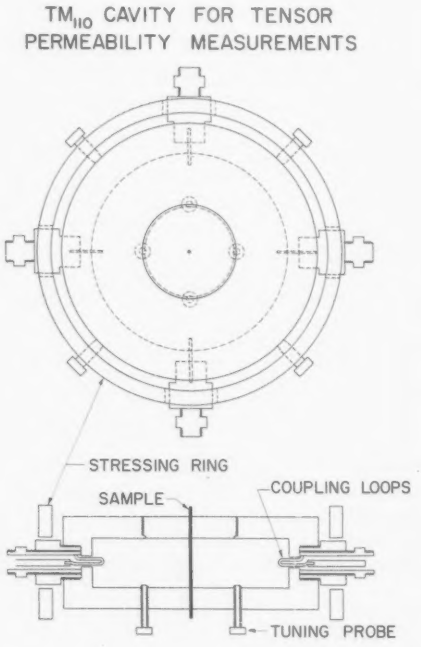

FIGURE 1. *Simplified drawing of TM_{110} mode cavity for tensor permeability measurements at 1106 MHz.*

[2] The signs preceding the ϵ'' and ϵ' terms of eq (11) in ref. 20 should be − and + respectively rather than as given in the paper. This is because the expression for inverse permeability m^* should have been $m^*=m'-im''$ rather than $m'+im''$ which the authors used in their discussion.

The cavity itself was fabricated from a solid piece of brass with an access lid having a radius of 48 percent of the inside radius of the cavity which corresponds to a low current region. The solid piece of brass was employed to avoid the use of mechanical joints in the regions of high current such as at the periphery of the cavity. Earlier designs of cylindrical cavities using lids that made contact at the corners demonstrated that it is difficult to obtain a perfectly symmetrical contact resistance around the periphery of the cavity. Tuning probes are located in the region of high electric field on the solid end of the cavity as seen in figure 1. It was observed that better circular polarization conditions could be obtained by using the above techniques.

Further minor adjustments are still necessary for obtaining optimum circular polarization conditions in the cavity. For example, as shown in figure 1, a heavy ring clamp is placed around the outer circumference of the cavity with adjusting screws for stressing the cavity in compression. This allows slight adjustments to be made in the circular symmetry of the cavity. Four small tuning probes as shown in figure 1 were placed in line with the coupling loops and at the point of maximum electric field to provide further fine adjustments in the tuning of the cavity. Adjustable coaxial coupling loops were also used. These of course readily allow coaxial lines, rather than waveguide, to be used external to the cavity which is advantageous at these lower frequencies. At the same time, the coaxial loops easily allow small adjustments in the coupling to be made in order to obtain a pure circularly polarized mode.

The procedure for obtaining circularly polarized waves in the cavity is carried out by first adjusting the compression screws, tuning probes, and coupling loops of the empty cavity in an iterating procedure to equalize the magnitude and frequency of the two possible modes of the degenerate mode cavity. Further adjustments are then made by placing a ferrite rod in the cavity and observing any resulting mode splitting when the ferrite is biased with a d-c field. Final adjustments using the coupling loops and line stretchers, which are external to the cavity, are then made in an effort to completely suppress one mode when the cavity is excited by a circularly polarized wave. It should be noted that it is more difficult to obtain the final adjustments with the sample in the cavity at L-band frequencies than at the higher frequencies. This is partly because the greater low field losses make it more difficult to distinctly see the splitting of the two modes. However, as will be shown in this paper, it is still possible to obtain good data.

Figure 2 is a photograph of the cavity showing many of the features described above. A typical sample is shown at the center of the cavity. In an actual measurement, the sample would be inserted through the small hole in the lid and cavity as shown. The lid would of course be on the cavity and would not be opened during the measurement. The small rod protruding from the stressing ring in the lower right-hand corner of the photo is used for hanging the cavity between the pole pieces of the electromagnet.

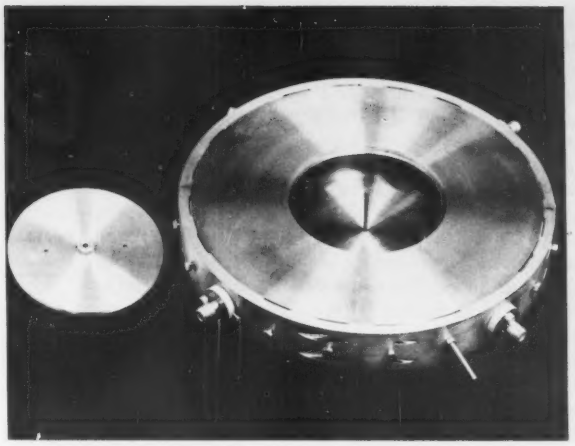

FIGURE 2. *Photograph of TM_{110} mode cavity with lid removed showing typical sample.*

2.3. Measurement System

The basic requirements in the circuit for tensor permeability measurements are shown in figure 3. The equipment used in this system is derived from commercially available coaxial components modified where necessary to meet the needs of these measurements. In particular, the microwave source is a commercial oscillator whose power supply was replaced by well-regulated direct current power supplies to improve the quality and stability of the signal. The plate supply was regulated to 0.002 percent, and the filament supply regulation was adequate at 0.5 percent. The system also makes use of IF detection to increase sensitivity and a phase-locked local oscillator system was used to assist in tracking the microwave source during the measurements [31].

Optimum accuracy in the resonant frequency and Q measurements of the cavity was assured by using a transfer oscillator in conjunction with a frequency counter. The crystal detector and galvanometer was in turn calibrated using a 30-MHz piston attenuator in the IF circuit in order to improve the accuracy of the 3-dB points on the cavity resonance curve used in the Q determinations.

The equal 90° phase shifted signals needed for circular polarization are obtained by the phase and power splitter in conjunction with the line stretchers. These adjustable length coaxial lines readily allow fine adjustments to be made on the phase which is necessary for obtaining good circular polarization.

3. Measurement Results

The permeabilities of three commercially available polycrystalline garnet materials of different magnetizations were measured at 1106 MHz. These materials will be identified as follows:

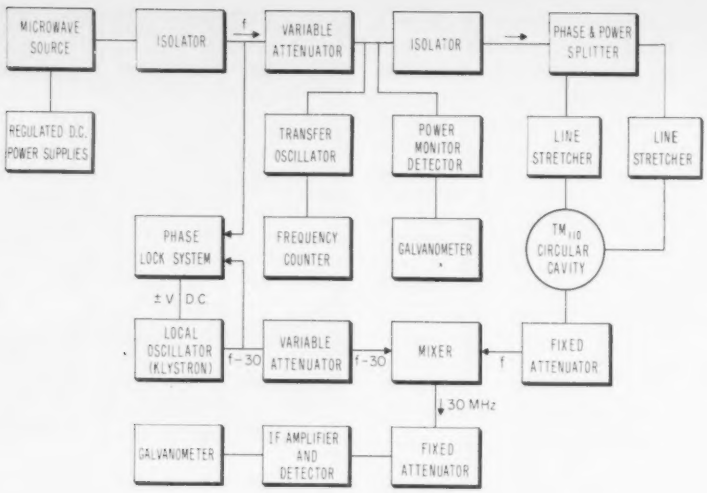

FIGURE 3. *Schematic diagram of circuit components used in tensor permeability measurements at L-band frequencies.*

Material	Composition	Saturation magnetization, $4\pi M$ in gauss
A	Substituted YIG	580
B	Substituted YIG	1158
C	YIG	1799

Measurements were made on rods of diameters 0.100, 0.150, 0.200, 0.250, and 0.300 in. Although data could be obtained on all these rods, the smaller diameters (0.1 in–0.15 in) resulted in poor precision because of the resulting small frequency shifts while the large rods (0.3 in) proved difficult to measure because of the greater loss introduced into the system. The best data were obtained on the 0.250 in rods.

The real and imaginary parts of the intrinsic tensor permeability values, $(\mu' \pm \alpha')$ and $(\mu'' \pm \alpha'')$, for the above three materials using 0.250 in diameter rods whose lengths ranged from 2.850 in to 2.882 in are shown in the top graph of figures 4, 5, and 6. It is of interest that these relatively good tensor permeability resonance curves were obtained on rod samples whose ordinary Kittel resonance properties could not be measured at L-band frequencies using a rod geometry due to the low fields resulting in unsaturated conditions in the sample.

It is feasible that low field effects may also be influencing the accuracy of these tensor permeability measurements. For example, we have shown the external tensor permeability for positive circular polari-

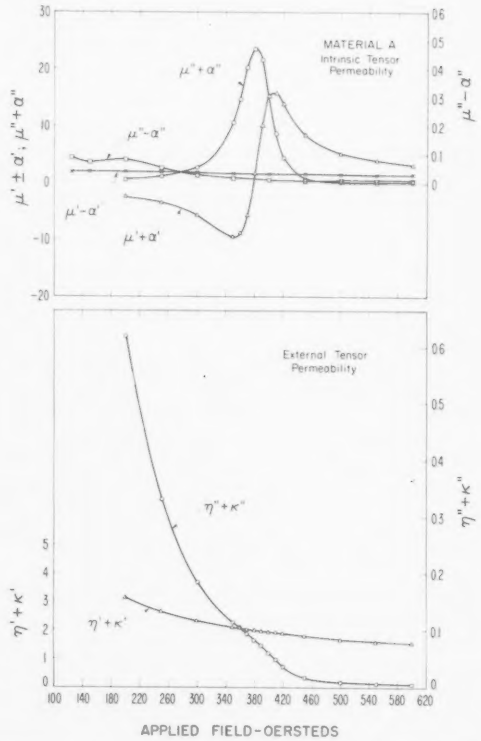

FIGURE 4. *Intrinsic and external tensor permeabilities for polycrystalline substituted yttrium iron garnet, material A, $4\pi M = 580$ G.*

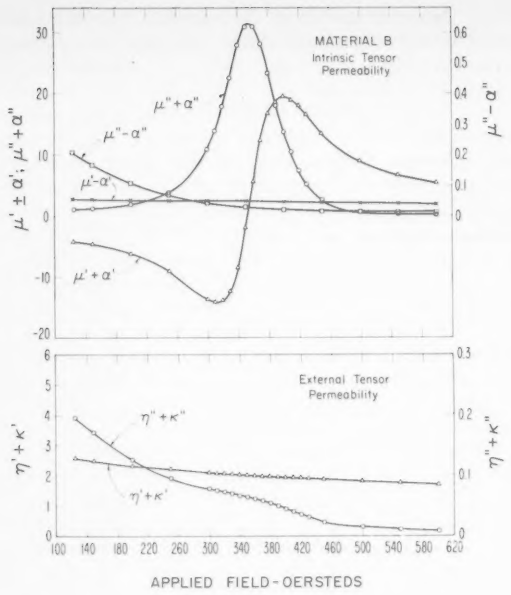

FIGURE 5. *Intrinsic and external tensor permeabilities for polycrystalline substituted yttrium iron garnet, material B, $4\pi M = 1158$ G.*

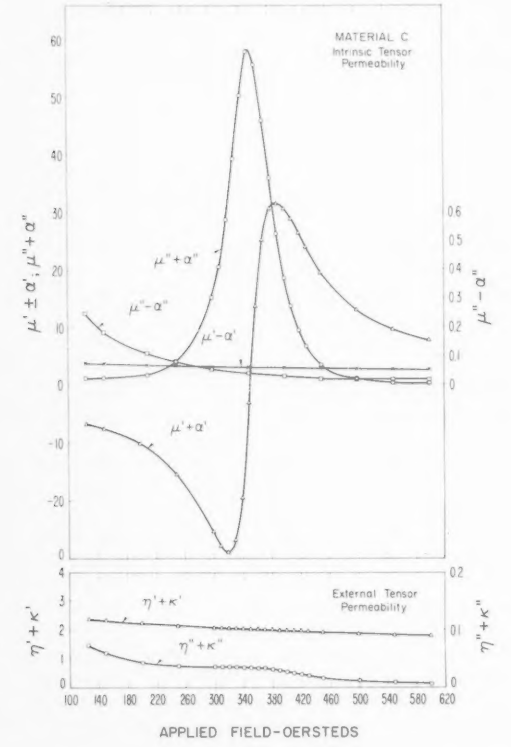

FIGURE 6. *Intrinsic and external tensor permeabilities for polycrystalline yttrium iron garnet, material C, $4\pi M = 1799$ G.*

zation conditions corresponding to the above intrinsic tensor results in the bottom graphs of figures 4, 5, and 6. These curves were calculated from the intrinsic tensor values using eq (3). The external permeability curves are essentially just the high field side of the Kittel resonance curve. Based on data obtained at higher frequencies [5], both $\eta' + \kappa'$ and $\eta'' + \kappa''$ might be expected to be smoothly decreasing curves. However, in all three cases, a slight absorption was observed in the $\eta'' + \kappa''$ data in the vicinity of the intrinsic tensor permeability resonance. This same phenomena was similarly observed in measuring one of the rods in a rectangular TE_{102} rectangular cavity at 1107 MHz indicating that it probably is not related to the adjustment of the circular polarization in our cylindrical cavity. It was also observed on rods ground into prolate ellipsoids indicating that it is not a macroscopic geometry effect. It is probably related to the relatively low fields used in these experiments although further studies are necessary in this area.

It is also of interest that the small absorption located at a field of about 200 Oe in the $\mu'' - \alpha''$ curve for material A in figure 4 appeared in measurements of different size rods of the same material and also in a prolate ellipsoid formed from one of the rods. This phenomena again may be characteristic of this material at low fields.

Further studies were carried out in an effort to determine the precision and accuracy of the system for measuring the intrinsic tensor permeability which was of primary interest in our program. First of all, it was observed that, for any given rod, the field for maximum absorption in $\mu'' + \alpha''$ could be repeated to better than 1 percent while the linewidth and maximum value of $\mu'' + \alpha''$ at resonance could be repeated to better than 5 percent. However, it was noted that data obtained on different rods may show a much greater variation than this which is probably due to sample inhomogeneity effects, etc.

The linewidths of the three materials obtained from the plotted results in figures, 4, 5, and 6 were compared with corresponding measurements on disk samples in a rectangular TE_{102} mode cavity at 1107 MHz using the technique adopted by the ASTM [32]. Disks having aspect ratios (diameter/thickness) of the order of 83 to 85 were used in an effort to minimize shape effects [33]. The results are shown in the following table:

Sample	Linewidth (oersteds)	
	Tensor meas. (rods)	ASTM meas. (disks)
A	51	48
B	82	78
C	66	62

The agreement is remarkably good considering the variations that are often experienced even from samples cut from the same slab of material. These results indicate that the tensor results give a very good indication of the linewidth in addition to providing information on the individual tensor permeability components.

It is also recognized that the rods used at these frequencies do not approximate infinitely long cylinders, and demagnetizing corrections may be necessary. For example, it is well known that the internal field H_i in a material is related to the external field H_0 by the relation

$$H_i = H_0 - NM, \tag{4}$$

where N is the demagnetizing factor and M is the magnetization. The data shown in figure 7 for the three materials indicate that the applied field for resonance, H_o, does increase slightly with increasing rod diameter. Better results are obtained using the corresponding data for the internal field H_i calculated using eq (4), and N values obtained from Bozorth [34], with values of M corresponding to the internal field as determined independently with a magnetometer. It thus appears that small size effects in resonant field values can be expected; however, these can be partially corrected for in the case of the rod samples.

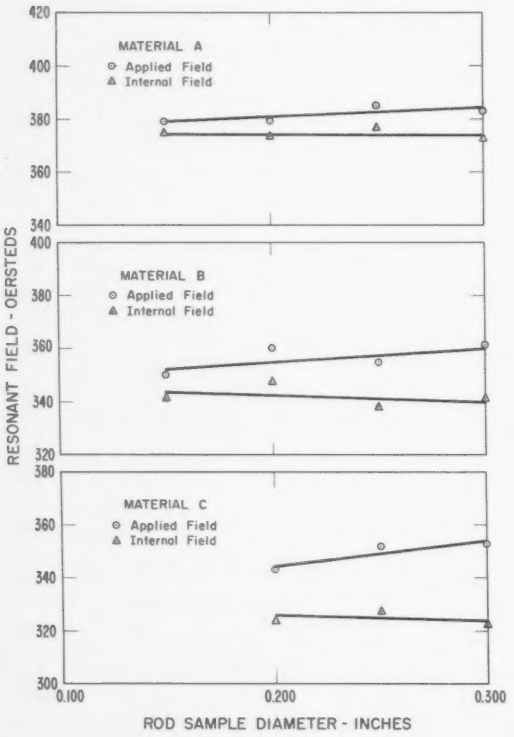

FIGURE 7. *Dependence of intrinsic tensor permeability resonant field on sample diameter for materials A, B, and C.*

No definite trend in linewidth on rod diameter could be identified within the variations of data observed on different rods. The linewidth varied considerably on different size rods that were cut from the same slab; therefore, it is possible that some size effects may still be present within the total variation.

It is apparent that some of the above variations in resonant field and linewidth could be comparable to similar variations on size previously observed in ferromagnetic resonance studies on disks [33]. It is also of interest to note that differences in the properties of ellipsoids and rods using the TM_{110} cavity, as well as ellipsoids and disks measured in the previous program, were observed. It thus appears that rod samples in the TM_{110} cavity as well as thin disk samples such as might be used in a stripline cavity may both result in some sample-shape errors in tensor permeability measurements.

Although the TM_{110} cavity method does not completely eliminate the problem of sample shape errors occurring in other methods, the cylindrical symmetry and ability to make several adjustments on the cavity for obtaining circular polarization may have advantages over stripline methods using disks. Furthermore, the cylindrical cavity allows the use of a long rod sample which is a distinct advantage when data in the vicinity of the intrinsic tensor permeability resonance are desired since this resonance coincides with the ordinary ferromagnetic resonance in disks but not in rods. The complications introduced by this higher loss in the disks have been previously recognized at higher frequencies [6] and further substantiated by our own efforts to measure disks at these lower frequencies.

4. Conclusions

On the basis of the above study, it is concluded that a degenerate TM_{110} mode cavity is very satisfactory for measuring the tensor permeability of rod samples at frequencies as low as 1 GHz. It is possible to obtain good linewidth measurements on cylindrical samples which ordinarily could not be measured at these frequencies using standard rectangular waveguide techniques normally used in studies of the Kittel resonance.

Although the use of rods in this method offers some decided advantages over disks in stripline when measuring intrinsic tensor permeability near resonance, the TM_{110} cavity method is still influenced by some sample shape effects. It is possible that all low frequency tensor permeability measurements may be influenced by sample shape effects that are related to the low fields involved. These results along with the appearance of a small anomalous absorption in the external permeability observed in our rod data in the vicinity of the intrinsic tensor permeability resonance indicate that there is still a need for further work describing ferromagnetic resonance and tensor permeability properties at low frequencies and applied fields.

The authors express their appreciation to H. E. Bussey for helpful discussions regarding the TM_{110} cavity method and the associated exact solution.

5. References

[1] D. Polder, On the theory of ferromagnetic resonance, Phil. Mag., **40,** 99–115 (Jan. 1949).

[2] A. A. Th. M. Van Trier, Guided electromagnetic waves in anisotropic media, Appl. Sci. Res., Sec. B **3,** 305–371 (1953).

[3] J. O. Artman and P. E. Tannenwald, Measurement of susceptibility tensor in ferrites, J. of Applied Physics, **26,** No. 9, 1124–1132 (Sept. 1955).

[4] E. G. Spencer, R. C. LeCraw, and F. Reggia, Measurement of microwave dielectric constants and tensor permeabilities of ferrite spheres, Proc. IRE **44,** No. 6, 790–800 (June 1956).

[5] E. G. Spencer, L. A. Ault and R. C. LeCraw, Intrinsic tensor permeabilities on ferrite rods, spheres and disks, Proc. IRE **44,** No. 10, 1311–1317 (Oct. 1956).

[6] W. Von Aulock and J. H. Rowen, Measurement of dielectric and magnetic properties of ferromagnetic materials at microwave frequencies, Bell System Tech. J. **XXXVI,** No. 2, 427–448 (Mar. 1957).

[7] I. G. MacBean, The measurement of complex permittivity and complex tensor permeability of ferrite materials at microwave frequencies, Proc. Inst. of Elec. Engrs. **104,** Part B, Supplement 6, pp. 296–306 (1957).

[8] N. Ogasawara, On the measurement of permittivity and tensor permeability of thin ferrite rods, Electrotechnical Journal of Japan **3,** No. 4, 126–130 (Dec. 1957).

[9] C. M. Srivastava and J. Roberts, Measurement of ferrite loss-factors at 10 Gc/s, Proc. Inst. of Electrical Engineers **105,** Part B, 204–209 (Mar. 1958).

[10] W. S. Carter, Apparatus for the measurement of tensor permeability and dielectric properties of ferrites at X-band frequencies, Marconi Review **22,** No. 134, 154–163, Third Quarter (1959).

[11] K. H. Gothe, Experimentelle bestimmung der komponenten des permeabilitätstensors und des spektroskopischen aufspaltungsfaktors an Mg-Mn-ferriten im mikrowellengebiet, I. Annalen Der Physik 7 Folge **6,** 298–306 (1960).

[12] F. Dachert and A. Schmouchkovitch, Mesure du tenseur de permeabilite des ferrites a 3000 et 8500 megacycles par seconde, J. de Physique et le Radium, Physique Appliquee, Tome **21,** Supplement Au No. 3, 57A–64A (Mar. 1960).

[13] D. I. Mash and V. V. Nikol'skii, Measurement of the complex dielectric susceptibility and the magnetic susceptibility tensor of ferrites in the millimeter-region, Soviet Physics-Technical Physics **4,** No. 9, 978–980 (Mar. 1960).

[14] F. Okada, Rectangular cavities for measurement of dielectric constants and tensor permeabilities of ferrites, Defense Academy, Yakosuka, Japan, Memoirs **2,** No. 1, 52–67 (Oct. 1961).

[15] C. P. Aron, The design and construction of a cavity for the measurement of the tensor susceptibility of ferrite materials, Proc. Inst. of Electrical Engineers **109,** Part B, Supplement No. 23, 867–878 (1962).

[16] M. Bujatti, Measurement of tensor permeability on ferrites, Alta Frequenza **XXXII,** No. 5, 366–369 (1963).

[17] V. Cagan and B. Lemaire, Mesures de permittivite et de permeabilite de ferrites a differentes frequences, Electronic Magnetic Resonance and Solid Dielectrics, pp. 517–524, Proc. of the XIIth Colloque Ampere, Bordeaux, September 1963, editors: R. Servant, A. Charru, (North Holland Publ. Co., Amsterdam, 1964).

[18] R. M. Bulley, Measurement of tensor permeability of a ferrite at 9 Gc/s, Mullard Research Laboratories Report No. 533 (Apr. 1965).

[19] H. E. Bussey and L. A. Steinert, An exact solution for a cylindrical cavity containing a gyromagnetic material, Proc. of IRE **45,** No. 5, 693–694 (May 1957).

[20] H. E. Bussey and L. A. Steinert, Exact solution for a gyromagnetic sample and measurements on a ferrite, IRE Trans. on Microwave Theory and Techniques **MTT-6,** No. 1, 72–76 (Jan. 1958).

[21] N. Ogasawara and Y. Shikata, Improved permittivity and permeability measurements, Microwaves **1,** No. 5, 20–23 (Oct. 1962).

[22] N. Ogasawara and Y. Shikata, Ferromagnetic resonance study using stripline resonators, Tokyo Metropolitan University Faculty of Technology, Memoirs **12,** 908–918 (1962).

[23] N. Ogasawara and S. Yamawaki, Measurement of tensor permeability on some ferrimagnetic materials at VHF band using circularly polarized resonators, International Conference on Microwaves, Circuit Theory, and Information Theory, 1964, Tokyo, Summaries of Papers, Part I Microwaves, Institute of Electrical Communication Engineers of Japan, pp. 131–132.

[24] S. P. Maxwell, A stripline cavity resonator for measurement of magnetic and dielectric properties of ferrites at low microwave frequencies, Marconi Review **27,** No. 152, 22–29, First Quarter (1964).

[25] R. A. Waldron, Theory of the stripline cavity resonator, Marconi Review **27,** No. 152, 30–42, First Quarter (1964).

[26] S. P. Maxwell, A stripline cavity resonator for measurement of ferrites, Microwave Journal **9,** No. 3, 99–102 (Mar. 1966).

[27] R. A. Waldron, Theory of a stripline cavity for measurement of dielectric constants and gyromagnetic resonance line widths, IEEE Trans. on Microwave Theory and Techniques **MTT-12,** No. 1, 123–131 (Jan. 1964).

[28] R. A. Waldron and S. P. Maxwell, Note on the measurement of material properties by the stripline cavity, IEEE Trans. Microwave Theory and Techniques **MTT-13,** No. 5, 711, September 1965.

[29] N. Ogasawara and E. Sawado, Shape dependence of magnetic half-width of ferrimagnetic materials at lower frequency microwaves, Proc. IEEE **54,** No. 4, 678–679 (Apr. 1966).

[30] R. A. Waldron, Intrinsic and external permeabilities and susceptibilities of gyromagnetic materials, British J. of Applied Physics **14,** No. 10, 700–703, October 1963.

[31] W. E. Case, R. D. Harrington, and L. B. Schmidt, Ferrimagnetic resonance measurements using IF substitution techniques, J. Res. NBS **68C** (Engr. and Instr.), No. 4, 255–259 (Oct.-Dec. 1964).

[32] ASTM Test Method C524–63T. This method is under the jurisdiction of the ASTM Committee C–25 on Ceramics for Electronics.

[33] W. E. Case, R. D. Harrington, and L. B. Schmidt, Ferrimagnetic resonance in polycrystalline ferrite and garnet disks at L-band frequencies, J. Res. NBS **68C** (Engr. and Instr.), No. 2, 85–89, April-June 1964.

[34] R. M. Bozorth, Ferromagnetism, pp. 848–849 (D. Van Nostrand Company, Inc., Princeton, New Jersey, 1951).

(Paper 71C1–445)

JOURNAL OF RESEARCH of the National Bureau of Standards—C. Engineering and Instrumentation
Vol. 71C, No. 1, January–March 1967

Publications of the National Bureau of Standards *

Selected Abstracts

Standard x-ray diffraction powder patterns, H. E. Swanson, M. C. Morris, and E. H. Evans, *Mono. 25, Section 4 (June 28, 1966), 55 cents.*

Standard x-ray diffraction powder data are presented for 103 substances. Thirty-two of these patterns represent experimental data and 71 are calculated. Ten experimental patterns replace eleven cards already in the X-ray Powder Diffraction File published by the American Society for Testing and Materials; twenty-two experimental patterns and seventy-one calculated patterns are for substances not previously included in the File. The experimental x-ray powder diffraction patterns were made with a Geiger counter x-ray diffractometer, using samples of high purity. All *d*-values were assigned Miller indices determined by comparison with theoretical interplanar spacings and from space group extinctions. The densities and lattice constants were calculated, and the refractive indices were measured whenever possible. The calculated x-ray powder diffraction patterns were obtained from single crystal structure data. The reported peak height intensities for calculated patterns were converted from integrated intensities.
Accurate cell determination measurements for the internal standards were obtained by using a flat-plate back reflection focusing camera.

Key Words: Constants, crystal, diffraction, lattice, measurements, powder, standard, structure, x-ray.

Electrical parameters of precision, coaxial, air-dielectric transmission lines, R. E. Nelson and M. R. Coryell, *Mono. 96 (June 30, 1966), $1.25.*
Since precision coaxial connectors have become commercially available, precision coaxial, air-dielectric transmission lines are being widely used as radio frequency immittance standards. The evaluation of seven electrical parameters for four different line sizes, which are commonly used as standards, are presented in graphic form. The seven parameters, evaluated as functions of frequency, are inductance per inch, resistance per inch, characteristic impedance magnitude, characteristic impedance phase angle, attenuation per inch, phase-shift per inch, and wavelength. Also included are graphs showing how these parameters vary with changes in the resistivity of the conductors, the relative dielectric constant of air, and the diameters of the conductors.

Key Words: Air-dielectric, coaxial transmission lines, electrical parameters, evaluation, functions of frequency, graphic presentation, and precision.

Dimensional metrology subject-classified with abstracts, I. H. Fullmer, *Misc. Publ. 265 (August 1, 1966), $3.00.*
This bibliography covers two of the three principal divisions of dimensional metrology, namely (1) linear, angular, and geometrical measurements of solid bodies, and (2) in-process control of sizes. The remaining division is gages, gaging, and inspection as to specified limits of size. There are about 3,600 references classified under main subject headings in 12 sections, which are further subdivided into 102 subsections covering 100 subjects. The 12 main subjects are (1) general metrology, physical and dimensional; (2) length and diameter measurements by interferometry; (3) length and diameter measurements by mechanical methods; (4) calibration of line standards of length, including tapes; (5) dimensional measuring instrument design features; (6) angle measurement; (7) measurements of deviations from geometrical regularity; (8) measurement of profile; (9) measurement of screw threads; (10) measurement of gears; (11) measurement of thickness of thin films; and (12) measurement and production techniques for accurate in-process control of size and form. The references in each subsection are arranged chronologically and a brief abstract of each is given with few exceptions. The bibliography is an attempt to organize and make more readily available the extensive existing knowledge in the field covered.

Measures for progress. A History of the National Bureau of Standards, R. C. Cochrane, *Misc. Publ. 275 (1966), $5.25.*
The story of the first half century of the Federal Government's primary scientific research body is told in appealing, interest-holding literary style. Starts with the founding of the Bureau in 1901, when this country was beginning its industrial growth, and physical weights and measures were in a hodge-podge of disorganization. Tells how the Bureau brought order out of this chaos and, through scientific research, went on to establish exacting, reliable new standards involving incredible sophistication in physical measurement. Reflected throughout the book is the remarkable technological, industrial, and commerical growth that the country itself was experiencing, 1901–1951, and the key role played by the National Bureau of Standards in this evolving technology. Thorough documentation and indexing, plus 15 Appendices containing a fund of information not heretofore assembled, make this a valuable reference volume.

Analytical mass spectrometry section: instrumentation and procedures for isotopic analysis, ed. W. R. Shields, *Tech. Note 277 (July 25, 1966), 60 cents.*
This report describes the general instrumentation of the Analytical Mass Spectrometry Section and the specific analytical techniques which have been devised for the measurement of isotopic ratios of Ag, Br, Cl, Cr, Cs, Cu, Mg, Pu, and U. Interim procedures for B, Li, Rb, and Sr are also given.
In the appendix some general statistical principles used in the design and analysis are briefly discussed; an example is given in detail illustrating the various steps involved leading from original data to the reported uncertainties for the isotopic ratio of bromine.

Key Words: Instrumentation, isotopic analysis, mass spectrometry, procedures.

Emission spectrometry, M. Margoshes and B. F. Scribner, *Anal. Chem.* **38,** *No. 5, 297R–310R (Apr. 1966).*
The literature of analytical interest in atomic emission spectrometry, flame photometry, and atomic absorption spectrometry is reviewed for the years 1964–65. The topics included are books and reviews, spectral descriptions and classifications, instrumentation, excitation, standards, calibration, and analytical applications. Literature citations total 351.

Application of sulfur coatings to integrating spheres, S. T. Dunn, *Appl. Opt. Letters* **4,** *No. 7, 877 (July 1965).*
This letter describes several methods of preparing infrared integrating sphere coatings.

Simple contact type temperature controller, L. A. Marzetta, *Rev. Sci. Instr. Note* **37,** *No. 6, 789 (June 1966).*
A simple, low cost temperature controller is described. The circuit has two independent current paths: One provides an On-Off control current, and the other a preselected current for the background heat. With the stated components, 250 watts of heater power can be controlled. For applications such as laboratory liquid baths, 1/1000 °C stability is possible.

Key Words: Mercury-toulene thermometer, temperature controller.

Some statistical properties of pulses from photomultipliers, M. Gadsden, *Appl. Opt.* **4,** *No. 11, 1446–1452 (Nov. 1965).*
An examination of the integrated counts from 9502S and 9558A photomultipliers suggests that the statistical distribution is closely

Poissonian. An examination of the time intervals between consecutive pulses has shown an interesting effect: with a 9502S tube, a highly significant, although small, number of intervals are much longer than expected on a random hypothesis. This effect is explicable in terms of a loss of electrons between cathode and anode. Data on the variation of the signal : noise ratio with differing discriminator bias levels are also presented.

Gas-density stabilizer for flow proportional counters, R. D. Deslattes, B. G. Simson, and R. E. La Villa, *Rev. Sci. Instr.* **37,** *No. 5, 596–599 (May 1966).*
A controller for gas density (pycnostat) is described with particular view to gain stabilization in flow proportional counters. The device is capable of operation at small flow rates and at pressures both above and below atmospheric. Constructional details and performance measurements are reported.

Use of an auxiliary sphere with a spectrophotometer to obtain absolute reflectance, D. G. Goebel, B. P. Caldwell, and H. K. Hammond, *J. Opt. Soc. Am.* **56,** *No. 6, 783–788 (June 1966).*
Reflectance measurements that are made on a scale that is not relative to an arbitrary standard are often called "absolute" measurements. The method presented here uses an auxiliary sphere with a double-beam integrating-sphere spectrophotometer to make measurements on an absolute basis. The basic requirements are: (1) The auxiliary sphere must be uniformly coated with a highly-reflecting, highly-diffusing material. (2) A flat plate must be coated in an identical manner to provide a measure of the coating reflectance. (3) The interior-surface area of the sphere and the area of the entrance port must be measured.
The theory of the method is discussed and an error analysis is made. Reflectance data are reported for specimens of smoked MgO and pressed powders of MgO and $BaSO_4$.
The precision of repeatability has been evaluated from measurements of a Vitrolite-reference standard. More than a dozen measurements at each of eight wavelengths made over a 3-year period exhibited a standard deviation of 0.003 for the spectral reflectance.

Key Words: Absolute, reflectance, spectral.

Influence of an external magnetic field on nuclear resonance in ferromagnetic materials, L. H. Bennett, *J. Appl. Phys.* **37,** *No. 3, 1242–1243 (Mar. 1, 1966).*
The reduction in the amplitude of the nuclear magnetic resonance signal, as well as a change in line shape, upon the application of an external steady magnetic field has been measured for pure nickel at room temperature. Both the transverse and longitudinal configurations (steady field and rf field perpendicular and parallel, respectively) were measured for a sample of nickel powder and for bulk nickel. The signal amplitude drops faster in the longitudinal configuration than in the transverse for each specimen. The reduction in amplitude is considerably less for the pellets than for the powder. There is no sign of a critical field as previously reported. A comparison of the resonance results with the apparent permeabilities is presented.

Key Words: Critical field, field dependence, nickel pellets, nickel powder, nuclear resonance, permeability.

Measurement of absolute wavelength stability of lasers, K. D. Mielenz, R. B. Stephens, K. E. Gillilland, and K. F. Nefflen, *J. Opt. Soc. Am.* **56,** *No. 2, 156–162 (Feb. 1966).*
A technique was devised to measure the absolute wavelength stability of a gas laser by direct interferometric comparison with a mercury 198 standard lamp. The apparatus used is described; its limits of precision are discussed.
The wavelength fluctuations of a free-running, unstabilized helium-neon laser were measured and found to be of the magnitude (several parts in 10^7) due to thermal and mechanical instabilities of the laser cavity.
Manual control of the laser was seen to yield a wavelength constancy (a few parts in 10^8) comparable to the limits of accuracy of interferometric standard sources.

Key Words: Fringe, interferometer, laser, optical, photoelectric, precision, scanning, stability, standard, wavelength.

Measurement of the 633-nm wavelength of helium-neon lasers, K. D. Mielenz, R. B. Stephens, K. E. Gillilland, K. F. Nefflen, and R. B. Zipin, *Appl. Phys. Letters* **7,** *No. 10, 277–279 (Nov. 1965).*
The wavelength of the $3s_2 - 2p_4$ transition of neon was measured by comparison of helium-neon lasers with the Krypton standard of length.

Some applications of the wave front shearing interferometer, J. B. Saunders, *Japanese J. Appl. Phys. Suppl.* **I, 4,** *99–105 (1965).*
This paper gives the results of several applications of the wave front shearing prism interferometer. The instrument is very compact and easy to apply. It is applied to the testing of chromatic aberration of simple and compound lenses; and to the testing of wave forms that characterize the monochromatic aberrations (spherical, coma and astigmatism). Results are shown for several different type lenses. This interferometer is equally applicable to the testing of small lenses and large telescope objectives.

The measurement of homogeneity of optical materials in the visible and near infrared, F. W. Rosberry, *Appl. Opt.* **5,** *No. 6, 961–966 (June 1966).*
A procedure is described for determining the inhomogeneities of a sample of optical material in terms of small changes in index of refraction at discrete points over the measured surface. The method is used in the visible and near infrared regions of the spectrum. A He-Ne gas laser source was used for the infrared measurements. The variation in index was mapped with contour lines enclosing areas of similar index variations. The largest index change in one cm distance was noted and recorded as the maximum gradient per cm. Over 25 different samples of six different materials were examined. The results are presented in a chart indicating the range of maximum index gradients of the samples observed. Data are shown to illustrate the possibility of determining index values to higher precision than the material justifies.

Key Words: Homogeneity, index gradient, infrared, interferometer, laser, measurement, optical, refractive index, shadowgraph.

Electron paramagnetic resonance and nuclear magnetic resonance as analytical tools, T. C. Farrar, *(Proc. Conf. Purification of Materials, New York Academy of Sciences), Ann. N.Y. Acad. Sci.* **137,** *323–334 (Jan. 1966).*
Nuclear magnetic resonance (NMR) spectroscopy is becoming an increasingly important and useful analytical tool. The advantages (such as rapid, non-destructive analysis), disadvantages (such as large sample requirement and low sensitivity), and limitations of high-resolution, broad-line and pulsed NMR techniques as applied to analytical problems are pointed out. Recent developments in instrumentation which have significantly increased the stability and sensitivity of NMR techniques are discussed.
Examples of the use of high-resolution NMR to determine the structure and the purity of samples of the recently-synthesized molecules HBF_2, Si_3BF_2, and Si_3BF_2 are given. The results of a broad-line NMR study to determine the number and the position(s) of the hydrogen atoms in the molecule $Re_3(CO)_{12}H_x$ are presented.
Although paramagnetic species can be detected in concentrations as low as 10^{-11} M, electron paramagnetic resonance (e.p.r.) has been used for quantitative analysis only in a few cases. It is somewhat more useful for qualitative analysis. At this time its prospects for developing into a useful analytical tool seem limited. The reasons for this are briefly discussed.

A cooling system for a laboratory magnet, R. A. Forman and T. McKneely, *Appl. Spectry.* **20,** *189 (May-June 1966).*
The cooling system is described for use with a 5 kW magnet system which enables one to obtain high electrical and thermal stability.

A method for calibrating volt boxes, with analysis of volt-box self-heating characteristics, R. F. Dziuba and T. M. Souders, *IEEE Intern. Conf. Record, Pt. 10, pp. 17 (Mar. 21–25, 1966).*
A modification of the Julie ratiometric method for calibrating volt boxes has been under study at NBS to evaluate its performance as a useful calibration technique. The modification features speed of operation, high accuracy and rated voltage measurements. Evaluation of the method accelerated an investigation of self-heating errors

of volt boxes that was in progress. The results of this study together with an analysis of self-heating curves are included.

Key Words: Calibration, errors, heating, volt-box, voltage divider.

Anomalous conductance behavior in polymers, A. H. Scott (*1965 Annual Report Conf. Electrical Insulation, NAS–NRC Publ. 1356, pp. 98–102 (Natl. Acad. Sci.-Natl. Res. Council, Washington, D.C., 1966).*
Conductance measurements on polymer materials are found to be affected by discharge currents even though the specimen has not had a voltage applied to it. It is necessary to fully discharge a specimen (sometimes for several days) before a repeatable conductance measurement is obtained. The discharge currents are amplified by the use of conductive rubber electrodes rather than tinfoil electrodes. Conductivities that were obtained with conductive rubber electrodes were lower in all cases than those obtained with tinfoil electrodes.

Key Words: Anomalous d-c conductance, conductive rubber electrodes, epoxy, polycarbonate, polystyrene, polyvinylbutyl, polyvinylchloride, tinfoil electrodes.

Apparent negative impedances and their effect on three-terminal dielectric loss measurements, W. P. Harris (*1965 Annual Report Conf. Electrical Insulation), NAS–NRC Publ. 1356, pp. 83–86 (Natl. Acad. Sci.-Natl. Res. Council, Washington, D.C., 1966).*
Tee networks consisting of "stray" impedances can cause "errors" in the conductance and capacitance of three-terminal capacitance measurements. In particular, a tee with two capacitive arms and a resistance leg to ground can introduce a negative component of conductance. Therefore, a three-terminal capacitor can appear to have zero or negative losses. A measurement of the dielectric loss of a material can indicate a negative loss unless steps are taken to eliminate by careful cell design this source of error.
A component of negative loss can arise from the coaxial cables connecting the cell or capacitor to the bridge. This error can be reduced by the use of coaxial chokes or by a feedback circuit.

Key Words: Dielectric losses, dielectric materials, dielectric measurements, errors, low-loss, negative impedances, negative losses.

Flow measurement standardization, T. Filban and M. R. Shafer, *Proc. ISA Conf. 1964, 19, Pt. 1, Paper No. 12–2–4–64 (1964).*
The availability and types of standards related to the measurement of flow are reviewed. The facilities available at the National Bureau of Standards for the calibration of flow-measuring instruments are described; the inaccuracies or uncertainties associated with these measurements are discussed.

Standards for galvanomagnetic devices, S. Rubin, *Solid State Electronics* **9, 5** *559–566 (May 1966).*
A review is given of the Military Standard and the IEC standard for Hall effect devices. Points of outstanding interest such as linearity definitions are detailed. A review of a proposed standard for magnetoresistive devices is given. Similarities between the two standards are noted as are some of the similarities with standards for other flux sensitive resistors such as thermistors and photoresistors.

The NBS instrumentation for use in the measurement of spectral irradiances of solar simulators, R. Stair and W. E. Schneider, *Proc. Inter. Symp. Solar Radiation Simulation, Los Angeles, Calif., Jan. 18–20, 1965, pp. 75–94 (Inst. Environmental Sciences and Am. Soc. Testing and Materials, 1965).*
Three methods are described for the measurement of the spectral irradiances of solar simulators at the National Bureau of Standards. The design of acceptable equipment is significantly affected by large variations in sensitivity of photoelectric and thermoelectric detectors with the wavelength and over their surfaces. The first instrumentation consists of a conventional spectroradiometer in which the source flux is collected in an integrating sphere which insures accurate evaluation of the solar simulator flux in terms of that from a 1000-watt lamp standard of spectral irradiance. A MgO-coated sphere is used for the ultraviolet, visible and near infrared to 1.6 microns. For longer wavelengths a gold-coated sphere was found more efficient. The second instrumentation consists of a photoelectric filter spectroradiometer in which 36 interference filters mounted on a filter wheel are selected and placed in correct optical position through the use of a T–V rotor motor. In both of these instrumentations photoelectric detectors are employed with the flux beam chopped at 510 cps and the signal measured ac-wise. The third instrumentation is a thermoelectric filter spectroradiometer wherein the filters are likewise mounted on a filter wheel. The thermoelectric output is measured dc-wise with the detector calibrated through the use of a lamp standard of total irradiance. The supplementary use of the first two instrumentations is recommended.

The response of flush diaphragm pressure transducers to thermal gradients, L. Horn, *ISA 20th Annual Conf. and Exhibit, Los Angeles, Calif., Oct. 4–7, 1965,* **20,** *Pt. III, ISA Preprint No. 13.3–4–65 (1965).*
The zero signal output of pressure transducers may alter during field use in the presence of thermal gradients. The changes can be large enough to cause serious questioning of the validity of test data taken without corrections for the zero shift.
Variations of up to 100% FS (full scale) have been found using transducers that indicated less than a 6% shift in the standard steady state temperature tests.
A simple method of dynamic testing is described and experimental results are given for a number of tests.

Key Words: Flush diaphragm, pressure gage, temperature, temperature gradient, transducers.

Color designation and specification, D. B. Judd, *Encyclopedia of Industrial Analysis* **1,** *315 (1966).*
Tristimulus colorimetry is summarized from basic assumptions to the 1931 CIE standard observer and the 1964 CIE supplementary observer and coordinate system for large-field colorimetry. Three types of tristimulus colorimetry (visual, photoelectric, spectrophotometric) are described including operating procedures, methods of reducing the data, and a summary of applications. A similar treatment is given of approximate colorimetry by systematic collections of color standards (Munsell, Ostwald, Maerz & Paul dictionary) including determination of the ISCC–NBS color designation. Definitions of radiometric, photometric, and colorimetric terms used are given in the form of a glossary.

Electrical testing in chemical technology, A. H. Scott, *Encyclopedia of Chemical Technology, 2d ed.* **7,** *716–726 (1965).*
Electrical testing of one sort or another is being used today to (a) determine the electrical properties of materials for design purposes, (b) determine the purity of the materials, (c) check the uniformity of manufacture or the manufacturing process, (d) aid in developing an understanding of the molecular structure of materials, (e) characterize materials, and (f) indicate the influence of environment on the properties of materials. The purpose of this article is to briefly describe such electrical measurements and to indicate their usefulness and limitations.

Measurement of DC dielectric conductance (reciprocal resistance) at elevated temperatures, A. H. Scott, *Proc. 6th Electrical Insulation Conf., Sept. 13–16, 1965, pp. 252–254 (1965).*
The new term adopted by Committee D-9 ASTM (DC Dielectric Conductance) for the conductance observed in electrical insulating materials differentiates this type of conductance from that in metals or other conducting materials. Measurements at elevated temperatures require special precautions and special emphasis on some of the usual precautions of measurement. Special cells or holders are required for these measurements.

The calibration of permanent magnet standards, I. L. Cooter, *ISA 20th Annual Conf. and Exhibit, Part 1. Measurement Standards and Instrumentation, Los Angeles, Calif., Oct. 4–7, 1965, 20 Pt. 1, ISA Preprint 14.1–3–65 (1965).*
The increased demand for the calibration of permanent magnets used as reference standards has required a new magnet calibration facility at the National Bureau of Standards, Washington, D.C. The method procedure and apparatus used in the calibration of reference magnets are described.

237-679 O–67—6

The nature of measurement, A. G. McNish, *Book, Industrial Metrology (Sponsored by the American Society of Tool and Manufacturing Engineers), chs. 1, 4, No. 2, 24–31 (Mar. 1966).*
General principles for measurement. Accuracy and precision are discussed.

Resolving power related to aberration, F. E. Washer, *Photogrammetric Eng.* **XXXII,** *No. 2, 213–226 (Mar. 1966).*
An heuristic method which accounts for the discrepancy between measured and theoretical values of resolving power of lenses is presented. The analysis also accounts for the sharp decline in contrast with increasing values of resolving power expressed in lines per mm in the image plane. Analyses are given of the probable effects on resolution and contrast of the fraction of the lens area transmitting image-forming light, longitudinal chromatic aberration, and longitudinal spherical aberration. An example is given that demonstrates change in focus with change in resolving power and shows how it is readily explained on the basis of simple diffraction theory.

Second breakdown and current distributions in transistors, H. A. Schafft and J. C. French, *Solid-State Electron.* **9,** *No. 7, 681–688 (July 1966).*
A study of second breakdown in transistors, which included the use of temperature-sensitive phosphors to reveal current distributions, has emphasized how intimately the susceptibility of the transistor to second breakdown is linked to the internal distribution of current or of energy dissipation. The effect of such factors as the base drive and internal structural irregularities on the internal current distribution is described. A better understanding of the role of the base drive in second breakdown was achieved and led to a test which was used to distinguish second breakdown from other low voltage modes that have been recently reported to be different levels of second breakdown.

Key Words: Diodes, failure mechanisms, internal current distributions, second breakdown, semiconductors, temperature sensitive phosphors, transistors.

Other NBS Publications

J. Res. NBS 70A (Phys. and Chem.) No. 6 (Nov.-Dec. 1966), $1.00.

Absolute isotopic abundance ratios and atomic weight of magnesium. E. J. Catanzaro, T. J. Murphy, E. L. Garner, and W. R. Shields.
Mass spectrometric study of photoionization V. Water and ammonia. V. H. Dibeler, J. A. Walker, and H. M. Rosenstock.
Interpretation of the third spectrum of gold (Au III). L. Iglesias.
A formal solution for slit corrections in small-angle x-ray scattering. J. Mazur and A. M. Wims.
High-temperature reactions of hexafluorobenzene. J. M. Antonucci and L. A. Wall.
The melting temperatures of the *n*-paraffins and the convergence temperature for polyethylene. M. G. Broadhurst.
General treatment of the thermogravimetry of polymers. J. H. Flynn and L. A. Wall.
Viscoelastic behavior under large deformations. L. J. Zapas.
Statistical aspects of second and third law heats. W. S. Horton.
Density-temperature formulae for coexisting liquid and vapor and for freezing liquid parahydrogen. R. D. Goodwin.
Solubility of $CaHPO_4 \cdot 2H_2O$ and formation of ion pairs in the system $Ca(OH)_2$-H_3PO_4-H_2O at 37.5 °C. E. C. Moreno, T. M. Gregory, and W. E. Brown.
Dissociation of some substituted phenols in 50-percent aqueous methanol as solvent. R. A. Robinson and R. G. Bates.

J. Res. NBS 71A (Phys. and Chem.), No. 1, (Jan.-Feb. 1967), $1.00.
Dedication of the new NBS laboratories.
Electric fields produced in cubic crystals by point defects. A. D. Franklin and D. J. Sparks.
Heat capacity and thermodynamic properties of beryllium 1 : 3-aluminate, $BeO \cdot 3Al_2O_3$, from 15 to 390 °K. G. T. Furukawa and W. G. Saba.
Dissociation constant of *m*-nitrophenol in 50 wt percent methanol-water solvent from 25 to 40 °C and related medium effects. B. J. Steel, R. A. Robinson, and R. G. Bates.
On the calculation of moments of molecular weight distribution from sedimentation equilibrium data. I. H. Billick, M. Schulz, and G. H. Weiss.
The far infrared spectrum of vulcanized natural rubber. J. E. Stewart and F. J. Linnig.
Irradiation of dextran and its aqueous solutions with cobalt-60 gamma rays. J. H. Flynn, L. A. Wall, and W. L. Morrow.
Synthesis of poly-p-oxyperfluorobenzylene and related polymers. A novel synthesis of the monomer 2,3,5,6-tetrafluoro-4-trifluoromethylphenol. J. M. Antonucci and L. A. Wall.
Preparation, purity, and homogeneity of NBS standard samples 705 and 706, polystyrene. D. McIntyre.
Large-scale, preparative paper chromatography. H. L. Frush.
Infrared absorption spectra of some aldofuranoid, aldopyranoid, and acyclic 1-acylamido derivatives of sugars. R. Stuart Tipson, A. S. Cerezo, V. Deulofeu, and A. Cohen.

J. Res. NBS 70B (Math. and Math. Phys.), No. 4 (Oct.–Dec. 1966), 75 cents.
A random walk model of chain polymer adsorption at a surface. III. Mean square end-to-end distance. R. J. Rubin.
Abscissas and weights for Gaussian quadrature for $N=2$ to 100, and $N=125$, 150, 175, and 200. C. H. Love.
Transverse impact of a linear three-element spring and dashpot model filament: theory. J. C. Smith.
Functions for thermal stress calculations near a transient heat source on a flat surface. S. Jarvis, Jr., and G. Hardy.

The band spectrum of carbon monoxide, P. H. Krupenie, NSRDS–NBS5 (July 8, 1966), 70 cents.
Interrelations between cement and concrete properties. Part 2. Sulfate expansion, heat of hydration, and autoclave expansion, R. L. Blaine, H. T. Arni, and D. N. Evans, NBS Bldg. Sci. Series 5, Pt. 2 (July 1, 1966), 35 cents.
Cast iron soil pipe and fittings, CS188–66 (July 1, 1966), 40 cents. (Supersedes CS188–59).
Southern pine plywood, Comm. Std. CS259–63 (as amended through Feb. 1, 1966) (Nov. 15, 1963), 15 cents.
Expanded vinyl fabrics for furniture upholstery use, Comm. Std. CS273–65 (Dec. 31, 1965), 10 cents.
TFE-fluorocarbon (polytetrofluoroethylene) resin sintered thin coatings for dry film lubrication, CS274–66 (Jan. 20, 1966), 10 cents.
Information handling in the National Standard Reference Data System, F. L. Alt, NBS Tech. Note 290 (July 1, 1966), 25 cents.
A bibliography on ion-molecule reactions. January 1900 to March 1966, F. N. Harllee, H. M. Rosenstock, and J. T. Herron, NBS Tech. Note 291 (June 28, 1966), 30 cents.
The viscosity and thermal conductivity coefficients of dilute argon between 100 and 2000 °K, H. J. M. Hanley, NBS Tech. Note 333 (Mar. 11, 1966), 25 cents.
Zonal harmonics in low frequency terrestrial radio wave propagation, J. R. Johler, NBS Tech. Note 335 (Apr. 13, 1966), 25 cents. (Formerly the Central Radio Propagation Laboratory of the National Bureau of Standards, now the Environmental Science Services Administration, Boulder, Colo.)
Acids, bases, and buffers, R. G. Bates (Proc. Symp. Current Concepts of Acid-Base Measurements, New York Academy of Sciences, New York, N.Y., Nov. 23, 1964), Ann. N. Y. Acad. Sci. **133,** Art. 1, 25–33 (1966).
Comparative strengths of aliphatic acids and some other carboxylic acids in benzene at 25°, M. M. Davis and M. Paabo, J. Organic Chem. **31,** 1804–1810 (1966).
Crystal chemistry of calcium phosphates, W. E. Brown, Proc. 1964 Technical Session on Cane Sugar Refining Research, New Orleans, Louisiana, Nov. 9–10, 1964, pp. 26–34 (Agriculture Research Service, New Orleans, Louisiana, Mar. 1966).
Equilibrium pressures of oxygen over oxides of lead at various temperatures, E. M. Otto, J. Electrochem. Soc. **113,** No. 6, 525–527 (June 1966).

Liquid immiscibility in the rare earth oxide-boric oxide systems, E. M. Levin, Phys. Chem. Glasses **7,** No. 3, 90–93 (June 1966).

Low-frequency motions and barrier to rotation in phosphonium iodide, J. J. Rush, J. Chem. Phys. **44,** No. 4, 1722–1723 (Feb. 15, 1966).

Matrix-isolation study of the infrared and ultraviolet spectra of the free radical CNN, D. E. Milligan and M. E. Jacox, J. Chem. Phys. **44,** No. 8, 2850–2856 (Apr. 15, 1966).

Microwave spectra of alkali hydroxides: evidence for linearity of CsOH and KOH, R. L. Kuczkowski, D. R. Lide, Jr., and L. C. Krisher, J. Chem. Phys. **44,** No. 8, 3131–3132 (Apr. 15, 1966).

Neutron and infrared spectra of $HCrO_2$ and $DCrO_2$, J. J. Rush and J. R. Ferraro, J. Chem. Phys. **44,** No. 6, 2496–2498 (Mar. 15, 1966).

Structure of cubic ammonium fluosilicate: neutron-diffraction and neutron-inelastic scattering studies, E. O. Schlemper, W. C. Hamilton, and J. J. Rush, J. Chem. Phys. **44,** No. 6, 2499–2502 (Mar. 15, 1966).

Anniversaries in 1965 of interest to statisticians, C. Eisenhart, Am. Stat. **19,** No. 5, 21–29 (Dec. 1965).

The assumptions underlying the analysis of variance, C. Eisenhart (Spanish Translation by Jose Otaduy), Book, Sobre el Analisis de la Variancia, pp. 1–24 (Comision de Educacion Estadistica del Instituto Interamerican de Estadistica, Rosario, Argentina, 1953).

Debye relaxation in symmetric-top-foreign-gas mixtures; temperature dependence of collision cross sections, L. Frenkel, S. J. Kryder, and A. A. Maryott, J. Chem. Phys. **44,** No. 7, 2610–2619 (Apr. 1, 1966).

Demountable high power source for soft x-ray region, R. D. Deslattes and B. G. Simson, Rev. Sci. Instr. **37,** No. 6, 753–754 (June 1966).

EPR spectrum of gas-phase sulfur atoms, R. L. Brown, J. Chem. Phys. **44,** No. 7, 2827–2828 (Apr. 1, 1966).

Inelastic scattering cross sections for 20-keV electrons in Al, Be, and polystyrene, N. Swanson and C. J. Powell, Phys. Rev. **145,** No. 1, 195–208 (May 6, 1966).

Methods of determining coriolis zeta constants, S. Abramowitz and I. W. Levin, J. Mol. Spectry. **19,** No. 4, 461–462 (Apr. 1966).

Plasmon damping metals, B. W. Ninham, C. J. Powell, and N. Swanson, Phys. Rev. **145,** No. 1, 209–217 (May 6, 1966).

Polycrystalline spin wave theory of ferro-magnetic resonance compared with the tilting experiment, A. S. Risley, E. G. Johnson, and H. E. Bussey, J. Appl. Phys. **37,** No. 2, 656–668 (Feb. 1966).

Shock wave propagation in cubic lattices, D. H. Tsai and C. W. Beckett, J. Geophys. Res. **71,** No. 10, 2601–2608 (May 15, 1966).

Superconducting behavior of indium-lead alloys, S. Gygax, J. L. Olsen, and R. H. Kropschot (Proc. IXth Intern. Conf. Low Temperature Physics, Columbus, Ohio, Aug. 31-Sept. 4, 1964), Book, Low Temperature Physics LT9, Pt. A, ed. J. G. Daunt, D. O. Edwards, F. J. Milford, and M. Yaqub, pp. 587–590 (Plenum Press Inc., New York, N.Y., 1965).

Superconductivity in ceramic, mixed titanates, H. P. R. Frederikse, J. F. Schooley, W. R. Thurber, E. Pfeiffer, and W. R. Hosler, Phys. Rev. Letters **16,** No. 13, 579–581 (Mar. 28, 1966).

Two-state model for the free volume of vitreous B_2O_3, P. B. Macedo, W. Capps, and T. A. Litovitz, J. Chem. Phys. **44,** No. 9, 3357–3364 (May 1, 1966).

A survey of the thermodynamic data on heavier elements and their compounds: high-temperature enthalpy and vaporization equilibria, T. B. Douglas, Proc. 3d Meeting Interagency Chemical Rocket Propulsion Group, Working Group on Thermochemistry, El Segundo, Calif., Mar. 17–18, 1965, I, No. 82U, 5–16 (Chemistry Propulsion Information Agency, Silver Spring, Md., July 1965).

Activation-analysis program and facilities at the National Bureau of Standards, J. R. DeVoe and G. W. Smith, Proc. 1965 Intern. Conf. Modern Trends in Activation Analysis, Texas A & M University, College Station, Texas, pp. 225–229 (Apr. 1965).

Additional observations on the electronic spectrum of copper (II) acetate monohydrate, C. W. Reimann, G. F. Kokoszka, and G. Gordon, J. Inorg. Chem. **4,** No. 7, 1082–1084 (July 1965).

Density and specific gravity, J. K. Taylor, Encyclopedia of Industrial Analysis **1,** 546–560 (Interscience Publ. Inc., New York, N.Y., 1965).

Determination of trace amounts of tellurium in standard reference materials by neutron-activation analysis, D. A. Becker, and G. W. Smith, Proc. 1965 Intern. Conf. Modern Trends in Activation Analysis, Texas A & M University, College Station, Texas, pp. 230–235 (Apr. 1965).

Equilibrium pressures of oxygen over Ag_2O-Ag at various temperatures, E. M. Otto, J. Electrochem. Soc. **113,** No. 7, 643–645 (July 1966).

Force fields for some group VI hexafluorides, S. Abramowitz and I. W. Levin, J. Chem. Phys. **44,** No. 9, 3353–3356 (May 1, 1966).

Formation of crystallites of benzophenone in hydrocarbon glass, R. Keller and D. Breen, J. Chem. Phys. **43,** No. 7, 2562–2563 (Oct. 1965).

Franck-Condon factors and the mass spectra of small molecules, H. M. Rosenstock (Proc. Intern. Mass Spectrometry Conf., ASTM E-14, The Hydrocarbon Research Group and GAMS, Paris, France, Sept. 1964), Adv. Mass Spectrometry **3,** 435–439 (1966).

Gas-phase radiolysis of cyclopentane. Relative rates of H_2-transfer reactions from various hydrocarbons to $C_3H_7^+$, R. D. Doepler and P. Ausloos, J. Chem. Phys. **44,** No. 5, 1951–1958 (Mar. 1966).

Infrared spectrum of the free radical CF_3 isolated in inert matrices, D. E. Milligan, M. E. Jacox, and J. J. Comeford, J. Chem. Phys. **44,** No. 10, 4058–4059 (May 1966).

Ion-molecule reaction in the liquid and solid phase radiolysis of hydrocarbon mixtures, P. Ausloos, A. A. Scala, and S. G. Lias, J. Am. Chem. Soc. **88,** 1583–1584 (1966).

Ion-pair process in CH_3Cl by photoionization, V. H. Dibeler and J. A. Walker, J. Chem. Phys. **43,** No. 5, 1842–1843 (Sept. 1965).

Microwave spectrum of perchlorylfluoride, D. R. Lide, Jr., J. Chem. Phys. **43,** No. 10, 3767–3768 (Nov. 1965).

Nuclear magnetic resonance studies of inorganic fluorides. II. Solvent effects on $J(^{29}Si-^{19}F)$ in silicon tetrafluoride, T. D. Coyle, R. B. Johannesen, F. E. Brinckman, and T. C. Farrar, J. Phys. Chem. **70,** No. 5, 1682–1684 (May 1966).

Phase relations between Cr_2O_3 and IrO_2 in air, C. L. McDaniel and S. J. Schneider, J. Am. Ceramic Soc. **49,** No. 5, 285–286 (May 1966).

Photoionization of propylene at 1236 Å. Reactions of $C_3D_6^+$ with added alkanes, R. Gorden, Jr., R. Doepker, and P. Ausloos, J. Chem. Phys. **44,** No. 10, 3733–3740 (May 1966).

Progress report on a test for cleanability, M. D. Burdick, Proc. Porcelain Enamel Institute Forum **26,** 41–48 (1965).

Progress report on the development of a standardized test for continuity of porcelain enamel coatings, M. A. Rushmer, Proc. Porcelain Enamel Institute **27,** 49–56 (1965).

Purification of single crystal growth, J. L. Torgesen, Ann. N.Y. Acad. Sci. **137,** 30–43 (1966).

Shear relaxation times of simple fluids, R. D. Mountain and R. Zwanzig, J. Chem. Phys. **44,** No. 7, 2777–2779 (Apr. 1966).

Silicon-fluorine chemistry. II. Silicon-boron fluorides, P. L. Timms, T. O. Ehlert, J. L. Margrave, F. E. Brinckman, T. C. Farrar, and T. D. Coyle, J. Am. Chem. Soc. **87,** No. 17, 3819–3823 (Sept. 1965).

Some aspects of the coulomb hole of the ground state of H_2^+, W. Lester and M. Krauss, J. Chem. Phys. **44,** No. 1, 207–212 (Jan. 1966).

Spectrochemical analysis of high-temperature alloys by spark excitation in argon and nitrogen, H. C. Dilworth, Am. Soc. Testing Mater, Spec. Tech. Publ. 376 (1965).

Standardization of the differential chemical shift for Fe^{57}, J. J. Spijkerman, F. C. Ruegg, and J. R. DeVoe, (Proc. New England Nuclear Mossbauer Symp., New York, N.Y., Jan. 1964), Book, Mossbauer Effect Methodology, pp. 115–120 (Plenum Press Inc., New York, N.Y., 1965).

The electron paramagnetic resonance spectrum of tetrakis-*t*-butoxyvanadium (IV), G. F. Kokoszka, H. C. Allen, Jr., and G. Gordon, Inorg. Chem. **5,** 91–93 (1966).

The microwave spectrum of dinitrogen trioxide, R. L. Kuczkowski, J. Am. Chem. Soc. **87,** 5259–5260 (1965).

A large signal IGFET DC source follower, D. P. Stokesberry, Proc. IEEE **54,** No. 1, 66 (Jan. 1966).

A semi-automatic technique for tuning a reflectometer, M. H. Zanboorie, IEEE Trans. Microwave Theory Tech. **MTT-13,** No. 5, 709–710 (Sept. 1965).

A simple current generator, J. K. Whittaker, Nuclear Instr. Methods **39,** No. 1, 183–184 (Jan. 1966).

A zero-crossing discriminator with picosecond time slewing, J. K. Whittaker, IEEE Trans. Nuclear Sci. **NS-13,** No. 1, 399–405 (Feb. 1966).

Effects of thermal shrinkage on built-up roofing, W. C. Cullen, J. Bldg. Res. Inst. **2,** No. 4, 23 (July-Aug. 1965).

Fire test methods for paints, A. F. Robertson, Bldg. Res. pp. 48–52 (July-Aug. 1965).

Guide to dental materials, 1966–1967, G. C. Paffenbarger, J. W. Stanford, M. P. Kumpula, and W. T. Sweeney, Am. Dental Assoc. 3d ed., 188 p. (Chicago, Ill., 1966).

Human engineering with design of a console for the comparison of volt boxes, P. H. Lowrie, Jr., ISA J. pp. 67–71 (July 1965).

International intercomparison of standards for microwave power measurement, G. F. Engen, IEEE Trans. Microwave Theory Tech. **MTT-13,** No. 5, 713–715 (Sept. 1965).

Measuring the coordinates of a number of points in a complex laboratory-scale model, F. D. Ordway, Rev. Sci. Instr. **36,** No. 8, 1156–1159 (Aug. 1965).

Modular software for on-line handling of nuclear data, J. M. Wyckoff, IEEE Trans. Nuclear Sci. **NS-13,** No. 1, 199 (Feb. 1966).

National Bureau of Standards offers method to prevent built-up roof splitting failure, W. C. Cullen, Roofing Siding Insulation Mag. **40,** No. 4, 28–30 (Apr. 1965).

1965 Meeting of IEC Committee TC45, Progress in Nuclear Instrumentation, L. Costrell, Mag. Std., p. 9 (Jan. 1966).

Roofing research in Guam and Okinawa, W. C. Cullen, Am. Roofer Bldg. Improvement Contractor, p. 10 (Oct. 1965).

Suppression of 60 c/s pickup when using sensitive DC amplifiers, R. L. Nuttall and D. C. Ginnings, Electron. Design **12,** No. 26, 34–35 (Dec. 20, 1965).

Tapered inlets for pipe culverts, discussion and author's closure, J. L. French, J. Hydraulics (Div. Am. Soc. Civil Eng.), p. 286 (May 1965).

The effect of insulation on the durability of a smooth-surfaced built-up roof, W. C. Cullen and W. H. Appleton, Coal Tar Asphalts and Related Mater. **3,** 122–124 (Mar. 1965).

Thermal insulation in buildings, F. J. Powell, Military Engr. **58,** No. 38, 275–276 (July-Aug. 1966).

Voltmeter calibration to 1 GHz, M. C. Selby, W. J. Blank, and R. P. Chairton (Proc. 1965 Wescon Conf., San Francisco, Calif., Aug. 1965), IEEE WESCON Tech. Papers **9,** pt. 6, No. 8.8, 1–12 (1965).

Congruence subgroups of positive genus of the modular group, M. Newman and M. Knopp, Ill. J. Math. **9,** No. 4, 577–583 (Nov. 1965).

Scattering properties of concentric soot-water spheres for visible and infrared light, R. W. Fenn and H. Oser, J. Appl. Opt. **4,** 1504–1509 (Nov. 1965).

The design of a federal statistical data center, D. Rosenblatt, E. Glaser, and M. K. Wood, Statistical Evaluation Report No. 6, Office of Statistical Standards, Bureau of the Budget, Appendix C, pp. 1–19 (Office of the President, Washington, D.C., Dec. 1965).

Measurement of DC dielectric conductance (reciprocal resistance) at elevated temperatures, A. H. Scott, Proc. 6th Electrical Insulation Conf., Sept. 13–16, 1965, pp. 252–254 (1965).

Metrology essential to the space age, A. G. McNish, George Washington University Mag. **1,** No. 4, 10–14 (1965).

Progress report for OSA Committee on uniform color scales, D. B. Judd, Proc. Intern. Color Comm., Lucerne, Switzerland, 1965, 1, 399–407 (Mar. 1966).

Specification and designation of color, D. B. Judd and I. Nimeroff, Treatise Anal. Chem. **36,** 2873–2942 (1964).

The international system of units, A. G. McNish, American Society for Quality Control Annual 1965 Tech. Conf. Trans. Industrial Quality Control **22,** No. 9, 465–469 (Mar. 1966).

Color appearance, D. B. Judd, Proc. Intern. Color Comm., Lucerne, Switzerland, 1965, 1, 27–51 (Mar. 1966).

Cooler for semiconductor light emitters, lasers and photodetectors, H. K. Kessler, Rev. Sci. Instr. **37,** 517–518 (Apr. 1966).

Decays of positive-parity baryon resonances in a broken U(12), H. Harari, D. Horn, M. Kugler, H. J. Lipkin, and S. Meshkov, Phys. Rev. **140,** No. 4B, B1003 (Nov. 1965).

Discussion of ASME paper 60–WA–333, November 30, 1960, D. P. Johnson and U. O. Hutton, Book, High Pressure Measurement, ed. A. A. Giardini and E. C. Lloyd, pp. 350–351 (Butterworth, Inc., London, England, 1963).

Effects of space radiation on refractive properties of optical glass, I. H. Malitson, M. J. Dodge, and M. E. Gonshery, Proc. Annual Conf. Photography, Science and Engineering, San Francisco, Calif., May 9–13, 1966, p. 75 (1966).

Elastic constants of single crystal UO_2 at 25 °C, J. B. Wachtman, Jr., M. L. Wheat, H. J. Anderson, and J. L. Bates, J. Nuclear Mater. 16, 39–41 (1965).

Electron energy bands in $SrTiO_3$ and TiO_2 (theory and experiment), A. K. Kahn, H. P. R. Frederikse, and J. H. Beckerd (Informal Proc. Bull., Intern. Conf. Materials, Pittsburgh, Pa., 1963), Book, Transition of Metal Compounds, ed. E. R. Schatz, pp. 53–64 (Gordon and Breach Sci. Publ., New York, N.Y., 1964).

Fundamental studies of color vision from 1860 to 1960, D. B. Judd, Proc. Natl. Acad. Sci. **55,** No. 6, 1313–1330 (June 1966).

Geomagnatic and solar data, J. V. Lincoln, J. Geophys. Res. **70,** No. 13, 3227–3228 (July 1965); **70,** No. 15, 3761–3763 (Aug. 1965); **70,** No. 17, 4383–4384 (Sept. 1965); **70,** No. 19, 4963–4964 (Oct. 1965).

High resolution infrared spectra of cyanogen and cyanogen-$^{15}N_2$, A. G. Maki, J. Chem. Phys. **43,** No. 9, 3193–3199 (Nov. 1965).

Interspecimen comparison of the refractive index of fused silica, I. H. Malitson, J. Opt. Soc. Am. **55,** No. 10, 1205 (Oct. 1965).

Intrinsic and lattice-induced distortion of the tetrachlorocuptrate ion, M. Sharnoff and C. W. Reimann, J. Chem. Phys. **43,** No. 9, 2993–2996 (Nov. 1965).

Line broadening, W. L. Wiese, Book, Plasma Diagnostic Techniques, ed. R. H. Huddleston and S. L. Leonard, 21, 265–317 (Academic Press, Inc., New York, N.Y., 1965).

Magnetic susceptibility of insulating and semiconducting strontium titanate, H. P. R. Frederikse and G. A. Candela, Phys. Rev. **147,** No. 2, 583–584 (July 15, 1966).

Magnetoacoustic adsorption and the fermi surface in potassium, H. J. Foster, P. H. Meijer, and E. V. Mielczarek, Phys. Rev. **139,** No. 6A, A1849–A1857 (Sept. 1965).

Magnetoresistance of semiconducting $SrTiO_3$, H. P. Frederikse, W. R. Hosler, and W. Thurber, Phys. Rev. **143,** No. 2, 648–651 (Mar. 1966).

Measurements of ion-optical properties of a high resolution spectrometer for electron scattering, S. Penner and J. W. Lightbody, Proc. Intern. Symp. Magnetic Technologies, Stanford Linear Accelerator Center, Stanford Univ., Calif., Sept. 8–10, 1965, pp. 154–163 (Oct. 1965).

Newly observed structure in the photoionization continua of Kr and Xe below 160 Å, K. Codling and R. P. Madden, Appl. Opt. **4,** 1431–1434 (Nov. 1965).

Observations of dislocations in ammonium dihydrogen phosphate: production of dislocation-free crystals, R. D. Deslattes, J. L. Torgesen, B. Parketzkin, and A. T. Horton, J. Appl. Phys. **37,** No. 2, 541–548 (Feb. 1966).

Observatory reports, spectroscopy, C. E. Moore, Astron. J. **70,** No. 9, 637–639 (Nov. 1965).

Optical absorption of cobalt in manganese fluoride, R. F. Blunt, J. Chem. Phys. **44,** No. 6, 2317–2320 (Mar. 15, 1966).

Photon absorption cross section of spherical nuclei, M. G. Huber, H. J. Weber, M. Danos, and W. Greiner, Phys. Rev. Letters **15,** No. 12, 529–531 (Sept. 1965).

Photoneutron reactions, E. G. Fuller (Proc. Intern. Conf. Study of Nuclear Structure with Neutrons, Antwerp, Belgium, July 14–23, 1965), Book, Nuclear Structure Study with Neutrons, ed. M. Neve De Mevergnies, P. VanAssche, and J. Vervier, pp. 359–375 (North-Holland Publ. Co., Amsterdam, The Netherlands, 1966).

Photonuclear reactions, M. Danos and E. G. Fuller, Ann. Rev. Nuclear Sci. **15,** 29–66 (1966).

Radiative recombination lifetimes in laser excited silicon, N. N. Winogradoff and H. K. Kessler, Appl. Phys. Letters **8,** No. 4, 99 (Feb. 1966).

Radiation of sound by earthquakes, R. K. Cook, 5e Cong. Intern. Acoustique, Liege, Belgium 1b, K19 (1965).

Relation of strength of thermally tempered glass to fracture mirror size, M. K. Kerper and T. G. Scuderi, Am. Ceramic Soc. Bull. **44,** No. 12, 953–955 (Dec. 1965).

Secondary electron trajectories in a Faraday cup magnetic field, J. S. Pruitt, Nuclear Instr. Methods **39,** 329 (Feb. 1966).

Structure in the photoionization continuum of N_2 near 500 Å, K. Codling, Astrophys. J. **143,** No. 2, 552–558 (Feb. 1966).

Symmetry conditions on jump rates occuring in relaxation times associated with point defect motion, H. S. Peiser and J. B. Wachtman, Jr., J. Phys. Chem. Solids **27,** 975 (1966).

Tables of dielectric constants, dipole moments and dielectric relaxation times, F. I. Mopsik, (1964 Digest of Literature on Dielectric

Conf. Electrical Insulation), NAS–NRC Publ. 1342, 28, 33–66 (Natl. Acad. Sci.-Natl. Res. Council, Washington, D.C., 1965).
The interaction of radiation with charged particles. I, W. H. Chappell, W. E. Brittin, and S. J. Glass, Il Nuovo Cimento **38,** No. 3, 1186–1191 (1965).
The interaction of radiation with charged particles. II. Dispersion relation for transverse modes, S. J. Glass and W. R. Chappel, Il Nuovo Cimento **38,** No. 1, 79–88 (1966).
The paramagnetic resonance spectrum of W^{5+} in rutile (TiO_2), T. T. Chang, Phys. Rev. **147,** No. 1, 264–267 (July 8, 1966).
Atmospheric research and electromagnetic telecommunication, Part I, H. G. Booker and C. G. Little, IEEE Spectrum **2,** No. 8, 44–52 (Aug. 1965).
Atmospheric research and electromagnetic telecommunication, Part II, H. G. Booker and C. G. Little, IEEE Spectrum **2,** No. 9, 98–103 (Sept. 1965).

**Publications for which a price is indicated are available by purchase from the Superintendent of Documents, U.S. Government Printing Office, Washington D.C. 20402 (foreign postage, one-fourth additional). The NBS nonperiodical series are also available from the Clearinghouse for Federal Scientific and Technical Information, Springfield, Va., 22151. Reprints from outside journals and the NBS Journal of Research may often be obtained directly from the authors.*

U.S. GOVERNMENT PRINTING OFFICE : 1967 OL—237-679

MICROFILMS SERIALS SECTION

UNITED STATES
GOVERNMENT PRINTING OFFICE
DIVISION OF PUBLIC DOCUMENTS
WASHINGTON, D.C. 20402

OFFICIAL BUSINESS

POSTAGE AND FEES PAID
U.S. GOVERNMENT PRINTING OFFICE

JOURNAL OF RESEARCH of the National Bureau of Standards Vol. 71C, No. 1 January–March 1967
C. Engineering and Instrumentation

Contents

	Page
Dedication of the new NBS laboratories.	I
Symmetrical bending of thin circular elastic plates on equally spaced point supports. A. F. Kirstein and R. M. Woolley.	1
Ultrasonic measurement of cylinder expansion at pressures to 40 kilobars. Peter L. M. Heydemann and James C. Houck.	11
A comparison of absorbed dose determinations in graphite by cavity ionization measurements and by calorimetry. Ben Petree and Paul Lamperti.	19
Germanium resistance thermometry in the range 2.1 to 5.0 °K. M. H. Edlow and H. H. Plumb.	29
Least squares technique for the analysis of periodic temperatures of the earth's surface region. Tamami Kusuda.	43
A new near-zone electric-field-strength meter. Frank M. Greene.	51
Inductance and characteristic impedance of a strip-transmission line. R. L. Brooke, C. A. Hoer, and C. H. Love.	59
Tensor permeability measurements at L-band frequencies using a degenerate mode cavity. L. B. Schmidt, R. D. Harrington, and W. E. Case.	69
Publications of the National Bureau of Standards.	77

Library of Congress Catalog Card Number: 62–3900

For sale by the Superintendent of Documents, U.S. Government Printing Office, Washington, D.C. 20402. Price 75¢ (single copy). Subscription price: $2.75 a year; 75¢ additional for foreign mailing.
UNITED STATES GOVERNMENT PRINTING OFFICE, WASHINGTON : 1967